NOVEL COMPOSITES FOR NONLINEAR TRANSMISSION LINE APPLICATIONS

by

Andrew J. Fairbanks

A Dissertation

Submitted to the Faculty of Purdue University

In Partial Fulfillment of the Requirements for the degree of

Doctor of Philosophy

School of Nuclear Engineering

West Lafayette, Indiana

May 2021

THE PURDUE UNIVERSITY GRADUATE SCHOOL

STATEMENT OF COMMITTEE APPROVAL

Dr. Allen Garner, Chair

School of Nuclear Engineering

Dr. Robert Bean

School of Nuclear Engineering

Dr. Ahmed Hassanein

School of Nuclear Engineering

D. Tyler Tallman

School of Aeronautics and Astronautics

Approved by:

Dr. Seungjin Kim

Dedicated to my wife Kristen and my parents whose love and support made this possible.

ACKNOWLEDGMENTS

I would like to thank the Office of Naval Research for funding this project under grant number N00014-18-1-2341 and the Directed Energy Professional Society Graduate Scholarship. I would like to thank my committee and especially Dr. Allen Garner for guiding me though this project and funding my graduate education. I would not have been able to complete all of the research tasks without the help of Travis Crawford, Xiaojun Zhu, Emily Downing, Jeremy Mateja, Leonardo Roca, Hayden Schultz, Mary Vaughan, and Luke Diehm. I would like to thank Russ Brayfield, Dr. Robert Bean, and Travis Crawford for their support and guidance that helped me make it through graduate school and providing lasting friendships that made the hard times much easier. I would not have been able to succeed without the love and support of my wife, Kristen, who was always there to help and support me through the long nights and days that made this possible.

TABLE OF CONTENTS

LIST OF TABLES

LIST OF FIGURES

ABBREVIATIONS AND DEFINITIONS

HPM:	high power microwaves
NLTL:	nonlinear transmission line
Directed Energy:	the propagation of electromagnetic waves from a source to a target in a coherent beam
Ferroelectric:	materials that have an inherent polarization
Ferromagnetic:	materials that have a high susceptibility to magnetization
LE:	lumped element; electrical circuits consisting of individual electric components
SRR:	split ring resonator
Precession:	the motion of a body or vector due to an external torque

ABSTRACT

Nonlinear transmission lines (NLTLs) provide a solid state alternative to conventional vacuum based high power microwave (HPM) sources. The three most common NLTL implementations are the lumped element, split ring resonator (SRR), and the nonlinear bulk material based NLTLs. The nonlinear bulk material implementation provides the highest power output of the three configurations, though they are limited to pulse voltages less than 50 kV; higher voltages are possible when an additional insulator is used, typically SF_6 or dielectric oil, between the nonlinear material and the outer conductor. The additional insulator poses a risk of leaking if structural integrity of the outer conductor is compromised. The desire to provide a fieldable NLTL based HPM system makes the possibility of a leak problematic. The work reported here develops a composite based NLTL system that can withstand voltages higher than 50 kV and not pose a risk of catastrophic failure due to a leak while also decreasing the size and weight of the device and increasing the output power.

Composites with barium strontium titanate (BST) or nickel zinc ferrite (NZF) spherical inclusions mixed in a silicone matrix were manufactured at volume fractions ranging from 5% to 25%. The dielectric and magnetic parameters were measured from 1-4 GHz using a coaxial airline. The relative permittivity increased from 2.74±0.01 for the polydimethylsiloxane (PDMS) host material to 7.45±0.33 after combining PDMS with a 25% volume fraction of BST inclusions. The relative permittivity of BST and NZF composites was relatively constant across all measured frequencies. The relative permeability of the composites increased from 1.001±0.001 for PDMS to 1.43±0.04 for a 25% NZF composite at 1 GHz. The relative permeability of the 25% NZF composite decreased from 1.43±0.05 at 1 GHz to 1.17±0.01 at 4 GHz. The NZF samples also exhibited low dielectric and magnetic loss tangents from 0.005±0.01 to 0.091±0.015 and 0.037±0.001 to 0.20±0.038, respectively, for all volume fractions, although the dielectric loss tangent did increase with volume fraction. For BST composites, all volume fraction changes of at least 5% yielded statistically significant changes in permittivity; no changes in BST volume fraction yielded statistically significant changes in permeability. For NZF composites, the change in permittivity was statistically significant when the volume fraction varied by more than 5% and the change in permeability was statistically significant for variations in volume fraction greater than 10%. The DC electrical breakdown strength of NZF composites decreased exponentially with

increasing volume fraction of NZF, while BST composites exhibited no statistically significant variation with volume fraction.

For composites containing both BST and NZF, increasing the volume fraction of either inclusion increased the permittivity with a stronger dependence on BST volume fraction. Increasing NZF volume fraction increased the magnetic permeability, while changing BST volume fraction had no effect on the composite permeability. The DC dielectric breakdown voltage decreased exponentially with increased NZF volume fraction. Adding as little as 5% BST to an NZF composite more than doubled the breakdown threshold compared to a composite containing NZF alone. For example, adding 10% BST to a 15% NZF composite increased the breakdown strength by over 800%. The combination of tunability of permittivity and permeability by managing BST and NZF volume fractions with the increased dielectric breakdown strength by introducing BST make this a promising approach for designing high power nonlinear transmission lines with input pulses of hundreds of kilovolts.

Coaxial nonlinear transmission lines are produced using composites with NZF inclusions and BST inclusions and driven by a Blumlein pulse generator with a 10 ns pulse duration and 1.5 ns risetime. Applying a 30 kV pulse using the Blumlein pulse generator resulted in frequencies ranging from 1.1 to 1.3 GHz with an output power over 20 kW from the nonlinear transmission line. The output frequencies increased with increasing volume fraction of BST, but the high power oscillations characteristic of an NLTL did not occur. Simulations using LT Spice demonstrated that an NLTL driven with a Blumlein modulator did not induce high power oscillations while driving the same NLTL with a pulse forming network did.

Finally, a composite-based NLTL could be driven directly by a high voltage power supply without a power modulator to produce oscillations both during and after the formed pulse upon reaching a critical threshold. The output frequency of the NLTLs is 1 GHz after the pulse and ranged from 950 MHz to 2.2 GHz during the pulse. These results demonstrate that the NLTL may be used as both a pulse forming line and high power microwave source, providing a novel way to reduce device size and weight, while the use of composites could provide additional flexibility in pulse output tuning.

1. INTRODUCTION

This chapter was published in IEEE Access, see Ref. [133]. The interest in nonlinear transmission lines (NLTLs) has increased in the past several decades because they can sharpen pulses to less than 100 ps [1] and serve as a solid state radiofrequency (RF) source. NLTL systems use components with nonlinear permittivity and/or permeability to sharpen pulses by allowing waves with higher amplitudes to travel faster than lower amplitude portions of the pulse to form an electromagnetic shock. Following electromagnetic shockwave formation, oscillations occur due to the motion of either the dipole or magnetic moment of the nonlinear permittivity or permeability of the material, respectively. The shockwaves from a nonlinear dielectric transmission line induce oscillations with frequencies generally below 100s MHz. Nonlinear magnetic transmission lines can produce oscillations with frequencies up to low GHz after the material is saturated [1]. These oscillations occur either due to the precession of magnetic moments for nonlinear magnetic materials or the translations of the dipole in the crystalline structure for nonlinear dielectric materials. The repetition rate, greater than 1 kHz, and consistency of the RF output make these devices practical for both low and high power RF applications [2], [3]

The technological development of fast, high voltage switching with capabilities up to hundreds of kHz [4]–[6] has motivated the development of high repetition rate RF sources with similar capabilities. Traditional microwave sources cannot operate at these high repetition rates because long electron recombination times lead to an increase in space charge in the gap, limiting microwave generation in traditional vacuum systems [7]. NLTLs provide a solid state RF source that can operate above 1 kHz with very little variation [3], [8].

While some systems provide high power capabilities by using high power components, such as lumped element designs [9], others provide a compact, narrowband, tunable design, such as split ring resonators (SRRs) [10]. Using nonlinear dielectrics in conventional transmission line configurations can achieve both high power and compactness [11]. Using these nonlinear materials in a coaxial design provides phase shifting, which allows beam combination and beam steering to yield a directional, high power, high repetition rate RF source that can be tuned to meet various needs.

This chapter [133] summarizes the different methods for constructing traditional NLTLs with either nonlinear permittivity or nonlinear permeability and the recent development of a hybrid

NLTL with nonlinearity in both permittivity and permeability. We review the three main NLTL topologies (lumped element, split ring resonator (SRR), and nonlinear dielectric materials) both experimentally and theoretically. Section 2 summarizes lumped element NLTLs, Section 3 discusses SRRs, and Section 4 describes NLTLs designed using nonlinear dielectrics. We make concluding remarks in Section 5.

1.1 Lumped Element Nltls

Constructing NLTLs with lumped element circuits has allowed for more detailed studies of the physical phenomena and tunability of nonlinear effects by using circuit simulation software to analyze nonlinear capacitance and/or nonlinear inductance, as shown in Fig. 1. These circuits may be constructed using commercial off-the-shelf (COTS) devices and novel nonlinear components.

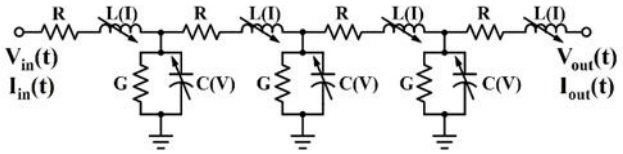

Figure 1. Lumped element representation of a nonlinear transmission line (NLTL) comprised of both nonlinear capacitance *C*(*V*) a function of voltage and inductance *L*(*I*) a function of current that translates an input voltage $V_{in}(t)$ and current $I_{in}(t)$ into an output voltage $V_{out}(t)$ and output current $I_{out}(t)$. An NLTL may be constructed with nonlinear capacitance and/or inductance. In general, loss may be included through a resistance *R* in series with the inductor or a conductance *G* in parallel with the capacitance.

The equation for the general, lossy, nonlinear transmission line in Fig. 1 is given by

$$\frac{\partial^2 V(x)}{\partial x^2} = (j\omega L(I) + R)(j\omega C(V) + G)V(x), \tag{1}$$

where V is voltage, x is position along the line, ω is angular frequency, $L(I)$ is inductance as a function of current I, R is resistance in series with $L(I)$, $C(V)$ is capacitance as a function of V, and G is conductance in parallel with $C(V)$.

1.1.1 Theoretical Contributions

Fundamental wave dynamics and transmission through nonlinear materials have been studied since the second half of the 20th century [12]. The mathematical solutions to the circuit equations often separate the incident pulse into solitons based on the amplitude to evaluate the wave speed of

each soliton independently; these results demonstrate that higher amplitude solitons propagate faster than the lower amplitude ones [12]–[14]. These solutions can preserve the identities of the waves after their nonlinear interactions with each other, meaning that that the solitons "pass through" one another and reappear with virtually the same size or shape as prior to the interaction [12], [15]. The various solutions form arrays that can be optimized to achieve the shortest pulse rise time without oscillations when used as a pulse sharpening line [13]. For applications seeking RF oscillations, one may also determine the minimum NLTL length. Numerical techniques, such as the Bulirsch-Stoer or Runge-Kutta methods [12], [13], [16], have been used to solve the wave equation for the nonlinear circuits. The Runge-Kutta method is more efficient than the Bulirsch-Stoer method for very sharp rise times due to its simpler step calculation [13].

The circuit equations can also be simplified from a partial differential equation (PDE) to an ordinary differential equation (ODE) using Taylor series expansions and appropriate simplifications [14], [17]. This technique can model NLTLs with nonlinear capacitors made from metal oxide semiconductor (MOS) varactors. The simulations demonstrate the potential to sharpen both the rising and falling edges of the pulse [14]. As the wave propagates down the line, it is separated into various solitons; applying the output to a linear matched load, such as a resistor, reduces the oscillations because the various solitons interfere with one another [18]. Applying the output pulse to a much larger output resistance lowers signal amplitude losses, mitigating the oscillation issues [18]. Numerical simulations have also solved the resulting nonlinear PDEs derived through circuit analysis to determine the capacitance of nonlinear capacitors comprised of ionic polymer-metal composites [19].

NLTLs can be modeled with lumped elements by making the standard transmission line capacitance and inductance functions of voltage and current, respectively. The Korteweg-de Vries equation may be solved numerically for NLTLs comprised of nonlinear inductors with linear capacitors [20], nonlinear capacitors with linear inductors [9], and hybrid line configuration with nonlinear capacitors and nonlinear inductors [21], [22], discussed later in this review. The circuit model compared well with experimental results and showed how the frequency and output of the lines varied with nonlinearity. The output of nonlinear capacitive transmission lines uses a decoupling capacitor to extract the AC signal, then applied to a load to allow for direct extraction [9].

Alternatively, one can separate the circuit analysis problem into different sub-problems by decoupling the linear and nonlinear subcircuits; balancing-related model reduction techniques reduce the linear subcircuit [23]. The reduction technique can be further refined by integrating the order-estimation algorithm with the proper-orthogonal decomposition reduction model to increase efficiency and decrease computational cost [24]. This can also be done for nonlinear inductors to solve for the magnetic vector potential and inductance as a function of current; results agree well with COMSOL simulations [25]. Another study used a multistage Adomain decomposition method, which is a hybrid analytical-numerical mathematical technique for solving nonlinear PDEs. This method is commonly used to model the transient behavior of nonlinear circuits, such as those containing ferroelectric ceramic capacitors [26]. This approach solves a circuit model with a nonlinear resistor exhibiting cubic voltage-current dependence in series with a nonlinear capacitor exhibiting quintic voltage-charge dependence [26].

Characterizing the output from different NLTL topologies is critical for various applications in directed energy, pulsed power, and high power microwaves (HPM). SPICE circuit simulations of an NLTL can determine its output frequency and input pulse rise time sharpening [27]. Evaluating wave propagation through the NLTL elucidates the physics involved by characterizing complex wave interactions [28], which can be important for achieving desired performance. SPICE simulations have also verified theoretical modeling of wave propagation and RF generation in NLTLs [29].

More recently, researchers studied nonlinear Schottky diodes for NLTL applications. One group developed a model that evaluated the formation and propagation of a large-amplitude electromagnetic shock wave in an NLTL comprised of distributed Si and 4H-SiC diodes [30]. This group applied this model to extract n-layer thickness, breakdown voltage, total semiconductor thickness, optimum line length, minimum electrode thickness, normalized voltage drop along the electrodes, and normalized line width. This study further showed that the required rise time of the input pulse determined the maximum output voltage, concluding that SiC based diodes were better suited for high voltage applications compared to distributed Si [30]. The influence of imperfections in varactor diodes used as nonlinear capacitors in coupled NLTLs has also been studied. For NLTLs weakly capacitively coupled with a linear capacitance, a low impurity rate can cause leapfrogging as a result of potential acceleration of the soliton in the defect line [31].

1.1.2 Experimental Contributions

While analytic models and simulations of lumped element NLTLs are valuable for system design, they must ultimately be compared to experimental results. Several studies have constructed NLTLs using COTS components such as nonlinear capacitors, nonlinear inductors, and hybrid lines. Experiments with COTS nonlinear capacitors agreed well with lumped element models [9]. Experimental results for hybrid NLTLs agreed well with the numerical models created using the Korteweg-de Vries method [22]. Another study applied a 30 ns pulse through a lumped element nonlinear inductor-based NLTL with saturable magnetic materials in an LC ladder network to generate an output RF frequency of 1 GHz at 20 MW peak power with a repetition rate of 1.0-1.5 kHz [32]. This study also constructed phased NLTL arrays to provide a higher power RF source [32].

Numerous materials have been used for nonlinear capacitance COTS components NLTLs. A parallel plate NLTL design used nonlinear capacitance lead-manganese-niobate ceramic (PMN38 from TRS company); the desired linear inductance was selected by appropriately spacing capacitor sections [33]. The dielectric loss was modeled as a series resistance based on the measured loss tangent of the NLTL. B-dot probes measured the pulses and current viewing resistors (CVRs) characterized the pulse evolution through the NLTL. An LTspice circuit model using the nonlinear capacitor model showed that the loss resistance prevented RF oscillations [33].

Evaluating COTS devices allows for better optimization and evaluation for their use in NLTLs. COTS capacitors constructed from lead-zirconate-titanate (PZT) and barium titanate (BT) were tested for their loss tangent, under different bias voltages, from 10 MHz to 1 GHz. The real and imaginary permittivities were extracted from the scattering parameters (S parameters), measured using a vector network analyzer (VNA). These studies showed that PZT capacitors were better suited for NLTLs because their capacitance changed more strongly as a function of applied voltage [34]. Another NLTL created using COTS capacitors with BT as the main component in the dielectric achieved measured rise-times between 1.84 and 2.5 μs, in agreement with 2.2 μs from simulations. The output pulse had a peak power of 8 kW for an output frequency of approximately 4 MHz [35].

Other studies evaluated COTS capacitors with X7R dielectric for use in NLTLs. Experiments showed that X7R NLTLs sharpened rise times down to tens of ns. Because the NLTL's cutoff frequency was 500 MHz, it could produce higher frequencies than other lumped element NLTLs with nonlinear capacitors. Simulations also showed that cross linking linear and nonlinear capacitors enabled frequency production [36]. A more recent approach for lumped element NLTLs leveraged the nonlinear capacitance of Schottky diodes to achieve a higher output frequency of 200 MHz, which agreed well with simulations. Continuing maturation of manufacturing techniques and improvement of material properties make Schottky diode NLTLs promising for higher frequency applications [37],[38]. Increasing the NLTL to a 30-section topology is expected to provide 65 W peak power and 115 V voltage modulation depth [38]. Double ridged guide antennas can extract and propagate the oscillations from the NLTL [39].

Using varactor diodes as nonlinear capacitors, may produce up to 90% variation in their capacitance, although they are only useful at low voltages. However, an amplifier circuit utilizing MOSFETs can increase the voltage modulation depth from 10.7 V to 40 V for a frequency of 33.3 MHz [40]. The input pulse shape significantly affects the frequency generation and efficiency of the oscillations produced. One study showed that a 150 ns rectangular pulse was optimal compared to a half sine wave and triangular wave [41]. Because the rise time was a critical attribute of the input pulse, this study was somewhat misleading since the rectangular, triangular, and half sine pulses had different rise times.

Varactor diodes recently produced a left-handed NLTL that increased the third-harmonic signal fivefold compared to conventional left-handed NLTLs. The circuit topology generated edge states that produced higher harmonic signals at increased levels [42].

CMOS technology provides a unique application for NLTLs as frequency multipliers. A frequency doubler and tripler were fabricated using CMOS processing to generate 20 GHz and 100 GHz, respectively. The 100 GHz tripler produced 0.7 W and a 12.2 dB bandwidth [43].

Table 1 summarizes the studies that evaluate lumped element NLTLs. While most lumped element NLTLs provide lower output power than NLTLs that utilize nonlinear materials, they elucidate the underlying physics in nonlinear wave propagation and can provide a more compact RF source.

Table 1. Summary of lumped element NLTLs.

Study	Input Pulse Amplitude (V)	Input Pulse Duration (ns)	RF Generation Frequency (GHz)	RF Generation Output Peak Power	Nonlinear Component	Modeling Method
[14]	1.85	0.05	-	-	C	SONNET
[21]	6,000	600	0.05-0.08	5 kW	C&L	Korteweg-de Vries
[22]*	5	400	0.025-0.055	0.31 W	C	Korteweg-de Vries
[22]*	5	400	0.015-0.07	0.27 W	C&L	Korteweg-de Vries
[27]	10	150	0.04	-	C	SPICE
[32]*	30,000-50,000	60	1	20 MW	L	-
[33]	4,000-43,000	50	-	-	C	LT Spice
[35]	400	3270	0.004	8 kW	C	LT Spice
[36]	500	600	-	-	C	-
[37]	500	34	0.2	-	C	LT Spice
[128]	5	50	0.8	0.125 W	C&L	LT Spice
[129]	1,000	-	0.033	-	C&L	-

* tunable output frequency
C = Capacitor; L = Inductor.

1.2 Split Ring Resonators

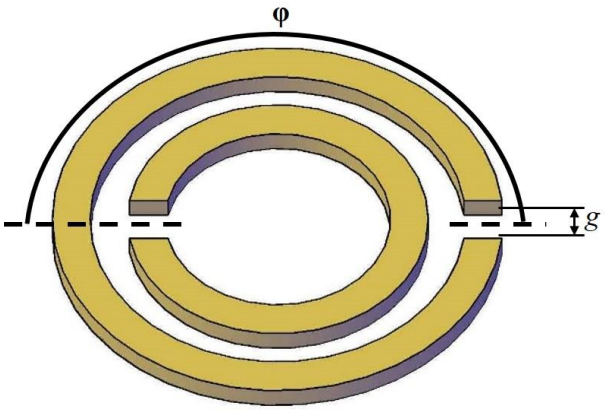

Figure 2. Coplanar split ring resonator circuit topology with gap width *g* and split angle φ.

SRRs comprised of different materials can provide nonlinear responses to input pulses, offering unique solutions to creating RF generators and narrowband signals. However, since SRRs are resonant structures resulting from the inductance produced by the ring structure and the capacitance from the gap, *g* in Figure 2, the resulting oscillations will be narrowband without a nonlinear component. SRRs are generally small, with a correspondingly small power output; however, they may be arrayed to increase the total effective power. Figure 2 shows a representative coplanar, double SRR. This section describes modeling and experimental studies using SRRs and their application to NLTLs.

1.2.1 Modeling Contributions

The initial work by Pendry and colleagues demonstrated that structures made of linear materials interacting with electromagnetic waves can exhibit negative permittivity and/or permeability [44], [45]. These studies showed that microstructures built from nonmagnetic conducting sheets exhibit a tunable effective magnetic permeability, including the potential to induce large imaginary components. Internal capacitance and inductance made most of the structures resonant, enabling the enhancement of the nonlinearity [44].

SRRs can be combined in various geometries such as coplanar, where SRRs are coupled through interactions between their edges (EC-SRR), and coaxial, where SRRs are coupled through interactions between the broadsides of the structure. A quasi-analytical and self-consistent model was developed to determine the polarizabilities of SRRs. This model applied a local field approach to determine the dielectric parameters and resonance frequency of negative permeability and left-handed SRRs for both coplanar/edge coupled and coaxial/broadside coupled SRRs [46]. Another study evaluated three patterns of EC-SRR designs for placement onto a truncated pyramidal microwave absorber. CST Microwave Studio simulations for frequencies from 0.01-20 GHz showed that reflection loss decreased for all frequencies with the largest change from 15-20 GHz [47]. An outer split ring gap width (cf. Fig. 2) of $g = 0.02$ cm, the minimum value analyzed, yielded the lowest reflection loss performance [47].

Left hand (LH) wave propagation occurs when both permittivity and permeability are negative, thus reversing the vector orientation from a right handed orientation to a left handed

orientation for the electric field (**E**), magnetic field (**H**), and the wave vector (**k**) [49]. Coplanar waveguide (CPW) inductively coupled SRRs periodically loaded with narrow metallic wires yield the negative permeability required to achieve LH wave propagation in a narrow frequency band [48]. Prototypes exhibited high-frequency selectivity and low pass band insertion losses. Since the rings were smaller than the signal wavelength, the wavelength was easily tuned to the resonance frequency, 7.7 GHz [48]. Circular polarization selective surfaces have also been developed by placing planar SRRs coaxially and orienting the split to different positions, designated by φ in Fig. 2. A CST Microwave Studio model of this device showed resonant peaks at 9.75 and 10 GHz. The excellent agreement between simulation and experiments demonstrated the benefit for their application as an equivalent of gridded reflectors such as those used on satellites [50].

Narrow resonance bandwidth has motivated SRR research focused on increasing bandwidth. The bandwidth of an SRR may be increased by rotating its inner ring at different angles in a hybrid structure or changing its dimensions. Bandwidth increases of approximately 70% were proposed for such a unit cell comprised of three SRRs with different resonant frequencies, and SRR arrangement should be based on a descending and/or ascending resonant frequency order. Strip-line measurements confirmed that selecting either ascending or descending order did not change the loss tangent of the unit cell [51]. Models of these geometries have typically used analytic circuit models, which are limited to certain classes of structures and often fail to accurately predict the macroscopic behavior of metamaterials, or electromagnetic simulations, such as the finite integration method (FIM) or the finite element method (FEM) [52].

SRRs may be modeled with differential equations for current and voltage distributions, solved analytically to determine the resonant frequencies. An approximate solution for the lowest resonant frequency agrees with heuristic arguments and numerical simulations [53]. Alternatively, one may use simulation software, such as the MICRO-STRIPES package, a 3D electromagnetic simulation tool that solves problems in the time domain, or by replace the distributed circuit with discrete circuits [53]. Treating the SRRs as inclusions in a bulk material allows development of a numerical model for double SRRs (cf. Fig. 2) to assess polarization for both planar and wire SRRs with the capacitance validated using ANSOFT [54]. The resonant frequency of an SRR depends strongly on the capacitance of the structure. The resonant frequency for these devices depends on the gap surface capacitances, which may be determined using the equation for an electric field in

a split cylinder combined with conformal mapping. These results showed that surface charges may play an important role in determining the total capacitance [55].

Coplanar SRRs can be developed into transmission lines [56] and antennas [57], [58], or stacked to create a metasolenoid [59]. A new approach for designing planar metamaterial structures was developed to investigate SRRs and complementary SRRs coupled to planar transmission lines. Baena, *et al*. derived analytic equivalent-circuit models of SRRs to show that stopband/passband characteristics of lines may be interpreted by negative/positive values of permittivity and permeability of the line in the long-wavelength limit [56]. Another study constructed a metamaterial SRR antenna with a very low profile and footprint that achieved an efficiency over 50% with a matched impedance of 50 Ω and a 120 MHz-10 dbm bandwidth [57]. The experimental performance of this system agreed well with Ansoft's HFSS full-wave simulations [57]. An SRR antenna designed using CST Microwave Studio provided two output frequencies: a higher frequency resulting from coupling a monopole radiator with the SRR at 4.59 GHz, and a lower frequency of the original monopole that resonated at 2.69 GHz [58]. HFSS simulations showed that a metasolenoid consisting of stacked SRRs may be modeled as a single particle and could achieve an effective permeability $\varepsilon_{eff} > 10$, over a wide frequency range [59].

Treating the SRRs as inclusions or artificial magnetic inclusions in bulk materials can elucidate the bulk material's response to propagating electromagnetic waves. An effective medium theory showed the relationship between particle responses and a macroscopic system comprised of periodic resonant structures. Using the average permittivity and permeability of each unit cell allows the derivation of a general form of discrete Maxwell equations for the macroscale material to determine the wave modes through the material; theoretically predicted S parameters agreed well with HFSS simulations [60]. Quasi-static equivalent-circuit models for analyzing and designing multiple SRRs, spiral resonators, and labyrinth resonators extended recent models by considering a dielectric substrate with finite resistivity and losses due to the finite conductivity of SRR conductors. The models predicted the resonance and quality factor of the SRR, agreeing well with simulations and measurements [61]. Treating an SRR as an artificial magnetic inclusion showed the limitations of metamaterials based on geometry and physical characteristics. The flatness of permeability as a function of frequency is limited by the desired operational bandwidth of the structure. A circuit-based model yielded geometrically invariant fundamental constants,

which showed that inclusions with large surface area induced higher permeability. Tradeoffs arose when attempting to simultaneously maximize permeability and minimize loss/reducing dispersion for Swiss Rolls and SRRs [62].

Treating the SRR structure as a metacrystal with nonlinear magnetic properties also permits bulk material analysis. A numerical model derived a perturbative solution to the nonlinear oscillator model of an SRR to characterize the nonlinear properties of the metacrystal. The metacrystal used exhibited a nonlinear magnetic response; the effective susceptibilities of the nonlinear magnetic response were evaluated by taking the series expansion to fifth order. The resulting expansion's validity was compared to valid power ranges observed experimentally. The modeled shift in resonant frequencies due to the increased power also agreed well with experimental results [63].

Using SRR structures in waveguides and with NLTLs reduces the noise in the output signal. Payandehjoo and Abhari discussed implementing compact complementary SRRs with a coplanar waveguide-based NLTL frequency doubler to suppress unwanted signals in NLTLs. They validated analytical derivations for the filter design and dispersion characteristics with VNA measurements. The third harmonic suppression was improved and sensitivity to variation of the input voltage level was reduced, producing a narrower signal. This filter increased isolation between the second and third harmonics at an input frequency of 500 MHz. These properties allowed for better single signal isolation. Components of the tank circuit of the distributed filter were determined using the Floquet Theorem; this method may also be applied to distributed amplifiers and mixers [64]. Other studies reported electromagnetic properties of waveguides loaded by complementary electric split ring resonators (CeSSRs) and the application of the waveguides in vacuum electronics. One study calculated the S-parameters of CeSSRs in free space using HFSS software to retrieve the effective permittivity and permeability as well as the dispersion relation and the gain of the wave-beam interaction. Effective medium theory (EMT) was used to calculate the modes of the waveguides as well as the gain. The HFSS results agreed well with EMT. This method improves agreement by fitting the permittivity tensor in the EMT; the gain of the backward wave mode of interaction with the electron beam calculated using HFSS and traveling wave tube theory agreed well with the dispersion method and EMT, respectively [65].

Recent studies have applied SRRs to HPM technology. One study considering metamaterials for HPM applications used an EMT to determine the coupling of an electron beam to a metamaterial structure in a geometry similar to a dielectric Cerenkov maser. The study analyzed negative real permeability, negative permittivity, and double-negative regimes of metamaterials. The authors analyzed SRRs and wire-rod materials by using the 3-D particle-in-cell (PIC) code ICEPIC to determine that the optimum coupling, and thus RF production, occurred in the negative permittivity regime [66]. Another study determined that the small size required for SRRs at higher frequency RF made them inadequate for high power applications due to electrical breakdown at high electric field strengths. While the failure of a single element in an array (short or open circuit) reduced the array's output power, it did not change the resonant frequency. These structures provided a much more compact approach to HPM technology, but further work is required to make them feasible for high energy applications [67]. Some of the high electric fields produced in the SRRs arose due to field enhancement at the edges of the structure, making electrical breakdown a major design risk. One study investigated techniques for reducing the maximum field enhancement factors (MFEF) in different structures. One case study examined a Sievenpiper metasurface, a high impedance meta-surface that consists of periodically arrayed metal patch elements separated from the ground plane by a dielectric substrate and connected to ground by a thin pin through the substrate. A genetic algorithm evaluated negative and low-index metamaterials for field enhancement and presented a quad-beam focusing metamaterial lens with MFEF < 5 over the entire operating band for this metasurface. This approach was applied to negative-index metamaterial (NIM), zero-index metamaterial (ZIM), and low-index metamaterial (LIM) structures [68].

1.2.2 Experimental Contributions

Materials comprised of SRRs provide unique engineering material properties. One composite media composed of SRRs achieved both negative permittivity and permeability and a transmitted bandwidth from 4.6 to 5.2 GHz [69]. The left-handed structure of this material also inverted the Doppler effect, Cherenkov radiation, and Snell's law [69]. Other studies have experimentally determined the material permittivity by examining signal interactions with the materials. One study examined the effective permittivity and permeability of composites containing wires and/or SRRs.

This study demonstrated that wires/SRRs exhibited a frequency regime with negative permittivity/permeability, while combining the two structures yielded a negative component of the index of refraction in the frequency regime with negative permittivity and permeability [70].

Table 2. Summary of SRR technologies.

Study	Resonance Frequency (GHz)	Modeling Method	Gap Loading	Single/Double Ring	Coupling
[10]	5.407-5.84	-	Varactor	Double	Edge
[48]	7.7	CST	-	Double	Edge
[50]	9.75, 10	CST	-	Single	Axial
[53]	~1	MICRO-STRIPES	-	Double	-
[58]	2.69, 4.59	CST	-	Single	Edge
[63]	0.81-0.82/1.15-1.25	CST	Varactor	Single/Double	Edge
[67]	6.125-6.39,12.22-12.55	HFSS	-	Double	Edge
[71]	0.6-0.775	HFSS	-	Double	Edge
[72]	6-9	Analytic Model	PIN Diode	Double	Edge
[74]	3.55-3.85	CST	-	Double	-
[76]	2.44-10.79	Not Stated	-	Double	Edge

The resonant frequency tunability of SRR systems makes them desirable for several applications, including antennas [71], tunable transmission lines [72], and waveguide filters [48]. One study varied the capacitance loaded between the split gaps in the SRR ring and the radial gap distance between the two rings to shift the resonant frequency. Reducing the capacitance increased the resonance and absorption of the SRR. A CST Microwave Studio simulation agreed well with the experimental results [73]. Another study created frequency tunable transmission lines using SRRs. Changing the gaps of the SRRs using PIN diodes, micro-electromechanical system (MEMS), and varactor diodes shifted the resonant frequency by 2.5 GHz [72].

SRR technology has the potential to increase transmission efficiency while decreasing electronics size. Placing an SRR in the near field of the aperture coupled strongly localized EM fields to a radius twenty times smaller than the resonance wavelength, increasing transmission by

740 times by exciting the electric resonance of SRR at approximately 3.55-3.85 GHz [74]. Improved manufacturing techniques provide new possibilities for SRR technology, such as fabrication in silver using nanosphere lithography. Scanning electron microscopy (SEM) showed that these SRRs had typical outer diameters between 100 and 140 nm, inner diameters between 40 and 60 nm, and gap widths between 35 and 40 nm. The measured results agreed well with calculations. The measured *LC* resonance wavelength was 721 nm, compared to the theoretically determined short wavelength limit of 426 nm [75].

NLTLs may be made from an array of SRRs with nonlinear capacitors placed in the gap. One study designed an NLTL system from varactor loaded SRRs to create a voltage controlled oscillator. Controlling the varactor diodes provided more frequency control frequency and creating a stripline [10], [63]. An ultra-wideband monopole antenna with a frequency range from 2.44 to 10.79 GHz was designed using two slotted SRRs. Simulations agreed well with measured data [76]; however, a low voltage breakdown threshold is a major design issue with SRRs, as discussed earlier. Both numerical and experimental studies have assessed the electric breakdown of SRRs under HPM exposure. In one experiment, an SRR combusted when exposed to 1 W at 10 GHz. EM simulation results at 10 GHz using the HFSS 3D full-wave EM field solver were imported into ANSYS to show that the peak temperature exceeded the combustion point of the FR4 PCB material used in the design [77].

SRRs provide a capability for creating metamaterials with unique material properties. While they do not offer a high power capability, they do offer frequency agility for propagating and filtering RF signals. Table 2 summarizes the capabilities of NLTL SRR technologies.

1.3 Nonlinear Bulk Materials

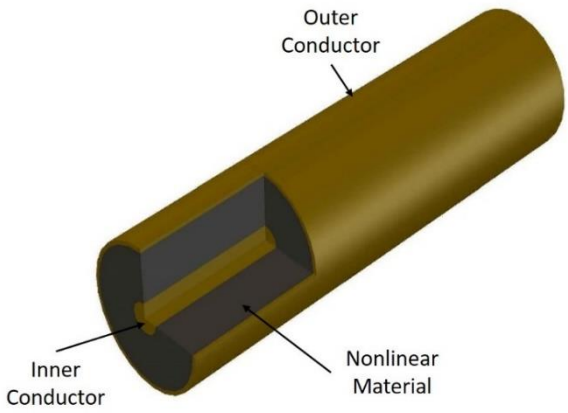

Figure 3. Coaxial nonlinear transmission line with a nonlinear material. Most coaxial or planar designs utilize nonlinear magnetic materials, although this material may also be a nonlinear dielectric or possess both nonlinear dielectric and magnetic properties.

Ideally, NLTLs would simply be made from nonlinear materials; however, characterizing the physical behavior of these materials and designing effective manufacturing processes is challenging. Understanding the physics behind nonlinear material responses under various pulse parameters allows for optimizing designs for both pulse sharpening and RF output. Nonlinear bulk materials may be linear composites with nonlinear inclusions, a large piece of nonlinear electric or magnetic material, or a linear material that acquires nonlinear properties from its geometry such as SRRs. Each approach has been examined theoretically and experimentally to elucidate the behavior of these materials. Figure 3 shows a representative coaxial NLTL with a nonlinear material, which is typically magnetic material with nonlinear permeability.

Nonlinear materials are separated into ferroelectric and ferromagnetic, where the electric polarization may be reversed under an applied electric field or the material has an intrinsic dipole or magnetic moment, respectively. The intrinsic dipole in a ferroelectric material arises from the location of the atoms in the polycrystalline structure. Examples of ferroelectric materials include barium titanate (BT) and barium strontium titanate (BST). Applying an incident pulse to ferroelectric materials stresses the dipole, which will move around the crystalline structure to produce oscillations. The ferromagnetic materials may be biased, as in gyromagnetic lines, to align

the magnetic moments normally in the axial direction. Applying a pulse generates a magnetic field that causes a precession of the magnetic moments to create an RF pulse. The microwave oscillations produced by ferroelectric materials produce lower frequency oscillations than ferromagnetic materials [78].

1.3.1 Modeling Contributions

Nonlinear bulk materials have been studied for over fifty years [79]. Early studies analyzed the rotational model of flux reversal in ferromagnetic materials and their subsequent switching coefficients. This research led to the development of a rotational model based on flux reversal in ferromagnetic materials. Gyorgy theorized that normal materials have a minimum switching coefficient of 0.2 μs [79]. The switching coefficient evaluation can also be performed for NLTLs by investigating lossy NLTL systems. The Runge-Kutta method was used to characterize the coupling phenomenon, phase change, and power due to coupling two lossy transmission lines uniformly with uniform nonlinear shunt capacitances and series inductance [80].

The continuum-limit approximation and Gardner-Morikawa transformation was applied to the lumped element NLTL models from section 2.1 to derive a theory for a nonlinear magnetic lattice. The resulting modified Korteweg-de Vries equation from a four-terminal nonlinear LC network (equivalent circuit for nonlinear magnetic lattice) showed that the soliton, as a model of ferrimagnetic materials, is a solution of this equation; Hirota's method was then used to calculate the interaction of two solitons [81]. Ikezi, et. al. showed that creating a soliton pulse train in a nonlinear-dispersive system can create HPM bursts and proposed developing a modulated transmission line with a nonlinear dielectric [82]. They analyzed nonlinear wave evolution, found nonlinear dielectric parameter requirements to create this pulse, and demonstrated good agreement with some low-power experiments [82]. Other techniques, such as finite difference time domain (FDTD), may be used to calculate wave propagation. Applying FDTD to wave propagation through highly conductive nonlinear magnetic material exhibited good agreement with published numerical results using other approaches [83].

Many studies have investigated various materials to create nonlinear effects. Several NLTL studies have evaluated the effectiveness of ferroelectric materials on NLTLs. One such model that evaluated NLTLs [84] proposed invalid material constraints since it is not bound by the laws of

electrostatics and proposes invalid material constraints. However, other models [82] were physics-based and did not violate basic laws. Crowne developed a Mathematica code based on Kirchhoff's circuit laws that effectively modeled NLTL propagation [85].

These ferroelectric materials can also create nonlinear components for transmission line circuits. Nonlinear ferroelectric capacitors have also been evaluated for other circuit applications, such as creating an effective nonlinear inductance when used as loads for gyrator circuits [86]. Incorporating ZnO microvaristors, as inclusions in a rubber polymer, form composites with nonlinear conductive and dielectric properties. Properties were tuned by adjusting the inclusion concentration, and were predicted using percolation theory [86]. Other ferrites such as spinel, garnet, and hexaferrite have been used to create metamaterials [88]. Ferromagnetic microwires have also been used to create composites that may provide tunable electromagnetic properties by modifying the volume loading [89].

BST and BT are promising nonlinear materials. Crowne's Mathematica code for wave propagation in an NLTL showed promising results using BST [85]. Another numerical study assessed the pulse sharpening of BST and BT dielectric NLTLs, representing the material granularly using Voronoi polygons with a grain boundary model; calculating the capacitance determined material properties such as permittivity [90]. A theoretical model was developed to predict the permittivity of composites comprised of BT fibers with volume fractions between 0.0234 and 0.157. Theoretically predicted permittivity agreed well with measurements from 10 kHz to 10 MHz [91].

Although composite dielectric properties may be modeled in numerous ways [92]– [94], two main techniques have been applied for metamaterials. One is microscopic theory, where the parameters of each element are averaged to create a metamacroscopic property. This is used when the system properties are already known [95]. When the properties are unknown, the effective parameters must be determined using scattering parameters or transfer matrices. Numerical simulations may also be used once the initial parameters are known for parts of the system. One numerical approach used a Green's function derived for nonlinear materials. Experimentally, nonlinear media have been created using SRRs in combination with nonlinear components. Using a nonlinear host material or substrate like GaA gave a higher output frequency. Small components

with large field enhancement, such as SRRs and metal rods with high aspect ratio, significantly increased device nonlinearity [95].

One microscopic approach statistically modeled conductivity and inclusion aspect ratio distributions using the Maxwell Garnett mixing rule by treating the inclusions as conducting spheroids at a concentration below the 5% percolation threshold. Assuming a Gaussian distribution of 0.4 to 4% volume loading of carbon inclusions in Teflon, the authors used Maple 10 software to calculate complex effective permittivity [96]. This study showed that the average aspect ratio and conductivity were the main factors in the composite effective permittivity at microwave frequencies [96]. Another study used HFSS to calculate scattering parameters to create an effective-medium model from the zero-scattering condition for calculating frequency-dependent effective permittivity and permeability of metamaterials. The model used a dipole approximation with no additional long-wavelength approximations. It also captured the effects of spatial dispersion and predicted finite effective refractive index and antiresonances in agreement with finite-element calculations [97]. The resulting high frequency mixing rule agreed well with the Maxwell Garnett mixing rule and yielded scattering parameters for composites similar to metamaterials of SRRs or particles arranged in a fishnet structure [98].

Multiple studies have recently examined wave motion through nonlinear materials in an NLTL configuration. One study modeled wave propagation in an NLTL using the derivative nonlinear Schrödinger equation with constant potential in the small amplitude, long wavelength limit, noting that some exact elliptic solutions showed mirror or rotational symmetry [99]. Another study investigated stationary solutions in the form of traveling EM waves in a uniform transmission line with saturated ferrites and no damping. This model showed that the period of linear oscillations increased linearly with current, while the group velocity of stationary waves increased with oscillation amplitude. Increasing the external magnetic field increased the asynchronicity of the oscillation [100]. An analytical model supported by SPICE circuit simulations was derived to study the wave propagation though a gyromagnetic line, specifically pulse rise time compression, by changing NLTL parameters. Several models were used with various parameters: Weiner and Silber's model, a simplified theory on pulse sharpening, had an input of 6 kV and 40 ns rise and fall times; Pouladian-Kari *et al.*'s model, which calculated the reduction of the output rise time due to the decrease in permeability, had an input of 12 kV and a

3.5 ns rise time; and Dolan and Bolton's model had an input of -10 kV with a rise time of 2 ns and produced 5 GHz oscillations. The numerical analysis was performed using Mathematica [101].

Wave sharpening, oscillation generation, and wave propagation can be modeled very accurately by using FDTD to solve the Landau-Lifschitz equations, given by

$$\frac{\partial M}{\partial t} = -\gamma \mu_0 M \times H + \frac{\alpha \mu_0}{M_s}\left[M \times \frac{\partial M}{\partial t}\right], \tag{2}$$

where H and M are the magnetization and total magnetic field vectors, respectively, μ_0 is the permeability of free-space, M_s is the value of the saturated magnetization, γ is the electron gyromagnetic ratio, and α is a dimensionless damping parameter. A model simulating the conversion of a DC pulse into a quasi-monochromatic RF pulse agreed well with the synchronous wave model. The study showed that the central frequency of the wideband pulse produced by the NLTL did not depend solely on the precession of the magnetic moments. The total coaxial NLTL diameter, ferrite core size, line spatial filling, and center frequency electric and magnetic parameters were also affected by the eigenmodes in the line and their associated frequencies and dispersion [102].

1.3.2 Experimental Contributions

Nonlinear dielectrics have been incorporated into transmission lines for over thirty years [2], [34], [82]. Using various dielectrics and geometries gave a broad range of shock forming lines [103], NLTLs for pulse sharpening, or RF sources. Ferrite loaded coaxial lines were used to produce sub-ns high voltage pulses through magnetic compression [103]. Early research examined issues with various geometries for NLTL design. Since coaxial geometry generates nonuniform fields, some researchers decided to use parallel plate geometry for a shock forming line. The authors also found that BST could achieve a very high relative permittivity (~8000-13 000), making it ideal for NLTLs. Experiments with BST achieved a shock wave amplitude of approximately 13 kV with a rise-time of 7 ns. At the load, 20-30% of the shock wave amplitude was reached in 20 ns with rise times of 700 ps or less (measurement sensitivity limited rise time determination for faster rise-times) [104].

While this review mainly focuses on using NLTLs as solid state RF generators, one useful application of NLTLs is for pulse compression [105]. Recently, a two-stage magnetic compressor based on gyromagnetic NLTLs converted a 7 ns duration, 500 kV amplitude input pulse into a 30 GW peak power output pulse with 0.65 ns duration,1.1 MV amplitude pulse with a repetition rate of 1 kHz [106]. Another system used a single, 30 cm long NLTL with an axially biased magnetic field of 22 kA/m to sharpen a 70 kV input pulse to a final rise time of 350 ps with an amplitude > 90 kV at a 1 kHz repetition rate [107]. More recently, nonlinear ferrite lines sharpened a 4 ns full-width half-maximum (FWHM) -500 kV pulse to 45 ps -850 kV pulse with an increase rate of the leading pulse of 15.5 MV/ns [108]. An axial bias field was added to produce microwave frequency of 3-3.7 GHz pulses with a 65%-85% modulation depth, although the repetition rate was limited to 1 Hz due to high electric fields in the line [108].

Researchers have used other nonlinear materials to create NLTL RF sources. One study used saturated NiZn ferrite to construct an NLTL with output oscillations at 1 GHz for bursts of 1000 pulses at 200 Hz repetition rate. A 1 m coaxial line sharpened a 250 kV pulse with a 2.5 ns rise time to 0.5 ns rise time, with RF pulse duration of 4-5 ns and a peak power of 260 MW [11].

More recently, NLTLs have been used to construct solid state RF sources with high repetition rates using solid state switching technology. A 50 kV 4H-SiC photo-conducting solid state switch triggered with a 3 mJ Nd:YAG laser switched a capacitive discharge circuit into an NLTL, comprised of ferromagnetic pieces in a coaxial geometry. The resulting pulse had a FWHM of 7 ns with a 2 ns rise time and repetition rate up to 65 MHz. This generated 2.1 GHz microwaves with 50 Ω system impedance [109]. This line achieved peak powers over 30 MW with a 30 kV incident pulse. The RF power output reached 4.8 MW peak, with an RF pulse length ranging from 1-5 ns. The NLTL operated in S-band, with about 30% bandwidth. Varying the nonlinear material's bias magnetic field established active delay control. Tuning the NLTL's magnetic bias varied the system's electrical delay between 9 ns and 20.5 ns [110]. Adjusting another NLTL's bias field tuned its frequency from 0.95 to 1.45 GHz. Circuit models and frequency domain simulations supported these experiments. A Marx generator provided 25 ns pulses with a 5 ns rise time, voltages up to 260 kV, peak power levels above 100 MW, average power levels of tens of MW, and 4-17 ns RF pulse duration. The output transition line provided 14 ns of transit time isolation from potential interference from the reflected pulse from the load [111].

NLTL RF outputs can be combined and controlled in various ways. One RF source used a gyromagnetic NLTL comprised of NiZn ferrites to generate MW-level power for L, S, and C microwave bands. A bias field controlled delay power combiner was designed for these bands. COMSOL was used to model the combiner to determine its functionality and power limits. The combiner joined two 50 Ω coaxial inputs to a single tapered transition with a final output impedance of 50 Ω. The NLTL output frequency was between 1.8 and 2.6 GHz [112]. Another study aligned a coaxial, four-element NLTL antenna array by placing adjustable, temporal ferrimagnetic delay lines serially in front of the main NiZn ferrite loaded gyromagnetic NLTL. Delay line propagation velocity adjustability was achieved by varying its bias voltage or external DC magnetic field [113]. Connecting one high voltage driver to two gyromagnetic NLTLs provided electronically controlled beam steering. Each NLTL produced several ns RF pulses with peak power from 50 to 700 MW. The generated frequencies ranged from 0.5 to 1.7 GHz at a repetition rate of 100 Hz. A helix antenna radiated RF pulses with near-circular polarization at 350 MW peak power level. The input pulse rise times were approximately 2-3 ns [114]. Since some NLTLs cannot produce high output power, combining the output of multiple NLTLs has been of great interest. We previously described a solid state, four-element array gyromagnetic NLTL comprised of NiZn ferrites with frequency adjustable between 2-4 GHz using a magnetic field with a repetition rate of 1 kHz and a power of 4.2 MW. This four NLTL system used phase control to create an additive effect on the RF output that lasted ~ 2 ns [115].

Other parallel gyromagnetic NLTL phase adding was accomplished by using a solenoid to create a magnetic field. amplitude -430 kV, 5 ns input pulse produced oscillations that reached 175 kV at the NLTL output, with a frequency of ~4 GHz and an electric field of 250 kV/m at 3 m distance, at a repetition rate of 1 kHz. The NLTLs were made of NiZn rings, yielding an RF output 2-4 ns in duration [116]. More recently, Ulmaskulov *et al*. demonstrated NLTL summation by combining four ferrite based NLTLs that produced 8 GHz pulses with an input nanosecond pulse of -195 kV, at a repetition rate of 5 Hz, for a total duration of 20 s [117]. Others coupled NLTLs, combining the output using an external bias. The application of high voltage nanosecond pulses generated 1 s packets of 1000 Hz RF from the output of the four channels. The RF had a pulse amplitude of 175 kV, generating an effective frequency of approximately 4 GHz for the NiZn ferrite NLTL [8]. Four coherent gyromagnetic NLTLs produced 2.1 GHz pulses with an effective

potential of 360 kV at the radiation axis, at a repetition rate of 1 kHz. A variation of 17° through beam steering was demonstrated in the horizontal plane [118].

Other nonlinear materials have been explored. The permittivity and permeability of barium titanate-ferrite was examined for application in a nonlinear capacitor exhibiting nonlinearity under high voltage pulses. The metamaterial and insulation of magnetic particles with a dielectric layer were tested [119]. Another study constructed a stripline gyromagnetic NLTL from yttrium iron garnet ferrite. The RF source operated at 40.1% average bandwidth and 2-12.7 MW peak power [120]. $Na_{1/2}Bi_{1/2}Cu_3Ti_4O_{12}$ ceramics were examined for dielectric tunability. The resulting Schottky and Langevin effects achieved ~70% tunability at room temperature for a 200 V/cm field. The positive tunability could be switched to negative tunability by 10% overdosing of Bi [121]. Another metamaterial, nanocomposite $Ag/Zr_{0.9}Ni_{0.1}O_y$, was interrogated with a quadrupole electrode AC electric field. The Ag nanoparticles aligned parallel to the electric field. The surface was evaluated using x-ray diffraction, SEM, and transmission electron microscopy. A frequency scan of a nanocomposite capacitor measured permittivity, while permeability was determined by wrapping a wire around the composite and measuring the wire's inductance during a frequency scan from 0 to 10 GHz; these measurements showed potential for the nanocomposite to be a double negative material [122].

The maturation of NLTL technology has raised other potential applications of the technology. One study examined the effects of RF pulses with a ns envelope on biological samples. The RF pulse amplitude was varied by 52 dB with about 40 kV/cm maximum output field, 4-25 ns pulse duration, and 0.6-1.0 GHz frequency [123]. Other researchers operated a gyromagnetic NLTL as a peak power amplifier of an input pulse, with similar pulse duration, and most of the input energy transmitted to the first oscillation peak. Experiments applied a 500 kV, 7 ns half height pulse duration pulse with about 300 MHz frequency input to the NLTL, yielding a 740 kV, 2 ns duration output, and 6 to 13 GW amplification [124]. Using the NLTL in a high current environment permitted its use in a gigawatt class electron beam driver. Experiments showed 0.95-1.45 GHz peak frequencies and 5-35% amplitude modulations depending on the setup [125]. This GW-class electron beam was simulated using PIC and measured waveforms from a synchronous wave ferrite NLTL to demonstrate its practicality. Simulations coupling the modulated beam to a

disk-on-rod slow wave structure (SWS) increased extractable RF ten times compared to direct extraction from an NLTL [126].

Recent studies utilized different ferrites and insulating materials for spatially dispersive NLTLs. One study replaced transformer oil with SF_6, which increased the RF output power by approximately a factor of four at frequencies exceeding 1.2 GHz; however, the peak power decreased at the center frequency. The output frequency range of the NLTL increased from 800 MHz - 1.4 GHz for transformer oil to 900 MHz- 1.8 GHz for SF_6. The highest power output for the transformer oil NLTL with an input pulse of 34 kV was ~ 230 MW at ~ 1 GHz, while the peak output power using SF_6 for the same input pulse was ~200 MW at 1.4 GHz. Also, increasing the ferrite volume loading in the NLTL increased permeability from 16 to 800, more than peak power generation [127].

NLTLs utilizing nonlinear dielectric or nonlinear magnetic materials provide a solid state HPM option. Phasing multiple NLTLs increases power and steerability without mechanical components. The lack of auxiliary systems, such as vacuum pumps, greatly reduces the physical footprint of these systems and increases power density. Output frequency is determined by the nonlinear material used; NLTLs using nonlinear dielectric materials yield less than 100 MHz, while NLTLs using nonlinear magnetic materials produce up to 8 GHz. Researchers are on the verge of producing GW class systems that can rival traditional vacuum HPM systems. Table 3 summarizes NLTLs designed using nonlinear material.

Table 3. Summary of NLTLs designed with nonlinear materials.

Study	Input Pulse Amplitude (kV)	Input Pulse Duration (ns)	Repetition Rate (kHz)	RF Generation Frequency (GHz)	RF Generation Output Peak Power (MW)
[8]	-175	5	1	4	-
[11]	250	10	0.2	1	260
[109]	20-25	7	65,000	2.1	-
[110]	30	1-5	-	2-4	4.8
[111]	260	25	-	0.95-1.45	100
[114]*	240	2-3	0.1	0.5-1.7	50-700
[115]*	-40	-	1	2-4	4.2
[116]*	-430	5	1	4	166
[117]*	-195	1	0.005	8	-
[118]*	-200	5	1	2.1	344
[120]	35-55	-	-	0.62-0.96	2-12.7
[121]	150-190	-	-	0.8-1.8	50-200

* combined output

1.4 Hybrid NLTLs

The above research generally studied NLTLs that achieved their nonlinearity using either a nonlinear permittivity or a nonlinear permeability; however, recent research has investigated hybrid NLTLs that exhibit both nonlinear permittivity and permeability. Hybrid NLTLs were created using a SPICE simulation and experiments to create a chaos generator, potentially valuable for modeling naturally occurring phenomena. The nonlinear circuit equations were solved using the Runge-Kutta method [1]. SPICE was used to simulate the frequency generation above 800 MHz using a hybrid line using varactor diodes as nonlinear capacitive elements. The system had 10 V applied voltage, 50 Ω impedance, and input pulse parameters of 5 V amplitude, 40 ns rise time, and 50 ns FWHM pulse width. The rise time decreased to 18-22 ns using proprietary ferrites; simulations showed about 800 MHz output frequency, with proposed 1-2 GHz using proprietary ferrites (BAE Systems, UK). The authors also demonstrated how utilizing a hybrid NLTL

produced a longer, 15 ns RF envelope compared to ~7 ns RF envelope for NLTLs with only nonlinear capacitance [2][128].

A numerical model for a lumped element hybrid NLTL used the Korteweg-de Vries equation. This analysis agreed well with experiments, which used COTS nonlinear inductors and nonlinear capacitors which varied exponentially with current and voltage, respectively. The output frequency of the modeled hybrid line was 50% greater than similar NLTLs with only nonlinear capacitance or nonlinear inductance. Modeling the hybrid NLTL showed the frequency double over a 5V increase in the voltage bias. [3]. A hybrid NLTL was constructed of COTS components was tested with a rectangular input pulse with a 6 kV input voltage, 600 ns pulse width, 47 ns rise-time, and 44 ns fall-time, using a storage capacitor and a fast semiconductor switch. Component nonlinearity was evaluated to determine line impedance change to match the load and prevent reflections. The RF produced by the line varied between 55 MHz and 80 MHz for 5 kV and 8 kV pulse voltages, respectively. The power output of the line peaked at around 5 kW for a 40 Ω load. Simulations using a code developed by the researchers matched well with the experimental results [4].

A more recent study constructed two 30-section hybrid NLTLs with BT dielectrics nonlinear capacitors, 2.2 nF or 10 nF unbiased capacitance, and ferrite bead inductors. A 1 kV input pulse applied to the lines generated a 33 MHz output. The voltage modulation depth of the output signal was 700 V for the NLTL with the 2.2 nF capacitors and 200 V for the 10 nF capacitors. Ten RF cycles were produced for each input pulse applied to the lines. The authors showed that the hybrid NLTLs produced a higher voltage modulation depth compared to lines with a single nonlinear component [5][129].

Other studies evaluated hybrid NLTLs as soliton generators, developing a model based on a modified Korteweg De-Vries equation and SPICE simulations.

Compared to traditional NLTLs using only nonlinear capacitors, hybrid lines produced more oscillations, although at lower voltages. For instance, the traditional NLTL produced a single peak with 8V amplitude, while the hybrid NLTL produced three solitons with the highest peak at 4 V and the lowest peak slightly less than 2 V. The numerical model developed by the authors matched well with SPICE simulations [6][130].

1.5 Conclusion

NLTLs have a promising future as valuable solid state RF sources. NLTLs may be designed using different modalities with unique advantages and disadvantages. Table 4 compares key parameters of the NLTL topologies.

Table 4. Comparison of key NLTL parameters for various designs.

	Lumped Element NLIL	Lumped Element NLCL	SRR	Nonlinear Material	Hybrid NLTL
Frequency (GHz)	0.7-1.3	0.01-0.2	2.44-12.5	0.95-8	0.8-2
RF Pulse Width (ns)	400	300	-	1-25	500
Peak Power (MW)	20	0.008	5×10^{-9}	4.8-700	0.005
Maximum Input Voltage (kV)	43	50	0.001	430	6
Nonlinear Element	L	C	C	L	L&C

NLIL = Nonlinear Inductive Line; NLCL = Nonlinear Capacitor Line; SRR = Split ring resonator

The lumped element approach allows for a more modular configuration that may be used at higher voltages due to circuit design and higher voltage components. However, the lumped element approach can become physically large when adding more stages at higher voltages and the NLTL output is not as tunable as other designs. The Bragg cutoff frequency limits the output frequency of lumped element designs to less than 250 MHz, for diode based systems, and even lower for capacitor based systems. The SRR approach provides a narrowband structure that can be used as an NLTL by adding nonlinear components or a nonlinear substrate. The frequency can be changed by illuminating the gaps during operation; however, this may be impractical for a mobile system. The SRR approach is limited in power due to the small structure size required for the desired RF output frequencies. SRRs are more practical as waveguide filters or steerable antennas, although they could provide compact low power RF generators. NLTL designs with nonlinear materials enhance device compactness and provide some frequency flexibility by changing the NLTL's bias. This approach also allows for creating phased arrays for potential power combination and beam steering. However, unless combined with other devices such as an SWS, the nonlinear material approach limits the power output compared with the lumped element

method [111]. The RF envelope of these devices has been an issue; most RF pulses were on the order of a few ns, although hybrid NLTLs may potentially extend this operating range [128]. Hybrid NLTLs also provide a unique capability for matching modulators to antennae in system designs through controlling both nonlinear permittivity and nonlinear permeability to achieve a more constant impedance. Table 5 shows the best NLTL topology for optimizing frequency, RF pulse width, peak power, ease of construction, and load matching.

Table 5. Optimal NLTL topology for a given parameter.

	Lumped Element	SRR	Nonlinear Material	Hybrid NLTL
Frequency		x		
RF Pulse Width				x
Peak Power			x	
Ease of Construction	x			
Load Matching				x

Nonlinear material based NLTLs are optimal for high power RF generation because of phase coupling. SRRs are optimal for a low power, high frequency RF generator or antenna where combining the output produces directivity. Lumped element NLTLs are best suited for mid-range power applications due to component limitations. The ability to utilize nonlinear inductance and capacitance in the lumped element topology allows for more design customization.

Current research focuses on overcoming the challenges when incorporating NLTLs into a system with limited power availability and combining NLTLs with a matched antenna to mitigate loss and reflections. Researchers are exploring the addition of coaxial ceramic rings to gyromagnetic NLTLs to improve their efficiencies, typically around 10%. Adding rings with a permittivity of 50 increased the overall line permittivity from 3.8 to 5.9, which increased the output from 35 kV to 50 kV and shifted the output frequency from 1.25 GHz to 1.17 GHz [131]; further optimization could increase the NLTL efficiency from 10% to over 40%. Researchers have also

investigated RF power extraction from an NLTL by using a resistive load to optimize the output. Theoretical models and SPICE simulations of efficiency agreed well with experimental results [132]. This work will be crucial for extending NLTL designs to LC loads more comparable to some antenna designs.

In summary, we have reviewed the three main topologies for NLTLs. Lumped element and nonlinear material designs are promising for HPM applications, while SRR designs are more applicable for lower power systems and antenna applications. NLTLs are a promising technology for providing high power (>100 MW), high frequency (>1 GHz), and high repetition rate (>1 kHz) solutions in a solid state package, while greatly decreasing the need for auxiliary systems required compared to traditional HPM technology. Current research demonstrates the feasibility of increasing the frequency of nonlinear capacitor-based lines simultaneously with increasing power output and efficiency. Ongoing advancements in solid state switch technology will make the application and optimization of NLTLs more important in future HPM system development.

2. MATERIAL PROPERTIES OF COMPOSITES WITH BARIUM STRONTIUM TITANATE OR NICKEL ZINC FERRITE INCLUSIONS FROM 1 TO 4 GHZ

2.1 Introduction

This chapter was publish in Composite Science and Technology, see Ref. [179]. Nonlinear transmission lines (NLTLs) are of great interest as a solid state high power microwave source (HPM) [3], [133]. The potential to provide a reliable, solid state, high repetition rate, wide band HPM system allows for a more compact source. The main shortcoming for NLTLs compared to conventional vacuum sources is the peak output power, which is limited by the dielectric materials used in the device. NLTLs utilize nonlinear dielectric materials to sharpen an input pulse to the point of generating an electromagnetic shockwave [3], [33]. This resulting shockwave generates microwave oscillations through different mechanisms depending on the nonlinear property that produces them.

NLTLs that use ferromagnetic materials, whose (magnetic) permeability depends on the applied and induced magnetic fields, are referred to as gyromagnetic lines. Once the electromagnetic shockwave forms in the NLTL, the magnetic moments will precess around the effective magnetic field [1], [109]. An alternative approach uses ferroelectric materials, whose permittivity depends on the applied and induced electric fields, such as barium titanate (BT) [35], [78] or BST [104]. The crystalline structure of these titanate ceramics generates a permanent dipole while the material is in the ferroelectric state. Once the material exceeds the Curie temperature, the material enters into a paraelectric state where the permanent dipole is removed [78]. The motion of this dipole after the electromagnetic shockwave has formed is the source of the oscillations in the ferroelectric materials. The output frequencies are also affected by the source of the oscillations, making the output frequencies for ferroelectric materials much lower than those of ferromagnetic materials [178].

This study evaluates the change in permittivity and permeability of composites with either BST or NZF inclusions to guide future NLTL designs using composite materials. Composites have been used for various applications, such as electromagnetic interference (EMI) shielding and high energy density capacitors. The inclusion shape and material have been shown to play an important role in the composite properties. The use of stainless steel rods with high aspect ratios proved well

suited for EMI shielding materials where a volume fraction of 2-3% was sufficient to reach percolation [93],[94],[134]. Other studies have shown that increasing the aspect ratio with the same volume fraction of BT increases the composite dielectric constant [135], [136]. The inclusions used for the high energy density capacitors were ferrite cores coated with BT. This was done to increase the effective permittivity of the dielectric used in the capacitor to increase the energy density [92],[137].

Previous studies have evaluated BT composites while adjusting the volume fraction and other inclusions to determine the variation of dielectric properties with volume fraction [138]-[144]. These studies showed that the relative permittivity of the composites increased with volume fraction of BT over their measured frequency range. Studies have also showed that BST composites [145-148] and other titanate inclusions [149], [150] exhibit the same trend of increasing relative permittivity with increasing volume fraction. Composites with ferrite inclusions [137], [151-154], some with additional inclusions such as BT and BST, behave similar to BT and BST composites; however, the increase as a function of volume fraction is far less due to the lower permittivity of the ferrite inclusion. Adding ferrite inclusions produces new materials that contain a magnetic component that also increases with increasing volume fraction.

The dielectric and magnetic properties of the composites have been measured using various techniques, including resonant chambers [155], [156], LCR meters [138], [139], [141], [142], [144], [148], [154], [157], [158], coaxial airlines coupled with vector network analyzers (VNAs) [137], [149], [151], [152], impedance analyzers [140], [142], [146], [147], [150], [153], [157], [159] and VNAs coupled with waveguides [143], [145]. Resonant chambers measured properties between 1 MHz and 1.8 GHz [155] and at specific frequencies 6.62, 6.69, and 11.5 GHz [156]. Measurements made using LCR meters ranged from 20 Hz [141], [148] to 30 MHz [154], [158]. Coupling a coaxial airline with a VNA can measure electromagnetic properties from 10 Hz [149] to 4.5 GHz [152]; however, the sample length depends on the evaluation frequency. Impedance analyzers have been used to measure from 10^{-4} Hz [159] to 1 GHz [140],[147]. Using a VNA coupled with a waveguide can measure dielectric properties at frequencies from 8 GHz [143] to 18 GHz [143],[145].

This study evaluates the dielectric and magnetic properties of composites containing various volume fractions of either BST or NZF inclusions from 1 to 4 GHz using a coaxial airline coupled with a VNA. We measured four samples at each volume fraction to characterize the

reproducibility of the manufacturing process and statistical significance of material property variation with changes in volume fraction. Section 2.2 summarizes the composite manufacturing composite for each matrix and the test procedures for determining the dielectric and magnetic properties and dielectric breakdown strength of the composites. Section 2.3 describes the results of these experiments. The composite dielectric breakdown strength and resulting Weibull statistics are reported in Section 2.4. We discuss the results and make concluding remarks in Section 2.5.

2.2 Methods

2.2.1 Composite Manufacturing

The composites were manufactured using a silicone elastomer two-part encapsulation medium (Sylgard 184) with BST (TPL Inc. HBS-8000) or NZF (Powder Processing & Technology FP350) powders. The BST powder had a ratio of 67% barium to 33% strontium with an average particle diameter of 600-800 nm. The NZF powder particle Dv50 (average particle diameter) was 10 μm. Scanning electron microscope (SEM) images of the powders are shown in Figure 4. We mixed volume loadings of the powder from 5% to 25% in 5% increments.

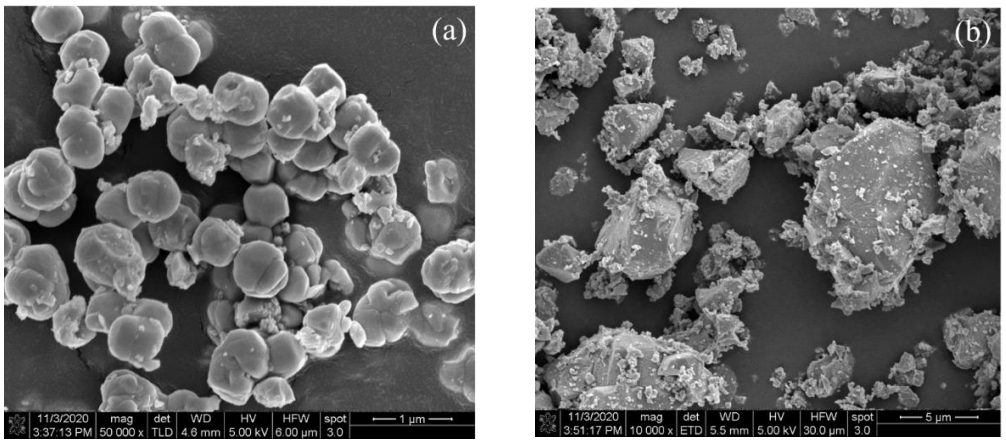

Figure 4. Scanning electron microscope (SEM) images of (a) barium strontium titanate (BST) and (b) nickel zinc ferrite (NZF) powders.

We first measured the mass of the silicone elastomer base and then calculated the mass of the desired volume fraction of either the BST or NZF powder. After stirring by hand for five

minutes to combine the mixture, we placed it in a planetary centrifuge (Thinky Mixer AR-100) for five minutes. BST composites were then placed in a bath sonicator (Crest Ultrasonics CP200HT) for four hours to disperse any conglomerations of the fine powder. Next, the sample was placed in the planetary centrifuge again for five minutes to ensure thorough mixing of the composite. We then removed the sample and added the curing agent to the mixture at 10% of the mass of the silicone elastomer base. After mixing in the curing agent by hand for five minutes to start the curing process, we placed the sample in a vacuum chamber (Medline Scientific Jeio Tech 665L Vacuum Oven OV-12) at 0.1 MPa below atmosphere for 30 minutes to degas the sample. Using a syringe and tubing, the sample was then transferred to a mold, which was filled from the bottom to limit the addition of air to the mixture. Next, the sample and mold were placed in the vacuum chamber to outgas for an additional five minutes. After securing the mold with the mixture inside, the mold was placed into a laboratory convection oven (Blue M LO-136E) at 100°C for two hours to cure.

Before each sample fabrication, the mold was placed in a bath sonicator with a mild detergent at 60°C for two hours to clean it and remove residual material. The mold was then dried with compressed air and sprayed with a silicone mold release. We next spread the mold release over the surfaces using a paint brush to ensure an even, thin coating of the mold release. After removing the sample from the mold, we cleaned the mold again using acetone and Kimwipes. Representative samples with BST or NZF inclusions are shown in Figure 5.

Figure 5. Composite samples containing (left) barium strontium titanate (BST) and (right) nickel zinc ferrite (NZF) inclusions. The quarter is included for scale.

2.2.2 Dielectric Measurements

The dielectric properties were measured using a network analyzer (Keysight FieldFox Handheld Microwave Analyzer N9913A) connected to a coaxial airline (Keysight Type-N 50 Ω Verification Kit). The measurements were conducted with the equipment and cables secured to an anti-static mat while the user wore an anti-static wrist strap. We performed a full two port calibration using an open, short, and matched 50 Ω load to calibrate the VNA receivers for both ports (Keysight 85054D Economy Mechanical Calibration Kit, DC to 18 GHz, Type-N, 50 Ω). The airline was connected to port 2 to eliminate any loss associated with the airline from 1-4 GHz. All connections were made using a torque wrench and tightened to 135 N-cm to ensure secure connections. The airline was cleaned using 70% isopropyl alcohol and Kimwipes (KimTech) to remove any residue on the center connector and the interior of the coaxial airline.

We placed the samples on the center conductor of the airline and used digital calipers to determine the length and diameter of the sample. The sample length was chosen to be at least $\lambda_l/4$, where λ_l is the wavelength of the electromagnetic signal corresponding to the lowest frequency measured (1 GHz). After placing the samples in the coaxial airline, we measured the distance from the end of the center conductor to the sample using digital calipers so that the software could make corrections when calculating the complex permittivity and permeability. The airline was then connected to the system using the aforementioned torque wrench to ensure proper connections.

The composite permittivity and permeability were calculated from the S-parameters using the Keysight Material Measurement Suite (Keysight N1500A) Transmission Line and Free Space Module. We used a frequency range 1-4 GHz with the power set to -15 dB and the intermediate frequency band width (IFBW) set to 1 kHz. We selected 601 points and averaged the output over ten scans. We calculated the permittivity and permeability using the iterative technique "Polynomial Fit Reflection/Transmission Mu and Epsilon" to fit the measured S-parameters [44]. This approach was specifically derived for magnetic materials, so we used it for all measurements for consistency in analyzing the result for both BST and NZF composites.

2.2.3 Statistical Analysis

We performed a one-way analysis of variance (ANOVA) on the measured real permittivity and permeability and applied a multiple comparison test utilizing the Tukey-Kramer method, which is optimized for balanced one-way ANOVA tests with equal sample sizes, to the ANOVA test output to determine the statistical significance with changes in volume fraction of the BST or NZF inclusions at each measured frequency. We used $p < 0.05$ to indicate a statistically significant difference between two measurements.

2.2.4 Dielectric breakdown measurements

The dielectric strength of the composites was evaluated using a 200 kV DC Hipot tester (High Voltage Inc. PTS-200). The samples were placed in a sample holder (cf. Figure 6a) to prevent surface flashover around the material. The sample holder was then placed in a test fixture (cf. Figure 6b), where the electrodes were aligned using holes in the sides of the test fixture. The electrodes consisted of a flat surface in the center with a large radius of curvature on the edges to mitigate any field enhancement that would occur. The voltage was increased at 2 kV/s. We tested four samples for each volume fraction and measured the thickness using a digital caliper.

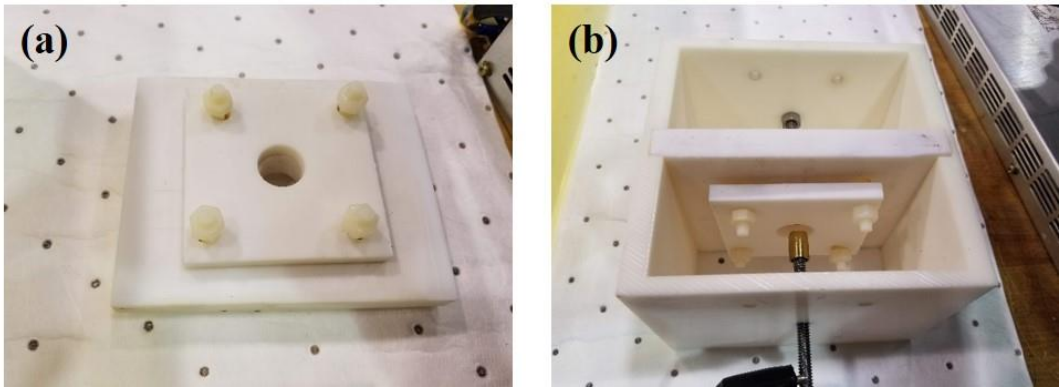

Figure 6. Experimental setup for the dielectric breakdown measurements, including the (a) sample holder and (b) test fixture.

2.3 Dielectric Property Measurements

2.3.1 BST Measurements

Figure 7 reports the real permittivity for BST composites as a function of volume fraction as the average of four samples for each volume fraction with the error bars determined using standard deviation. The relative permittivity of the composite increases with increasing volume fraction and is fairly constant across the frequencies of interest. ANOVA and Tukey tests show that $p < 0.05$ for all changes in volume loading, indicating that any changes in the volume loading of BST will induce statistically significant changes in ϵ_r. The real permeability μ_r of the composites remains relatively constant ($\mu_r \approx 1$), indicating that the composite is nonmagnetic, as anticipated. For μ_r, $p > 0.05$ for all changes in volume loading, indicating that the measurements do not differ significantly from one another, as expected since neither the BST inclusions nor the PDMS matrix are inherently magnetic.

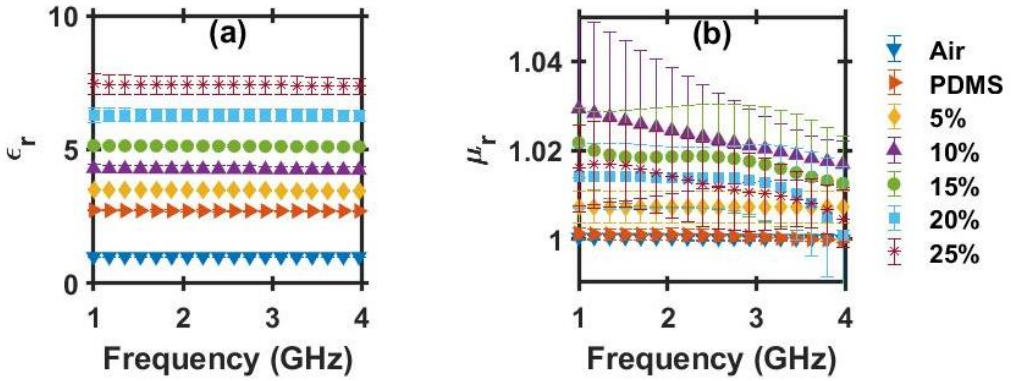

Figure 7. The real (a) permittivity and (b) permeability of composites containing PDMS and various volume loadings of barium strontium titanate (BST) reported as the average of four different samples with error bars determined using standard deviation. The error bars for air, PDMS, and 5% BST are approximately the same size as the lines.

The dielectric and magnetic loss tangent are given by

$$\tan \delta = \frac{\epsilon_i}{\epsilon_r} \tag{2-1}$$

and

$$\tan \delta_m = \frac{\mu_i}{\mu_r}, \tag{2-2}$$

respectively, where ϵ is the permittivity, μ is the permeability, and i and r are the imaginary and real components, respectively. The standard deviation for the dielectric and magnetic loss tangents may be determined using error propagation [161],[162] to obtain

$$\sigma_{\tan \delta} = \sqrt{\left(\frac{1}{\epsilon_r}\right)^2 \sigma_{\epsilon_i}^2 + \left(\frac{\epsilon_i}{\epsilon_r^2}\right)^2 \sigma_{\epsilon_r}^2} \tag{2-3}$$

and

$$\sigma_{\tan \delta_m} = \sqrt{\left(\frac{1}{\mu_r}\right)^2 \sigma_{\mu_i}^2 + \left(\frac{\mu_i}{\mu_r^2}\right)^2 \sigma_{\mu_r}^2}, \tag{2-4}$$

respectively, where $\sigma_{\epsilon_i}^2, \sigma_{\epsilon_r}^2, \sigma_{\mu_i}^2$ and $\sigma_{\mu_r}^2$ represent the variances of $\epsilon_i, \epsilon_r, \mu_i$, and μ_r, respectively. Figure 8 shows the dielectric and magnetic loss tangents.

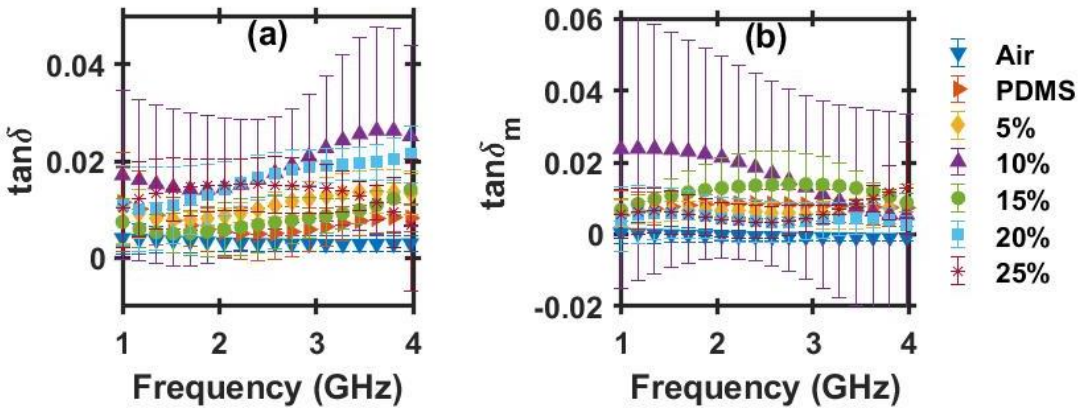

Figure 8. The (a) dielectric loss tangent tanδ and the (b) magnetic loss tangent tanδ_m of composites comprised of PDMS (silicone) and various volume loadings of barium strontium titanate (BST). The results reported are the average of the measurements of four samples with error bars reported as the standard deviation.

The low values of electrical loss tangent ($\tan\delta < 0.015$ except for the 10% and 20% volume fractions at frequencies >2GHz) make it reasonable to consider these composites as low loss materials. These materials may also be considered low loss magnetically ($\tan\delta_m < 0.015$ except for the 10% volume fraction below 2.75 GHz).

2.3.2 NZF Measurements

Figure 9 shows the measured real permittivity and permeability for composites consisting of PDMS and various volume loadings of NZF inclusions with data reported as the average of four samples and error bars determined by standard deviation.

Figure 9a shows that ϵ_r increases with NZF volume fraction and is essentially constant with frequency. Figure 10 shows the analysis of the statistical significance of these changes using a one-way ANOVA. Changing the NZF volume fraction induced statistically significant changes in the composite's permittivity ($p < 0.05$) in most cases, except for 5% to 10%, 10% to 15%, and, in a less significant way, 5% to 15% at higher frequencies. The slight changes for these exceptions shows that small changes in NZF volume fraction at low levels do not change ϵ_r as drastically as similar changes in BST volume fraction since $\epsilon_{NZF} \ll \epsilon_{BST}$ (e.g., ϵ_{BST} ~ 15,000 and ϵ_{NZF} ~ 5.5 at 100 kHz). At volume fractions over 15%, ϵ_r quickly begins to more closely resemble ϵ_{NZF} and $\epsilon_{NZF} \gg \epsilon_{PDMS}$, so slight changes in the volume loading will have more effect on the composite behavior.

Figure 9b shows that μ_r also increases with NZF volume fraction, although the change is not as dramatic as the permittivity since $\epsilon_{NZF} \gg \mu_{NZF}$, and depends on frequency. Figure 11 shows the one-way ANOVA analysis of the changes in volume loading on μ_r. Small changes in NZF loading (5% to 10%, 10% to 15%, 15% to 20%, and 20% to 25%) do not induce statistically significant changes in μ_r ($p > 0.05$). However, larger changes in NZF volume fraction (e.g. PMDS to 25% and 5% to 25%) do induce statistically significant changes in μ_r ($p < 0.05$). Thus, one may manipulate NZF volume fraction to tune μ_r, but such modification requires a sufficiently large change in volume loading.

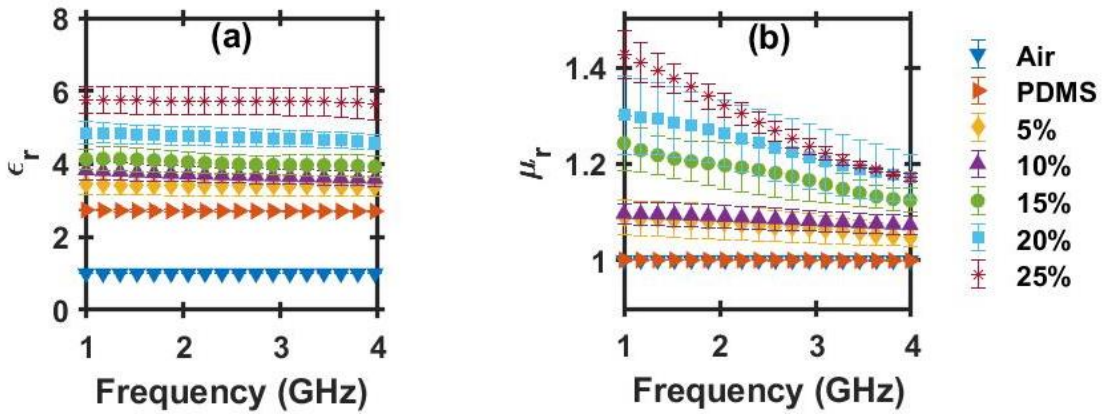

Figure 9. The real (a) permittivity ε_r and (b) permeability μ_r of composites containing various volume loadings of nickel zinc ferrite inclusions in a PDMS (silicone) matrix.

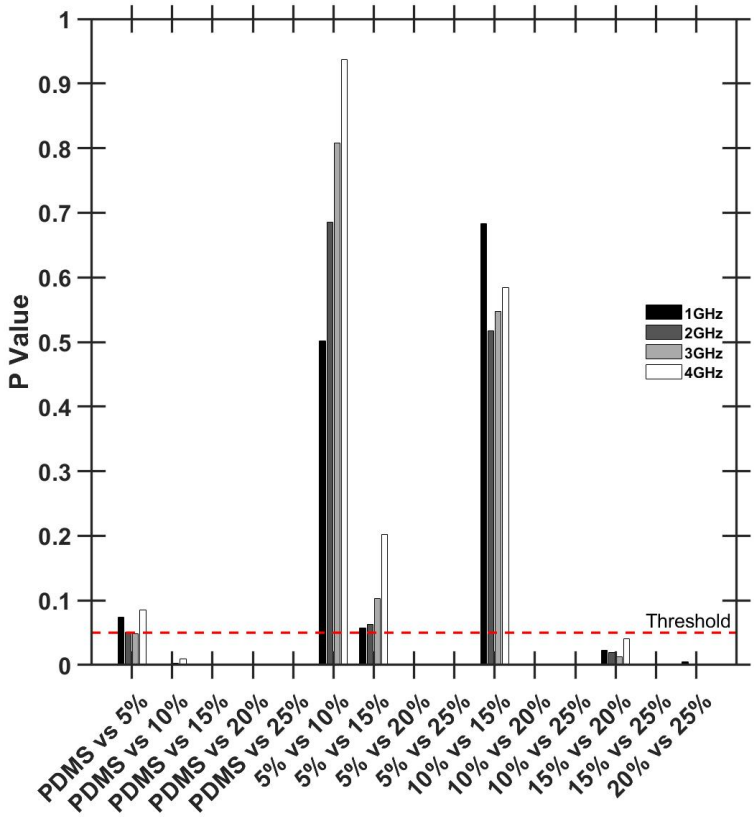

Figure 10. Statistical analysis of the real permittivity for composites with varying volume fractions of nickel zinc ferrite using a one-way ANOVA test and a multiple comparison analysis using the Tukey-Kramer method.

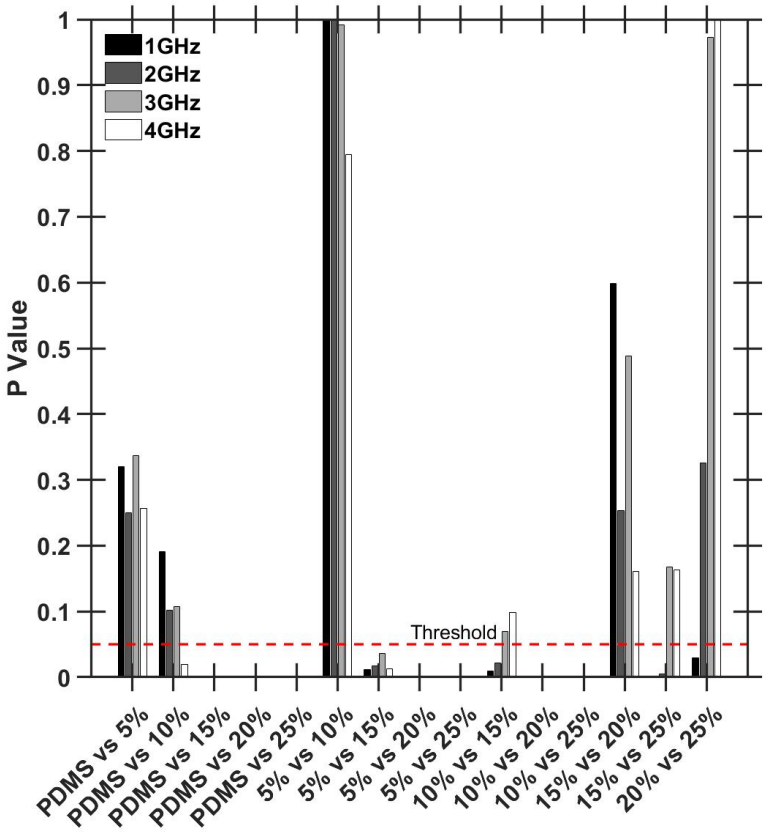

Figure 11. Analysis of statistical significance of the real permeability for composites with varying volume fractions of nickel zinc ferrite using a one-way ANOVA test and a multiple comparison analysis using the Tukey-Kramer method.

Figure 12 shows $\tan\delta$ and $\tan\delta_m$ for composites comprised of various volume loadings of NZF inclusions in PDMS using (1) and (2), respectively. Data are reported as the average of four samples with error bars calculated using (3) and (4) to propagate error for $\tan\delta$ and $\tan\delta_m$, respectively. The dielectric loss tangent for the NZF composites generally increased with frequency, as expected due to the larger inclusion size. For the NZF inclusions $\tan\delta$ was on the same order of magnitude as composites with BST inclusions with the majority of measurements <0.02. However, composites with 10% and 20% NZF had $\tan\delta$>0.02 for frequencies >3 GHz. Also, composites with 25% NZF had $\tan\delta$ much greater than BST composites, reaching an average value of 0.09 at a frequency of 4 GHz. For NZF composites, $\tan\delta_m$ also increased with volume fraction with a highest average value <0.2. Increasing NZF volume loading by 15% induced a statistically significant increase in $\tan\delta_m$ for all frequencies, as shown in Figure 10.

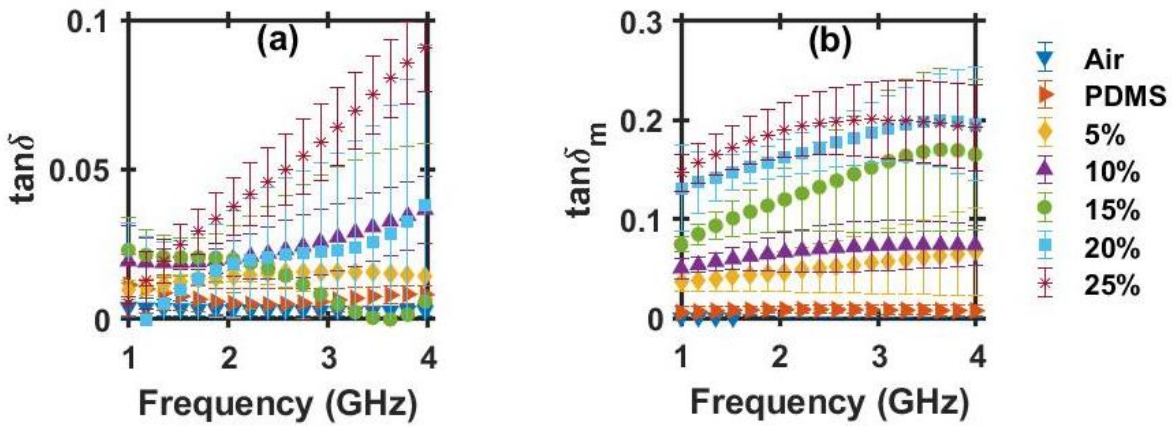

Figure 12. The (a) electrical loss tangent tanδ and (b) magnetic loss tangent tanδ_m for composites with nickel zinc ferrite inclusions in a PDMS (silicone) matrix. The results are reported as the average of four measurements with error bars determined by standard deviation.

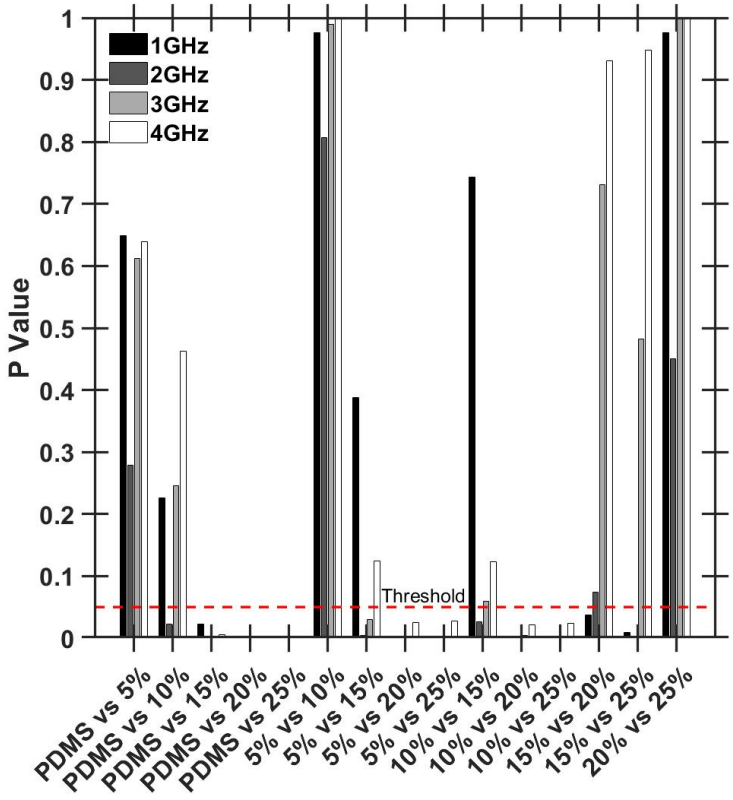

Figure 13. Analysis of statistical significance of tanδ_m for composites with varying volume fractions of nickel zinc ferrite using a one-way ANOVA test and a multiple comparison analysis using the Tukey-Kramer method.

2.4 DC Breakdown Analysis

The average breakdown for the samples containing BST inclusions showed no significant trend, as shown in Figure 14. The breakdown electric field remained relatively constant as volume fraction increased.

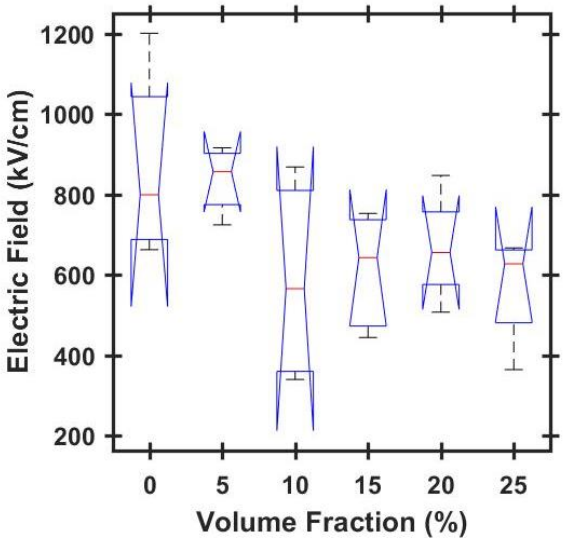

Figure 14. ANOVA test of the breakdown electric field for composites with varying volume fractions of BST showing no statistically significant change in breakdown electric field with increasing BST volume loading.

Figure 15a shows a linear fit to the data using the MATLAB curve fitting tool, indicating that the breakdown electric field for BST composites decreases slightly with increasing volume fraction. However, because the change in breakdown electric field was not statistically significant with changes in volume loading, this best fit line is not meaningful and the change with volume fraction is most likely experimental variation. An ANOVA test showed no statistically significant variation in the breakdown electric field due to changes in BST volume fraction. Thus, for practical purposes, breakdown electric field for BST composites is independent of BST volume fraction.

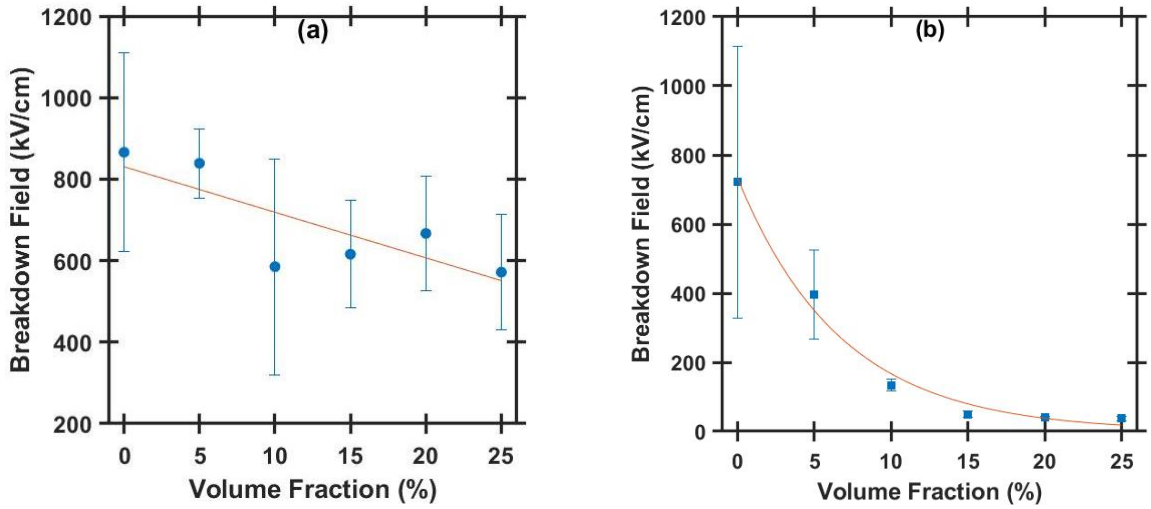

Figure 15. The breakdown electric field for composites with (a) barium strontium titanate (BST) or (b) nickel zinc ferrite inclusions in a silicone (PDMS) matrix. The results are the average of four measurements and the error bars represent the standard deviation of the breakdown electric field values. The fit line has R^2 = 0.65, which is expected since an ANOVA indicates that changes in breakdown electric field with BST volume loading are not statistically significant. The error bars represent the standard deviation of the electric field values with R^2 =0.988.

The breakdown electric field for samples with NZF inclusions decreased exponentially with volume fraction, as indicated by using the MATLAB curve fitting tool to fit the data with R^2 = 0.988, shown in Figure 12b. The error bars shown in Figure 15 are the standard deviation of the breakdown electric fields for each volume fraction.

The Weibull probability plot was used to evaluate the probability of breakdown for the NZF composites as a function of volume fraction. The Weibull distribution is given by

$$f(x|a,b) = \frac{b}{a}\left(\frac{x}{a}\right)^{b-1} e^{-(x/a)^b}, \tag{2-5}$$

where a is the scale parameter and b is the shape parameter.

The slopes of the Weibull distributions show that there is a strong probability that the breakdown will occur in the region predicted by the Weibull plot. The breakdown electric field decreases with increasing NZF volume fraction, as shown by the scale values in Table 6.

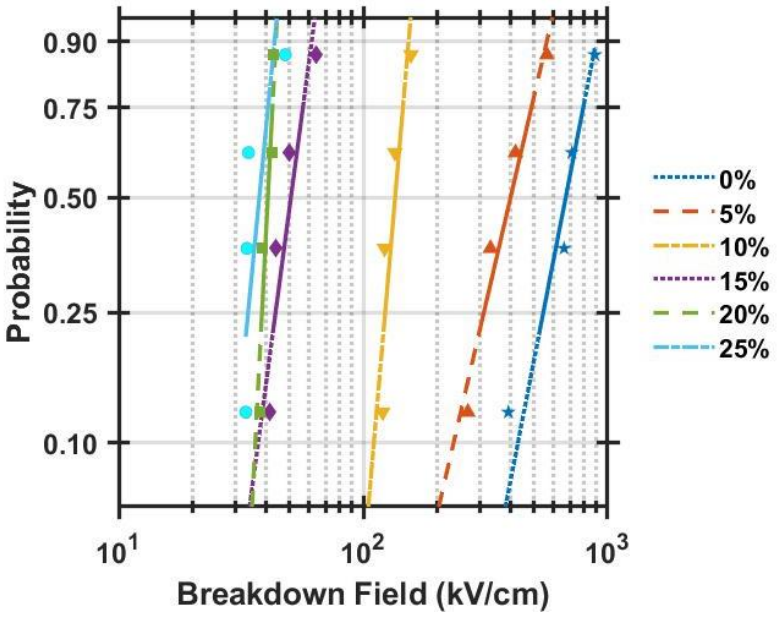

Figure 13: Weibull probability plot for the electric field breakdown of composites with varying volume fractions of nickel zinc ferrite in a silicone (PDMS) host material.

Table 6 summarizes the Weibull parameters calculated using MATLAB to fit the breakdown strength of the NZF composites. The shape of the Weibull distribution for each volume fraction shows that increasing the electric field increases the breakdown probability, as expected.

Table 6. The Weibull parameters for the breakdown fields of composites with varying volume fractions of nickel zinc ferrite in a silicone (PDMS) host.

Volume Fraction (%)	Scale Parameter, *a* (kV/cm)	Shape Parameter, *b*
0	951	4.34
5	438	3.88
10	140	9.28
15	54	5.93
20	41	21.85
25	40	5.80

2.5 Discussion

The change in dielectric properties for composites containing various volume fractions of either BST or NZF inclusions were measured using a coaxial airline from 1-4 GHz. The BST composites exhibited low dielectric and magnetic loss for all volume fractions, while the NZF composites exhibited low dielectric loss for all volume fractions and increasing magnetic loss with increasing volume fraction. An ANOVA test and multiple comparison test showed that the change in the real permittivity of the composite was statistically significant with increasing BST loading, while only larger changes in NZF volume fraction (≥10%) induced statistically significant changes. Adding >10% volume fraction of NZF inclusions increased the permeability of the composites significantly, while adding BST did not induce a statistically significant change in composite permeability.

Changing the volume fraction of BST in BST composites did not statistically change the breakdown strength; for NZF composites, the breakdown electric field decreased exponentially with increasing volume fraction. The Weibull parameters showed a large slope that was independent of volume fraction but further demonstrated the dependence of breakdown strength on volume fraction.

Future work will evaluate the dependence of composite electrical and magnetic properties with various volume fractions of both BST and NZF. Simulations will also be performed evaluating the electrical and magnetic properties of composites using CST Microwave Studio and compared to both experiment and effective medium theories [163]-[165]. Since the long-term goal is to design NLTLs with nonlinear permittivity and/or permeability [133], future will work will also include measuring this nonlinear behavior for composites with BST and/or NZF inclusions.

3. MATERIAL PROPERTIES OF COMPOSITES WITH BARIUM STRONTIUM TITANATE AND NICKEL ZINC FERRITE INCLUSIONS FROM 1 TO 4 GHZ

3.1 Introduction

This chapter was published in Composite Science and Technology, see Ref. [188]. Nonlinear transmission lines (NLTLs) are of great interest as high power microwave (HPM) sources [3],[133]. By providing a solid-state capability for HPM generation, NLTLs eliminate auxiliary systems, such as high power magnets, vacuum systems, and cooling systems for the source and magnets. Eliminating auxiliary systems and particle beam sources significantly reduces HPM system size. The solid-state design of NLTLs allows for a much higher repetition rate than conventional vacuum systems, which are limited because the plasma in the device must recombine prior to subsequent pulses since space charge in the gap reduces the electric field, which reduces the power for subsequent pulses. NLTLs are generally arrayed due to their lower peak power than traditional vacuum system; their operation at lower input voltages may also enable solid state switching, making high repetition rate operation feasible.

Optimizing NLTL system parameters requires fine-tuning the material properties. NLTLs utilize nonlinear materials to generate microwave oscillations in various ways depending on the material used. Ferromagnetic materials, such as nickel zinc ferrite (NZF), are generally used in NLTLs due to their higher frequency generation from hundreds of MHz to low GHz. Ferromagnetic materials have a magnetic permeability that is a function of current and sharpen pulses to the point where an electromagnetic shockwave is generated [3],[33]. Upon generating the shockwave, the magnetic moments will precess around the effective magnetic field [1],[109], which causes the oscillations in the signal at microwave frequencies. When using multiple NLTLs, one can apply an external magnetic field to create a delay in the signal in one of the lines; putting one (or multiple) lines out of phase with the other(s) leads to constructive interference that provides increased power and beam steering [32].

NLTLs can also be comprised of a nonlinear dielectric with voltage dependent permittivity. Voltage dependent permittivity can be implemented using varactors [10],[63],[166], Schottky diodes [2],[167],[168], PIN diodes [3],[169], and ferroelectric materials [34],[78],[86]. Ferroelectric materials, such as barium titanate (BT) [35], [78], , strontium titanate (ST), and

barium strontium titanate (BST), have a permanent dipole due to an asymmetry in the crystalline lattice structure [104]. The lattice structure produces multiple stable positions for the titanium atom while in the ferroelectric phase. At the curie temperature of the material, the structure transitions to a paraelectric phase where the permanent dipole vanishes [78]. Microwave oscillations are produced in a manner similar to ferromagnetic materials, with pulse sharpening and electromagnetic shockwave formation [9]; however, microwave generation for ferroelectric materials occurs because the motion of the titanium atom causes the dipole moment to change in direction and size upon shockwave formation. These oscillations are much slower than those of ferromagnetic materials due to the inertial difference in the generation particle.

Previous work has shown that composite properties can be altered by varying the volume fraction of the inclusion materials [119], [138]-[140], [143]-[147], [149]-[151], [153], [155]-[159], [170]. One application involves designing composites for electromagnetic interference (EMI) shielding by adding a sufficiently high volume loading of conductive inclusions to a plastic can create a conductive material (even approaching stainless steel) at a lower weight than using pure metal. Changing inclusion aspect ratio also changes the volume fraction necessary to achieve a desired composite behavior. For instance, adding 2-3% volume loading of high aspect ratio stainless steel fibers to plastic can make the composite material approach the properties of the metal fibers [93],[94],[134], or achieve percolation [171],[172]. Similarly, a relatively low volume fraction of high aspect ratio fibers of BT can significantly increase the composite permittivity [135],[136]. Adding BT-coated ferrite inclusions can also increase the composite permittivity and, concomitantly, the capacitance for high energy density capacitors [92],[119].

Previous composite studies have measured the dielectric properties of thermoplastics with varying volume fractions of BST [147] and diglycidyl ether of bisphenol A type (DGEBA) with BT inclusions in [140] at frequencies up to 1 GHz. Composites containing ferroelectric and ferromagnetic inclusions, such as cobalt ferrite with BT [143], zinc oxide and BST [170], BST and NZF [146], BT and NZF [142], and carbon black with BT [143], have also been studied to determine the change in electromagnetic properties. However, most measurements for these composites only consider frequencies up to or below 1 GHz [141], [144], [148], [170] or above 8 GHz [143]; the frequencies relevant for most HPM devices (e.g. 2.45 GHz) are less well explored.

In this study, we examine the permittivity and permeability of composites containing both NZF and BST for frequencies from 1 to 4 GHz. We vary the volume fraction of BST and NZF

from 5% to 15% while increasing the total volume fraction of inclusions from 10% to 25% in 5% increments. Section 3.2 describes sample manufacturing and assesses inclusion dispersion. Section 3.3 reports the measured permittivity and permeability of the composites and uses an analysis of variance (ANOVA) test and a multiple comparison test to determine the statistical significance of these properties for changes in inclusion volume loading. We report the DC electric field for composites as a function of inclusion type and volume fraction in Section 3.4. Concluding remarks are provided in Section 3.5.

3.2 Methods

3.2.1 Composite Manufacturing

We manufactured the composites using a silicone elastomer two-part encapsulation medium (Sylgard 184) with BST (TPL Inc. HBS-8000) and/or NZF (Powder Processing & Technology FP350). X-ray diffraction (XRD) showed that BST was $Ba_{0.45}Sr_{0.55}TiO_3$ and NZF was $Ni_{0.5}Zn_{0.5}Fe_2O_4$. The BST powder had an average particle diameter of 600-800 nm. The NZF powder particle size ranged from ~5 μm to ~17 μm. The powders were imaged using a scanning electron microscope (SEM) to verify inclusion size and shape, as shown in Figure 16. We varied the volume fractions of the multiple inclusion composites from 5% to 15% in 5% increments for each inclusion with the total volume fraction of the combined composite ranging from 10% to 25% in 5% increments.

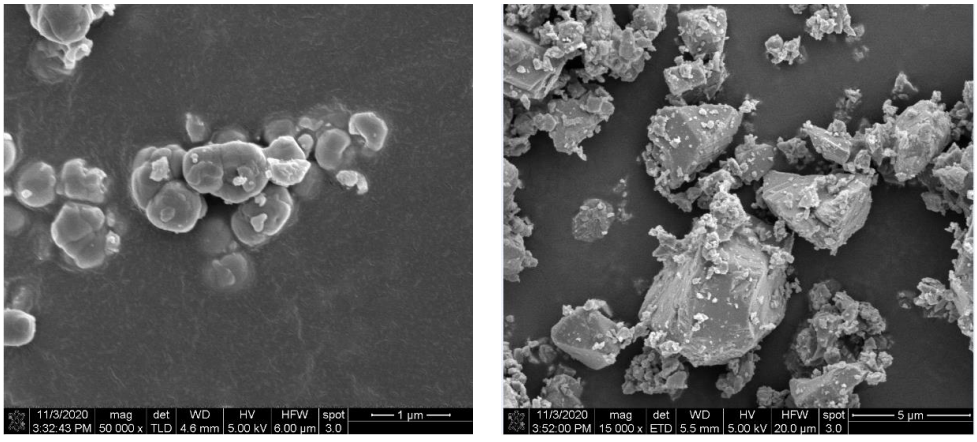

Figure 16. SEM images of (left) BST powder and (right) NZF powder.

The manufacturing process started by measuring the mass of the silicone elastomer base (Part A) and calculating the mass of the desired volume fraction of the inclusion(s). After stirring the mixture by hand for 5 min to combine it, we placed it in a planetary centrifuge (Thinky Mixer AR-100) for 5 min. The mixture was next placed in a bath sonicator (Crest Ultrasonics CP200HT) for 4 h to disperse any conglomerations of the BST powder. Figure 17 shows a representative x-ray microscope image of a 15% BST and 10% NZF sample to demonstrate that the inclusion distribiton was generally uniform with some slight clumping of NZF present. Since the shortest wavelength under consideration is 7.5 cm at 4 GHz, we anticipate that this clumping is generally inconsequential electrically. The sample was then placed in the planetary centrifuge again for 5 min to thoroughly mix the composite, after which we added the cure (10% of the mass of Part A) to the mixture. After mixing the sample by hand for 5 min to start the curing process, we degassed it in a vacuum chamber (Medline Scientific Jeio Tech 665L Vacuum Oven OV-12) at 0.1 MPa below atmospheric pressure for 30 min.

Figure 17. X-ray microscope image of a 15% BST and 10% NZF composite with 4.99 µm resolution.

Before each sample fabrication, we placed the mold in a bath sonicator with a mild detergent at 60°C for 2 h and then dried it with compressed air. After cleaning the mold, we sprayed it with a silicone mold release, which we spread over the surfaces using a paint brush to ensure an even, thin coating. After removing the sample from the mold, the mold was cleaned again using acetone and Kimwipes.

We then used a syringe and tubing to transfer the sample a mold, which we filled from the bottom to minimize air addition to the mixture. Next, the sample and mold were placed in the

vacuum chamber for an additional 5 min to outgas again before the mold, with the composite inside, was placed into the oven (Blue M LO-136E) at 100°C for 2 h.

3.2.2 Permittivity and Permeability Measurements

We measured the composite permittivity and permeability using a network analyzer (Keysight FieldFox Handheld Microwave Analyzer N9913A) connected to a coaxial airline (Keysight Type-N 50 Ω Verification Kit) [64], [65]. The measurements were made with the equipment and cables secured to an anti-static mat while wearing an anti-static wrist strap. We performed a full two port system calibration (Keysight 85054D Economy Mechanical Calibration Kit, DC to 18 GHz, Type-N, 50 Ω) with the airline connected to port 2 to eliminate any loss associated with the airline from 1-4 GHz. A torque wrench was used to tighten all connections to 135 N-cm to ensure secure connections. The airline was cleaned using 70% isopropyl alcohol and Kimwipes (KimTech) to remove any residue on the center connector and interior of the coaxial airline.

The samples were placed on the center conductor of the airline and the length and diameter of the samples were measured using digital calipers. The sample length was made to be at least $\lambda/4$, where λ is the wavelength, based on the lowest frequency measured (1 GHz). After placing the samples in the coaxial airline, we measured the distance from the end of the center conductor to the sample using digital calipers and connected the airline to the system using the aforementioned torque wrench to ensure proper connections.

The permittivity and permeability were calculated using Keysight Material Measurement Suite (Keysight N1500A) Transmission Line and Free Space Module. The settings for the software were set to use the frequency range 1-4 GHz with the power set to -15 dB and the intermediate frequency bandwidth (IFBW) set to 1 kHz. The number of points was set to 601 and the output was averaged over ten scans. We calculated the permittivity and permeability using the Polynomial Fit Reflection/Transmission Mu and Epsilon model, which is an iterative technique used to fit the measured S-parameters [44], due to the presence of magnetic inclusions. All values of permittivity and permeability reports in this manuscript are reported as relative values.

3.2.3 Dielectric Breakdown Measurements

We evaluated the dielectric breakdown strength of four samples of each composite loading using a 200 kV DC Hipot tester (High Voltage Inc. PTS-200) using the setup shown in Figure 18. The samples were placed into a sample holder where the sample was secured between two 3D printed slabs with nylon screws to prevent surface breakdown around the samples. The sample holder was placed into a test fixture with the electrodes aligned in the test fixture using threaded holes. The electrodes were flat in the center to provide a uniform electric field across the sample and had a large radius of curvature to mitigate field enhancement at the edges. The tests were conducted in oil to prevent breakdown around the test fixture. We raised the voltage at a rate of 2 kV/s and monitored it using the voltmeter in the control unit of the Hipot tester. The Hipot tester was placed in guarded current mode to prevent the interlock from tripping due to losses in the cables at high voltages. All breakdown measurements are reported as the average of four measurements.

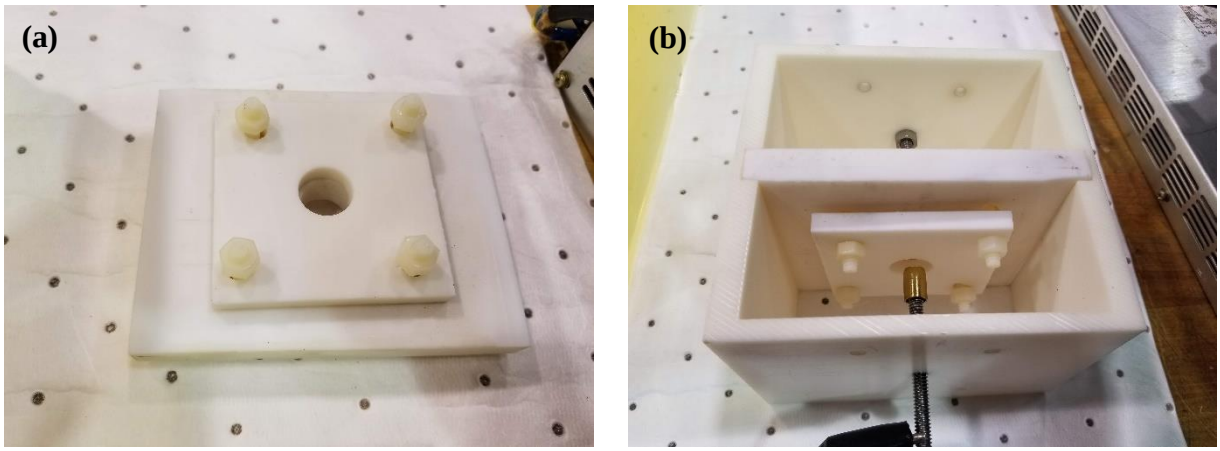

Figure 18. Dielectric breakdown (a) sample holder and (b) test.

3.3 Permittivity and Permeability Measurement Results

The complex permittivity and permeability were measured using the network analyzer and the electrical and magnetic loss tangents were calculated from these values, as described in Section 3.2. Figure 19 shows the measured real permittivity and real permeability of the composites as a function of frequency for various combinations BST and NZF volume fractions. The results are

reported as the mean of four samples for each volume fraction with the error bars determined using standard deviation.

The real permittivity of the composites with BST and NZF, shown in Figure 19a, increases with volume fraction similarly to the composites with only a single inclusion. However, the real permittivity tends to depend more strongly on the total volume fraction compared to the volume fraction of each individual inclusion. The real permeability again increases with volume fraction as shown in the composites with a single inclusion. The main dependence on the real permeability is the volume fraction of NZF, which is expected since this is the only magnetic material in the composite.

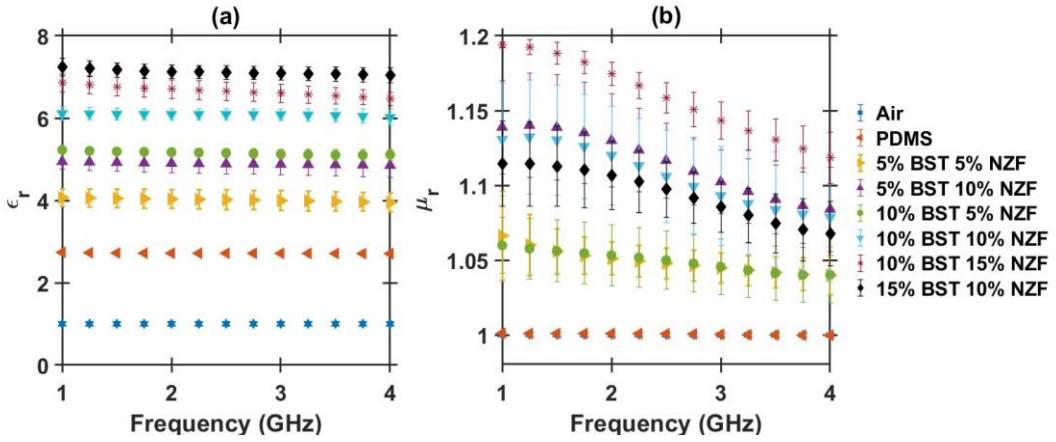

Figure 19. The real (a) permittivity and (b) permeability of composites containing various volume fractions of BST and NZF inclusions in a PDMS matrix. The results reported are the mean of four independent samples with error bars determined by standard deviation.

The dielectric and magnetic loss tangents are calculated by taking the ratio of the imaginary permittivity/permeability to the real permittivity/permeability. The dielectric loss tangent and the magnetic loss tangent are shown in Figure 20. Using error propagation, the standard deviation for the dielectric loss tangent $\tan\delta$ is given by [161],[162]

$$\sigma_{\tan\delta} = \sqrt{\left(\frac{1}{\epsilon_r}\right)^2 \sigma_{\epsilon_i}^2 + \left(\frac{\epsilon_r}{\epsilon_i^2}\right)^2 \sigma_{\epsilon_r}^2}, \tag{3-1}$$

where $\sigma_{\tan\delta}$ is the standard deviation of the loss tangent, ϵ_r is the real permittivity, σ_{ϵ_i} is the standard deviation of the measured the imaginary permittivity, ϵ_i is the imaginary permittivity, and σ_{ϵ_r} is the standard deviation of the measured real permittivity. The standard deviation of the magnetic loss tangent $\tan\delta_m$ is calculated in a similar manner by replacing the real and imaginary permittivity with the real and imaginary permeability, respectively, and the standard deviations of the real and imaginary permittivity with the standard deviations of the real and imaginary permeability, respectively.

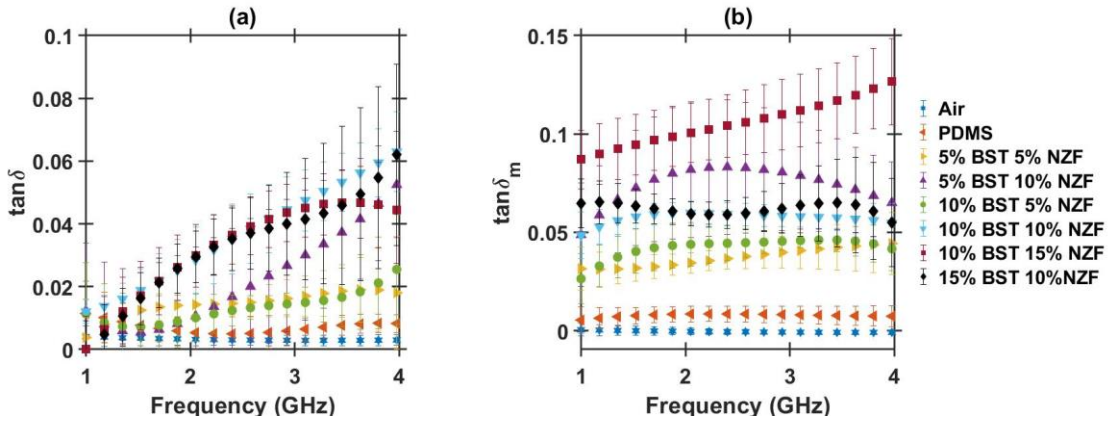

Figure 20. The (a) dielectric (tanδ) and (b) magnetic (tanδ_m) loss tangents for composites comprised of BST and NZF in a PDMS matrix. The results reported are the mean of four independent samples with error bars determined by standard deviation.

The dielectric loss tangent shows that these materials can be considered low loss materials with $\tan\delta < 0.015$, except for the 10% volume fraction of NZF. The magnetic loss tangent also shows that air and PDMS are low magnetic loss materials with $\tan\delta_m < 0.015$. The magnetic loss tangent increases with increasing NZF such that $\tan\delta_m < 0.15$.

3.3.1 Statistical Analysis

A one-way analysis of variance (ANOVA) was performed on the measured real permittivity. A multiple comparison test utilizing the Tukey-Kramer method, which is optimized for balanced one-way ANOVA tests with equal sample sizes, was applied to the output of the ANOVA test to determine the statistical significance in the change of the dielectric values due to

the change in the volume fraction. We used $p < 0.05$ to indicate a statistically significant difference between two measurements. The ANOVA and multiple comparison tests were performed at each frequency to determine whether a change in volume fraction of one of the inclusion materials induced a statistically significant change in permittivity. All changes in volume fractions caused statistically significant changes in real permittivity except for 5% BST with 10% NZF compared to 10% BST with 5% NZF. The overall volume fraction of the inclusions has a larger dependence on the permittivity of the inclusions, although the change in individual inclusion volume fraction also changes the composite permittivity in a statistically significant way. Due to the high contrast in permittivity between BST and NZF, the dependence on single inclusion volume fraction is appropriate.

We performed the same statistical analysis on the measured real permeability for composites containing BST and NZF inclusions at each frequency, selecting $p = 0.05$ as the threshold indicating statistical significance. Figure 21 shows p as a function of frequency for different volume loadings. As anticipated, the prominent factor driving changes in permeability is the volume loading of NZF, which is the only magnetic material involved. Because the magnitude of NZF permeability is lower than the magnitude of either BST or NZF permittivity, changes in NZF volume loading cause a lower magnitude change in permeability than changes in permittivity given the same volume change of BST or NZF.

Generally, a change in NZF volume fraction of $\leq 5\%$ does not result in a statistically significant change in real permeability. A variation in NZF volume fraction of $\geq 10\%$ results in a statistically significant change in the composite permeability from 1 to 3 GHz. While adding BST should not change the permeability of the composite, the permeability does seem to vary slightly with BST volume loading. This could be a result of the much smaller size of the BST particle allowing it to electrically separate the NZF particles from one another, decreasing the overall magnetic contribution. This also occurs for the magnetic loss tangent, shown in Figure 20b, where the magnetic loss tangent decreases with increasing BST volume fraction [174].

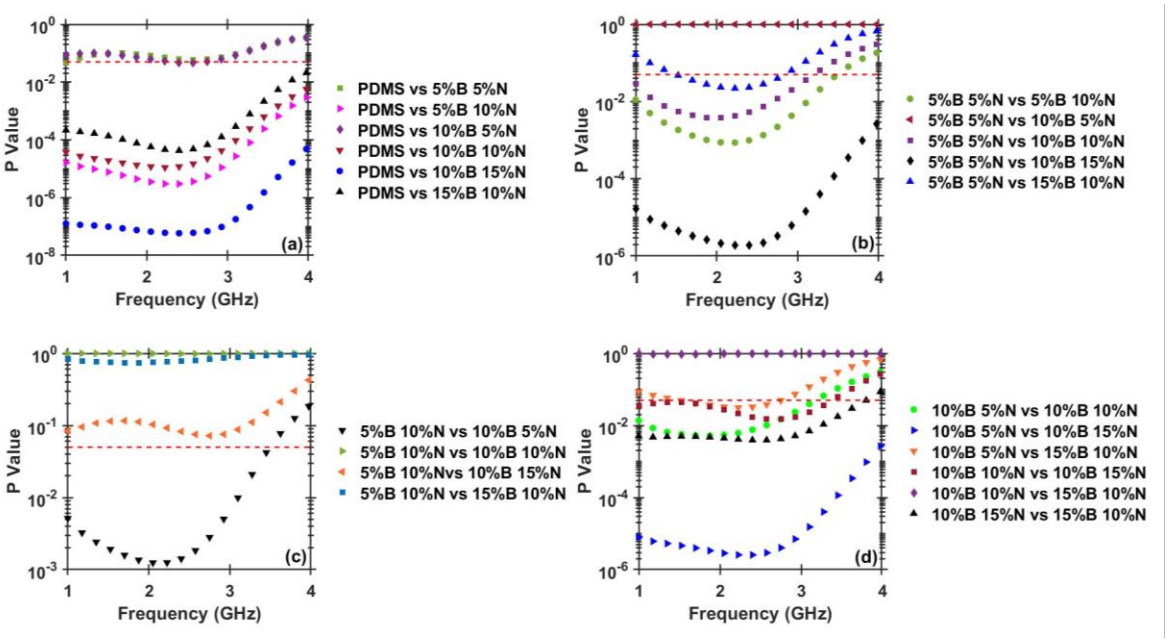

Figure 21. Statistical analysis of the real permeability for composites with varying volume fractions of BST (B) and NZF (N) using a one-way ANOVA test and a multiple comparison analysis using the Tukey-Kramer method. The comparisons for (a) PDMS vs composites wi th BST and NZF, (b) 5% BST and 5% NZF vs composites with BST and NZF, (c) 5% BST and 10% NZF vs composites with BST and NZF, and (d) 10% BST with 5%, 10%, or 15% NZF vs composites with BST and NZF. The dotted lines denote $p = 0.05$ with lower p indicating statistical significance. The results reported are the mean of four independent samples with error bars determined by standard deviation.

The same statistical analysis was also performed on the dielectric and magnetic loss tangents. Figure 22 shows the statistical analysis for the dielectric loss tangent. There are no statistically significant changes in the dielectric loss tangent at frequencies below 2 GHz. The change in dielectric loss tangent becomes statistically significant for total volume fraction ≥ 20% when compared to PDMS for all frequencies studied. Only a few of the 5% or 10% changes in either BST or NZF volume fraction led to statistically significant changes in dielectric loss tangent, indicating that dielectric loss tangent is relatively insensitive to volume fraction of either BST or NZF, particularly below 2 GHz.

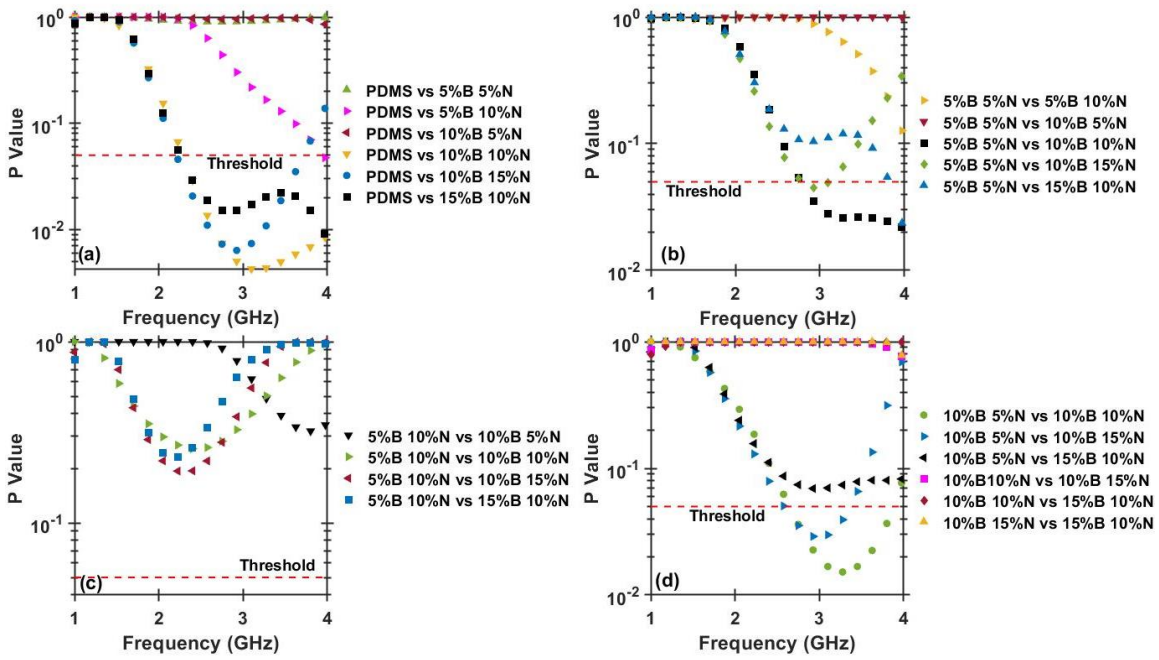

Figure 22. Statistical analysis of the dielectric loss tangent for composites with varying volume fractions of BST (B) and NZF (N) using a one-way ANOVA test and a multiple comparison analysis using the Tukey-Kramer method. The comparisons for (a) PDMS vs composites with BST and NZF, (b) 5% BST and 5% NZF vs composites with BST and NZF, (c) 5% BST and 10% NZF vs composites with BST and NZF, and (d) 10% BST with 5%, 10%, or 15% NZF vs composites with BST and NZF. The dotted lines denote $p = 0.05$ with lower p indicating statistical significance. The results reported are the mean of four independent samples with error bars determined by standard deviation.

Figure 23 shows the statistical analysis for the magnetic loss tangent. The magnetic loss tangent is statistically significant once the NZF volume fraction is ≥ 10% when compared to PDMS. When the volume fraction of BST is ≥ 10%, changes from 5% to 15% NZF and 10% to 15% NZF produce statistically significant changes in magnetic loss tangent.

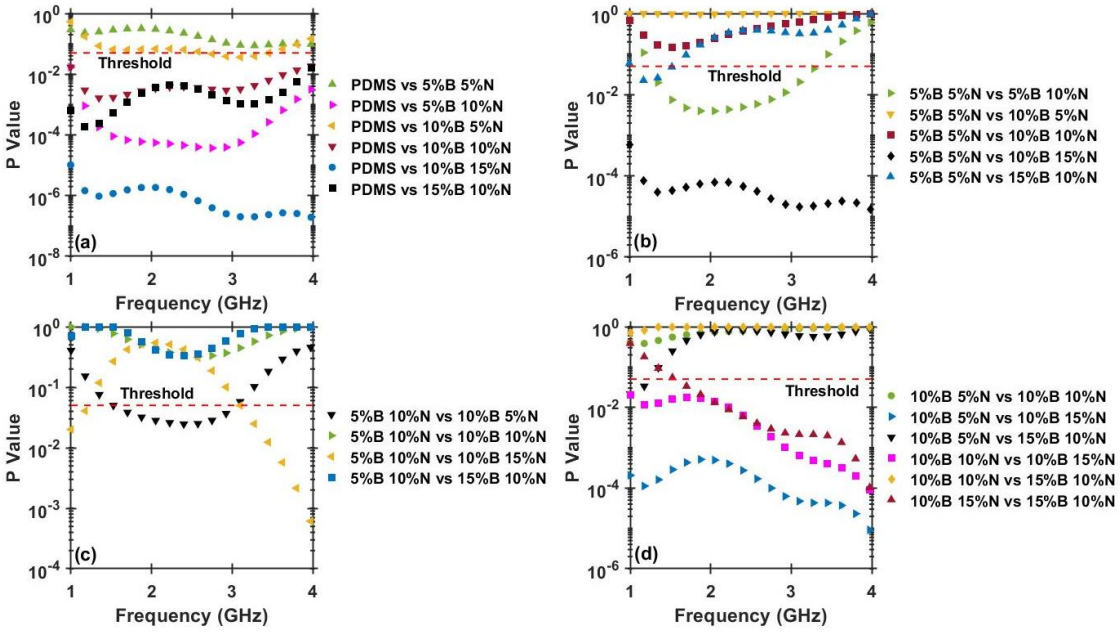

Figure 23. Statistical analysis of the magnetic loss tangent for composites with varying volume fractions of BST (B) and NZF (N) using a one-way ANOVA test and a multiple comparison analysis using the Tukey-Kramer method. The comparisons for (a) PDMS vs composites with BST and NZF, (b) 5% BST and 5% NZF vs composites with BST and NZF, (c) 5% BST and 10% NZF vs composites with BST and NZF, and (d) 10% BST with 5%, 10%, or 15% NZF vs composites with BST and NZF. The dotted lines denote $p = 0.05$ with lower p indicating statistical significance. The results reported are the mean of four independent samples with error bars determined by standard deviation.

3.4 DC Breakdown Analysis

Previous studies showed that adding BST [175],[176] or BT [177] inclusions to composites increases the dielectric breakdown strength. We previously showed that the breakdown voltage of composites containing only NZF inclusions decreased exponentially with increasing volume fraction [179]. Table 7 shows the dielectric strength for composites containing various volume loadings of BST and/or NZF. The volume fractions 15% NZF 5% BST and 15% BST 5% NZF were not tested. Adding BST to NZF composites dramatically increased the breakdown strength. Adding higher volume fractions of NZF to BST composites reduced the breakdown strength, although not to the extent that such changes did in PDMS without BST.

Table 7. DC dielectric breakdown threshold in kV/cm for composites with various volume loadings of BST and NZF in a PDMS matrix. Values are reported in units of kV/cm as the average of four measurements with error determined by standard deviation. Samples labeled N/A were not tested.

		NZF Volume Fraction (%)			
BST Volume Fraction (%)		0	5	10	15
	0	710.42±279.07 kV/cm	395.68±111.041	133.51±14.58	49.90±8.64
	5	838.86±73.72	567.59±247.00	392.24±155.37	**N/A**
	10	585.15±229.28	597.53±68.15	428.50±13.58	401.20±150.73
	15	644.29±111.25	**N/A**	423.75±103.53	**N/A**

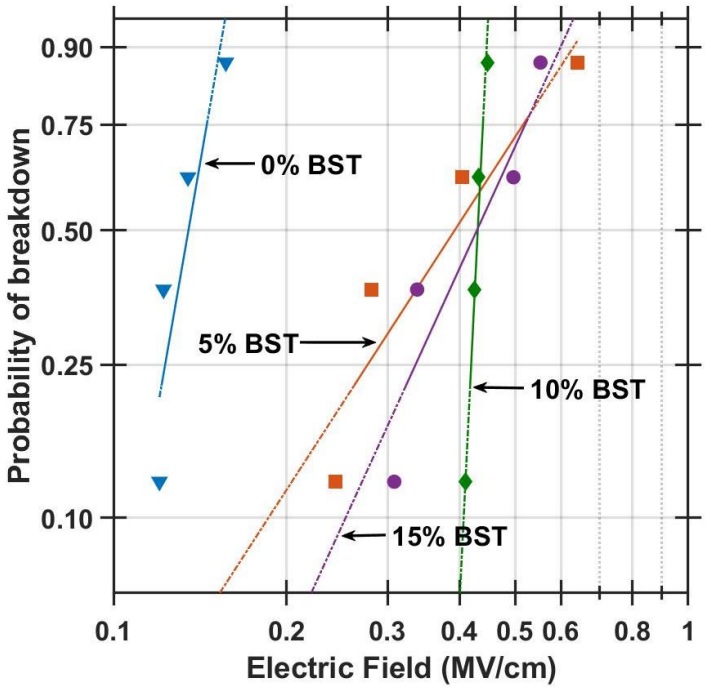

Figure 24. Weibull probability plot of composites with 10% volume fraction of NZF inclusions with increasing volume fraction of BST in a PDMS host matrix.

Figure 24 shows the breakdown probability for composites with 10% NZF and increasing the volume fraction of BST from 0% to 15%. The electric field strength of the composites increases dramatically with increasing volume fraction of BST. Adding 10% BST to NZF increases the average breakdown electric field from 133.5 ± 14.5 kV/cm to 428.5 ± 13.5 kV/cm by adding 10% BST to the composite.

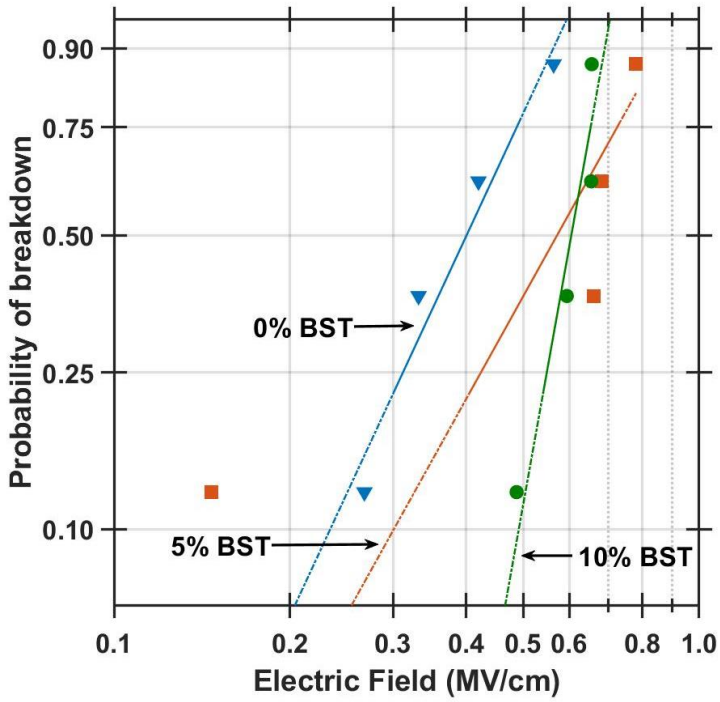

Figure 25. Weibull probability plot of composites with 5% volume fraction of NZF inclusions with increasing volume fraction of BST in a PDMS host matrix.

Figure 25 shows the Weibull probability plot for composites containing 5% NZF and volume fractions of BST from 0 to 10%. As for the 10% NZF case reported in Figure 8, the electric breakdown strength increases markedly with increasing BST volume fraction, increasing from 395.7 ± 111 kV/cm to 597.5 ± 68.15 kV/cm by adding 10% BST.

Conversely, fixing BST volume fraction and increasing NZF volume fraction reduces the electric breakdown strength, as shown in Figures 26 and 27. For a composite containing 5% BST, Figure 10 shows that increasing the volume fraction of NZF from 0% to 10% decreases the breakdown strength. The average breakdown strength for composites with 5% BST decreases from 838.86 ± 73.7 kV/cm with 0% NZF to 392.24 ± 155.37 kV/cm with 10% NZF. A similar relationship arises for samples with 10% BST when varying the volume fraction of NZF from 0% to 15% NZF, as shown in Figure 11. The average electric field for composites with 10% BST and 0% NZF decreases from 585.15 ± 229.28 kV/cm to 401.2 ± 150.73 kV/cm for samples with 10% BST and 15% NZF.

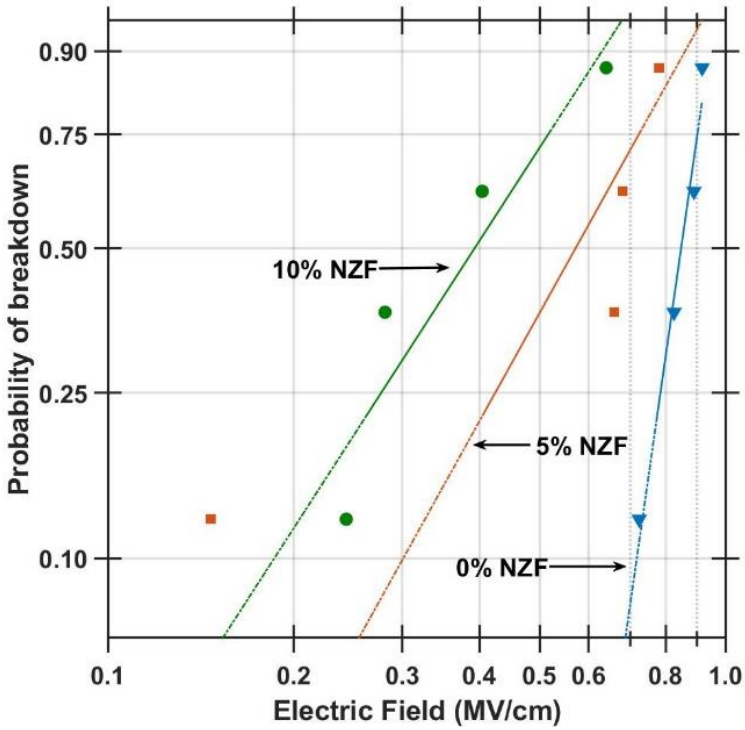

Figure 26. Weibull probability plot of composites with 5% volume fraction of BST inclusions with increasing volume fraction of NZF in a PDMS host matrix.

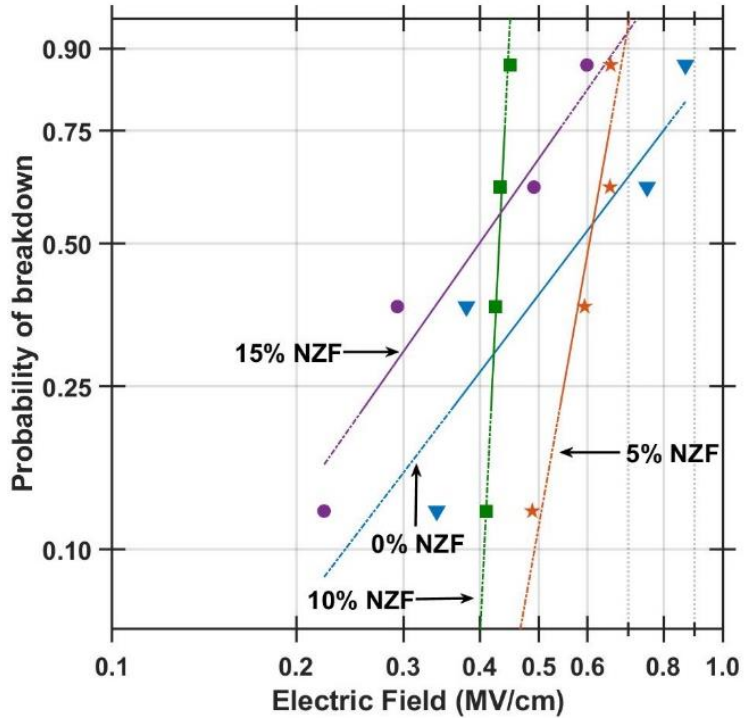

Figure 27. Weibull probability plot of composites with 10% volume fraction of BST inclusions with increasing volume fraction of nickel zinc ferrite in a PDMS host matrix.

3.5 Discussion

We report permittivity and permeability of composites containing various volume fractions of both BST and NZF from 1-4 GHz using a coaxial airline. The composites exhibited low dielectric (< 0.09) and magnetic (< 0.15) loss for all volume loadings and frequencies considered. Using an ANOVA test and multiple comparison test, we observed that small changes in volume fraction (5%) of either BST and NZF induced statistically significant changes in real permittivity; however, the change in real permeability was not statistically significant for any change in BST and was only statistically significant for larger changes in NZF volume fraction (≥ 10%).

The DC electrical breakdown threshold showed a strong correlation to the volume fraction of NZF inclusions in the composites. For a fixed volume fraction of either 5% or 10% NZF, the breakdown threshold increased dramatically by adding as little as 5% volume fraction of BST. For a fixed volume fraction of either 5% or 10% BST, the breakdown threshold decreased significantly with increasing volume fraction of NZF.

The results indicate that adding small amounts of a highly insulating dielectric, such as BST, can greatly increase the power handling capabilities of composites with NZF. The increased power handling may make the design of NLTLs capable of hundreds of MW peak power plausible. Future work will focus on manufacturing NLTLs using composites comprised of BST and/or NZF and evaluating the frequency output, power output, and repetition rates (up to 25 kHz).

4. SIMULATED AND MEASURED OUTPUT FROM A COMPOSITE NONLINEAR TRANSMISSION LINE DRIVEN BY A BLUMLEIN PULSE GENERATOR

4.1 Introduction

Nonlinear transmission lines (NLTLs) provide a solid state high power microwave (HPM) option with multiple benefits over their traditional vacuum alternatives [133]. NLTLs use voltage-dependent permittivity and/or current-dependent permeability to generate RF rather than requiring external high power magnets, cryogenic systems, or vacuum system to generate RF. Although NLTL systems generally produce lower output power (hundreds of MW) than vacuum systems (GW), researchers have combined multiple NLTLs using constructive interference to generate high powers [112], [118]. Due to their solid state nature, NLTLs can operate at much higher pulse repetition rates than traditional vacuum systems, which must eliminate residual space charge prior to the application of subsequent pulses [109].

NLTLs are constructed in three main topologies: lumped element (LE), split ring resonator (SRR), and nonlinear bulk material. SRRs are very small and useful for low power applications; however, they are not suited for HPM applications [133]. While LE NLTLs provide great modularity and more compact size, they provide far less power handling capability than nonlinear bulk material lines. LE NLTLs can be manufactured with nonlinear capacitance and/or nonlinear inductance with hybrid NLTLs utilizing both nonlinear capacitance and inductance [128]. Typically, NLTLs comprised of nonlinear bulk material use a ferrite material, such as nickel zinc ferrite (NZF), and are referred to as gyromagnetic lines [11], [78], [110], [112], [123]. Gyromagnetic lines incorporate a section of ferrous material around the center conductor of the NLTL with an additional insulating layer, either SF6 or transformer oil, to prevent breakdown between the inner and outer conductor [109], [123]. The RF is produced when the input pulse is sufficiently sharpened to generate an electromagnetic shockwave. Some researchers apply an external magnetic field to decrease the length required to generate this shockwave and to align the magnetic moments to allow for synchronous precession. After producing the shockwave, the magnetic moments will precess around the effective magnetic field generated by the current applied to the line and the external bias, in accordance with the Landau-Lifshitz-Gilbert (LLG) equation [189].

Bulk material lines leveraging nonlinear permittivity use ferroelectric materials in the form of barium titanate (BT) or barium strontium titanate (BST) [33]. These materials have an offset atom inside the crystalline structure that creates a permanent polarization vector. When the material temperature is close to the Curie temperature, this atom can move to multiple stable positions inside the crystalline structure with small amounts of additional energy [78]. Applying a pulse stresses the atom, moving it to other stable positions in the crystalline lattice after electromagnetic shockwave formation. The movement of this polarization vector produces the RF signal. However, due to the difference in inertia between the electron in the gyromagnetic line and the atom in the ferroelectric material, the gyromagnetic line generates much higher frequencies, on the order of GHz, compared to tens of MHz for the ferroelectric line [178].

Hybrid NLTLs can generate higher frequencies than purely nonlinear capacitive lines [22]. This benefit also provides output frequency tunability based on the input pulse amplitude. Previous work designed composites with ferroelectric and/or ferrimagnetic material and measured the material properties as a function of volume fraction [179], [188]. These studies showed that adding small amounts of BST to an NZF-filled composite dramatically increased the breakdown strength, enabling the application of higher voltage pulses and the potential for high power output. The composites were manufactured with various volume fractions of BST and/or NZF to determine the permittivity and permeability dependence of the composites on the inclusion volume fractions from 1 to 4 GHz [179], [188]. The magnetic field dependence of the composite permeability was also measured from 1 to 4 GHz [174]. Combining BST with NZF increased the high voltage capability compared to material containing just NZF inclusions, while providing flexible tuning of both nonlinear permittivity and permeability.

Now that we have characterized the permittivity, permeability, and breakdown strength of composites consisting of NZF and/or BST composites, the next step is to test the ability to generate RF. While most NLTLs are tested using pulse forming networks (PFNs) with a 50 Ω load, we instead use a Blumlein generator with a 10 Ω load. As mentioned above, constructing NLTLs using composites gives additional flexibility in tuning the dielectric and magnetic properties of the NLTL, providing the ability to tune to different pulse generator outputs aside from the more standard 50 Ω load, such as linear transformer drivers [194] and Blumlein generators [180]. We initially hypothesized that the microwave generation from the NLTL should be independent of the method of pulse formation and only dependent on the critical pulse parameters, specifically voltage, rise-

time, and pulse duration. Instead, the experiments and simulations reported here demonstrate that using a Blumlein generator rather than a PFN actually dampens the RF generation because the waves traveling in opposite directions to form the pulse in the Blumlein topology actually mitigate the shockwave phenomenon in the NLTL.

This paper outlines the manufacturing and testing of NLTLs constructed from composites comprised of BST and NZF in a silicone matrix spanning the entire gap between the inner and outer conductor of the coaxial geometry. We then tested them using a Blumlein pulse generator with a pulse duration of 10 ns and rise- and fall-times of 1.5 ns [180] to test the NLTLs. We also used LT Spice to simulate the driving of the NLTLs using either a Blumlein or PFN modulator. Section 4.2 describes the manufacturing process, test setup, and modeling setup. Section 4.3 reports the experimental and simulation results. Final conclusions are presented in Section 4.4.

4.2 Methods

4.2.1 NLTL Manufacturing

We manufactured a coaxial NLTL using a 1 in copper tube with an internal diameter of 0.75 in as the outer conductor and a 0.5 in copper rod as the center conductor to match the 10 Ω impedance of the Blumlein pulse generator [180]. The composites were made by weighing the base material (Part A PDMS Sylgard 184) and adding the required amounts of NZF (FP350 PPT Technologies) and BST (HBS-8000 TPL Inc.) to achieve the following desired volume loadings: 25% NZF, 15% NZF/10% BST, and 10% NZF/15% BST. The mixtures were then stirred by hand for 5 min to incorporate the powders into the PDMS base and placed in a planetary centrifuge (Thinky AR100) for 5 min at 400 rpm for thorough mixing. Composites containing BST were then placed in an ultrasonic bath for 4 h to break up any conglomerations of powder. We added a curing agent at a ratio of 1:10 mass of the PDMS base, and mixed by hand for 5 min. The mixtures were then placed in a vacuum chamber at < 20 kPa for 30 min to remove any air bubbles. We next poured the samples slowly into the outer conductor at an angle to minimize air addition into the mixture. The outer conductor with the composite was then placed into the vacuum chamber for 5 min at < 20 kPa to remove any air introduced. We next slowly inserted the center conductor into the line and centered it using an aluminum block on the bottom of the line. Again, the mixture with the center conductor inserted was placed in the vacuum chamber for 5 min at < 20 kPa to remove

any gas introduced. Finally, another aluminum block was placed on top of the line to ensure the center conductor was centered and the line was place in an oven (Thermo Scientific Heratherm OGS180) at 100 ℃ for 2 h to cure. Figure 28 shows a representative constructed NLTL after winding 14 AWG magnetic wire around the line for bias

Figure 28. Final NLTL after winding 14 AWG magnet wire around line for bias. The three brass connectors are D-dot probes to assess the wave propagation through the line.

4.2.2 NLTL Testing

We used a Blumlein pulse generator (INP, Greifswald, Germany) to apply a 10 ns pulse with a 1.5 ns rise and fall time to the NLTL [180]. The Blumlein generator used a pressurized spark gap switch filled with dry nitrogen gas to increase the breakdown threshold and control the output voltage of the generator by altering the pressure. A Glassman high voltage supply (model EJ40P15) provided the high voltage to the generator with a 5 MΩ resistor in series between the generator and power supply to limit the current output of the supply. We matched the impedance of the NLTL to the 10 Ω impedance of the generator.

Voltage measurements were made at the outputs of the Blumlein and the NLTL by using 10 ft RG 58 cables connected to a 2.5 GHz oscilloscope (Lecroy WaveRunner 625 Zi). We selected the cable length to ensure that any reflections from the measurements did not interfere with the original pulse. A custom resistive voltage divider was used to measure the voltage signals and was comprised of a noninductive resistor (HVR RT series) and 30 dB attenuator (Pasternack PE7049-30). detailed in Appendix A.

4.2.3 Modeling

We used LT Spice, a lumped circuit simulation software, to model the NLTLs. The current dependent inductance was modeled by defining the flux through the inductor. Motivated by Ref.

[101], we modeled the magnetic field dependence of the permeability of the NZF in the composites by

$$\mu(I) = (\mu_i - \mu_S) \times \tanh\left(\frac{H}{H_s}\right)^2 + \mu_{fit}, \tag{4-1}$$

where μ_i is the initial permeability of the composite, μ_s is the saturation permeability (we set μ_s = 1), H is the applied magnetic field, H_s is the magnetic field at which the ferrite saturates (H_s = 159.15 kA/m), and μ_{fit} is a fitting value with a typical value $\mu_{fit} \approx \mu_s \approx 1$. We used the curve fitting tool in MATLAB to fit experimental measurements of $\mu(I)$ for composites with the same volume loading as the manufactured NLTLs [174]. Figure 29 shows a representative fit at 1 GHz with Table 8 showing curve fitting parameters for each composite.

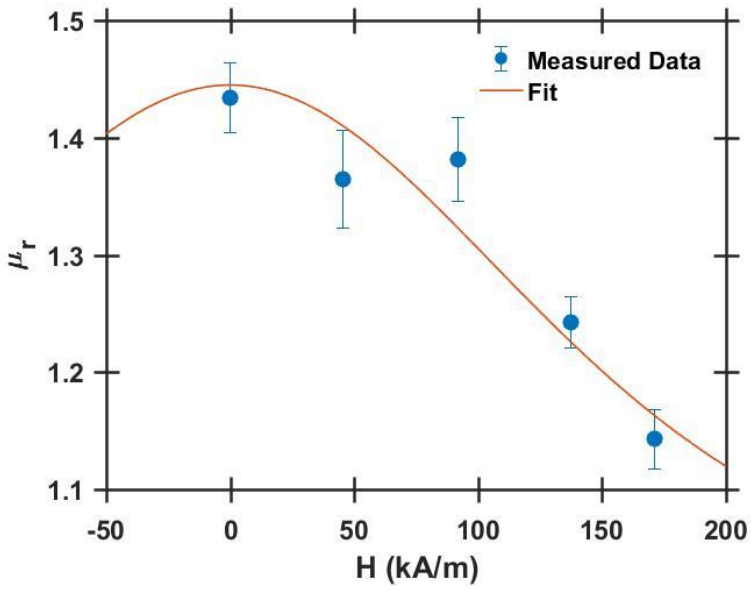

Figure 29. Curve fitting performed in MATLAB for the 25% NZF inclusions based on field dependent measurements of the permeability. The measurement was performed at 1 GHz and the fit produced an R^2 value of 0.8856 [174].

Table 8. Magnetic field dependent permeability curve fitting results for composites used in NLTL measured at 1 GHz [174].

Volume Fraction	μ_i	μ_{fit}	R^2
25% NZF	1.45	0.9949	0.9129
10% BST 15% NZF	1.25	0.9465	0.968
15% BST 10% NZF	1.16	0.953	0.8856

The voltage dependent capacitance for the composite is calculated using the charge in the capacitor, given by [181]

$$Q(V) = (C_0 - C_{SAT})V_{SAT}\tanh\left(\frac{V}{V_{SAT}}\right) + C_{SAT}V, \quad (4\text{-}2)$$

where C_0 is the initial capacitance, C_{SAT} is the saturated capacitance, V_{SAT} is the voltage at which saturation begins (230 V), and V is the applied voltage. Table 9 provides the values for each composite.

We model an NLTL driven by a 10 ns pulse delivered by either a Blumlein modulator, shown in Figure 30, or a traditional 10 ns pulse forming network (PFN), shown in Figure 31; both modulators had rise- and fall-time of 1.5 ns. The capacitance and inductance are calculated based on the dimensions of the NLTL for a coaxial capacitor and the inductance of a coaxial line, respectively, using the material properties for the composites measured previously [179], [188]. We model the 20 in NLTLs that we manufactured as twenty LC segments, where the capacitance C and inductance L are given by

$$C = \frac{2\pi\epsilon_0\epsilon_r}{Ln\left(\frac{b}{a}\right)} \quad (4\text{-}3)$$

and the inductance, L, was calculated by

$$L = \frac{\mu_0\mu_r}{2\pi}Ln\left(\frac{b}{a}\right) \quad (4\text{-}4)$$

Where ϵ_0 is the permittivity of free space, ϵ_r is the permittivity of the composite, b is the inner diameter of the outer conductor (0.75 in,), a is the diameter of the center rod (0.5 in.), μ_0 is the permeability of free space, and μ_r is the permeability of the composite.

Table 9. Initial and saturated capacitance and inductance values per inch for the constructed composite NLTLs.

Volume Fraction	C_0 (pF/m)	C_{SAT} (pF/m)	L_0 (nH/m)	L_{SAT} (nH/m)
25% NZF	20.9	20.9	2.99	2.06
10% BST 15% NZF	23.9	14.4	2.46	2.06
15% BST 10% NZF	25.2	13.3	2.30	2.06

We determined C_{SAT} for the 25% NZF, 10% BST/15% NZF, and 15% BST/10% NZF composites using (3) with the permittivity of the composites corresponding to NZF volume fractions based on prior measurements composites based on prior measurements [14], [15] from Chapter 2.

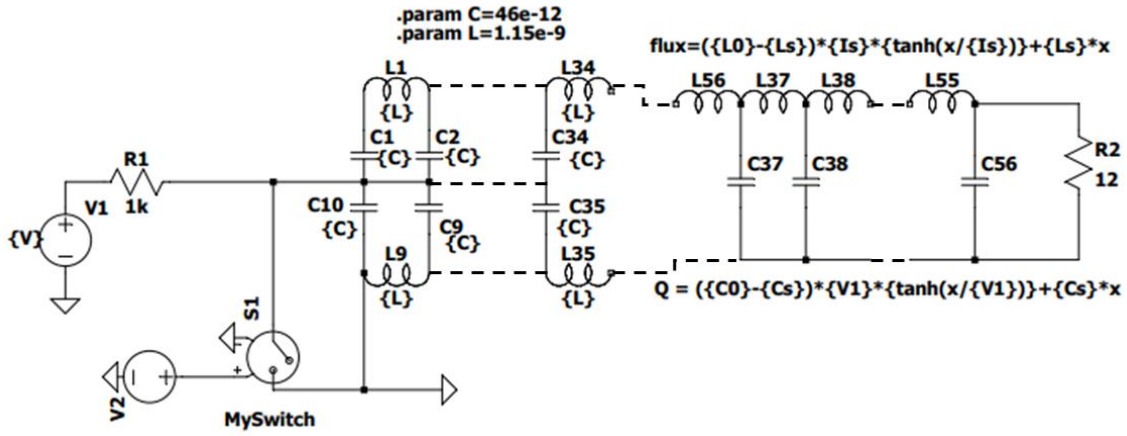

Figure 30. Circuit schematic of 10 ns Blumlein driving NLTL made of composite with nonlinear inclusions in a silicone matrix, where Ls is the saturated inductance, L0 is the initial inductance, Is is the current at which the saturation takes place, C0 is the initial capacitance, Cs is the saturated capacitance, and V1 is the voltage when saturation occurs.

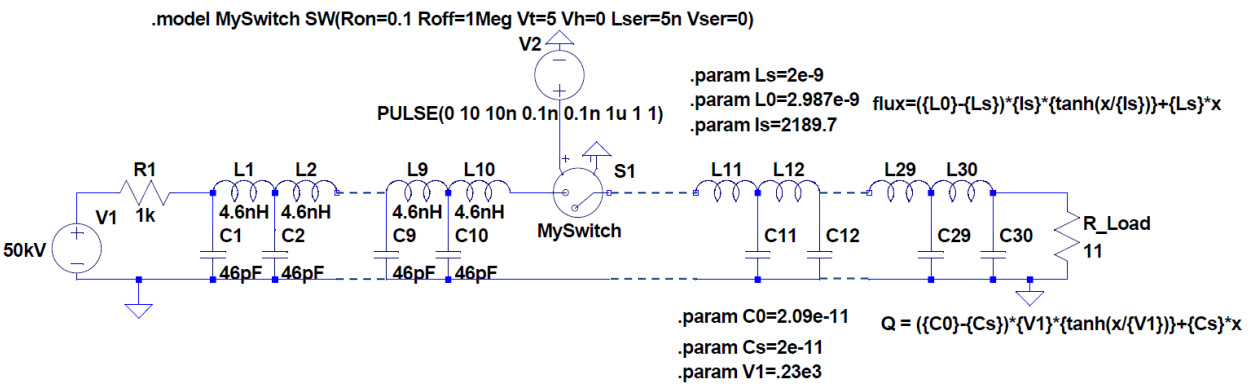

Figure 31. Circuit schematic with 10 ns PFN driving NLTL made of 25% NZF composite in a silicone matrix. Ls is the saturated inductance, L0 is the initial inductance, Is is the current at which the saturation takes place, C0 is the initial capacitance, Cs is the saturated capacitance, and V1 is the voltage when saturation occurs.

4.3 Results

4.3.1 Modeling an NLTL driven by Blumlein modulator

We performed LT Spice simulations using a charging voltage of 10 to 60 kV in 10 kV increments. Representative input and output waveforms for a 25% NZF NLTL are shown in Figure 32. The voltage differences of the Blumlein output and across the load were recorded to distinguish oscillations produced by the Blumlein from those of the NLTL. The output voltage of the NLTL was then compared between the different charging levels and normalized to the peak Blumlein output voltage to determine if oscillation production increased or remained the same.

Figure 32 shows the modeled waveforms from the outputs of the Blumlein and NLTL with a composite of 25% NZF inclusions in PDMS. The first oscillation from the NLTL output increases compared to its input, indicating the possible production of a single high frequency cycle. The subsequent cycles dampen quickly and the peak-to-peak magnitudes of these cycles typically vary from 140% to 154% of those of the input pulse, indicating the production of no major oscillations.

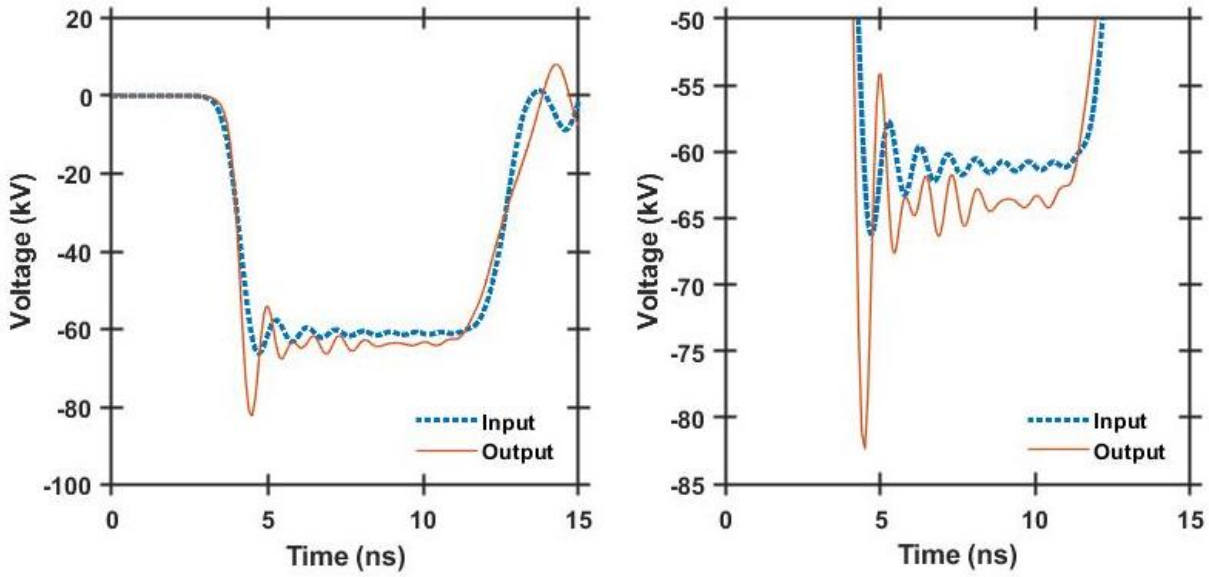

Figure 32. (a)The input waveform to the NLTL produced by the Blumlein modulator and the output waveform from the NLTL and (b) zoomed in view of the flat top of the input and output waveform from the NLTL. The NLTL simulated contains a dielectric of 25% volume fraction of NZF in a silicone matrix.

Figure 33 compares the inputs and outputs from the 25% NZF composite NLTL for different Blumlein pulse amplitudes in terms of both voltage and voltage normalized to the peak voltage of the Blumlein generator. The initial single cycle produced by the NLTL increases with increasing input voltage; however, the number of oscillations does not change with increasing charging voltage. Also, changing the peak Blumlein voltage does not change the relative amplitude of the initial oscillation. Increasing the pulse amplitude from 10 kV to 60 k decreases the rise time of the output pulse from 1.05 ns to 0.6 ns.

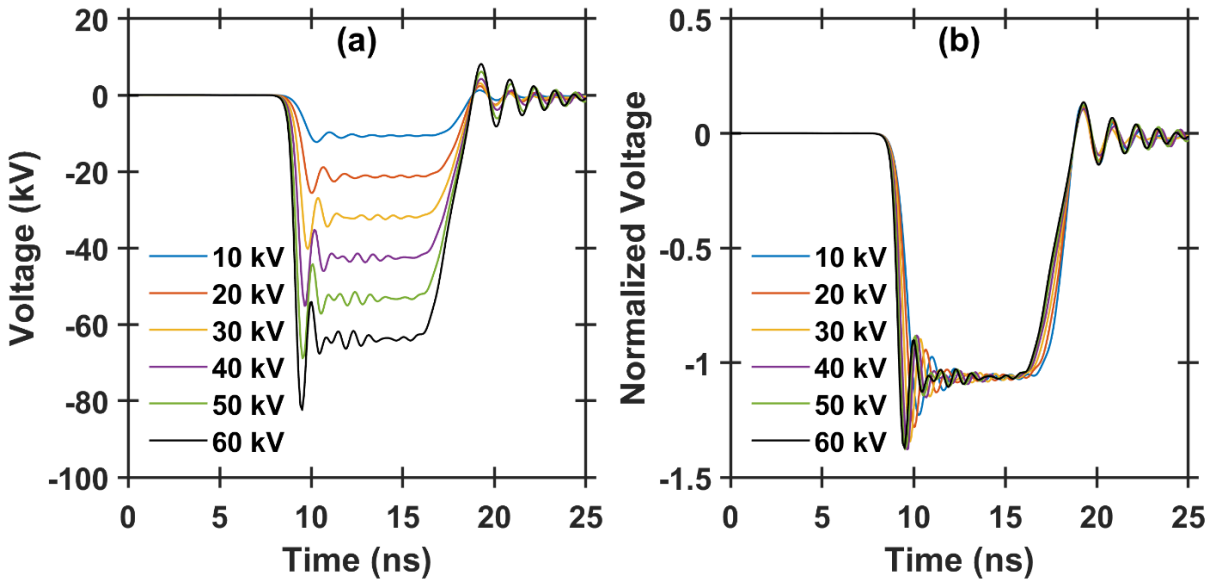

Figure 33. The simulated (a) output voltage waveforms and (b) normalized output waveforms of a NLTL with a dielectric composite comprised of 25% NZF in a silicone matrix driven by a Blumlein modulator.

Figure 34 shows that using a Blumlein to drive an NLTL with 10% BST/15% NZF in a silicone matrix yielded a single cycle of RF with a much lower peak-to-peak amplitude than the 25% NZF NLTL. Figure 35 compares the output pulses from the NLTL normalized to the peak voltage of the Blumlein generator to compare the initial spike on the voltage waveform for different applied voltages. While the amplitude of the initial peak increases with increasing charging voltage, the *relative* amplitude of the initial peak does not increase with increasing charging voltage. The initial peak is greater at the output of the NLTL than the output of the Blumlein

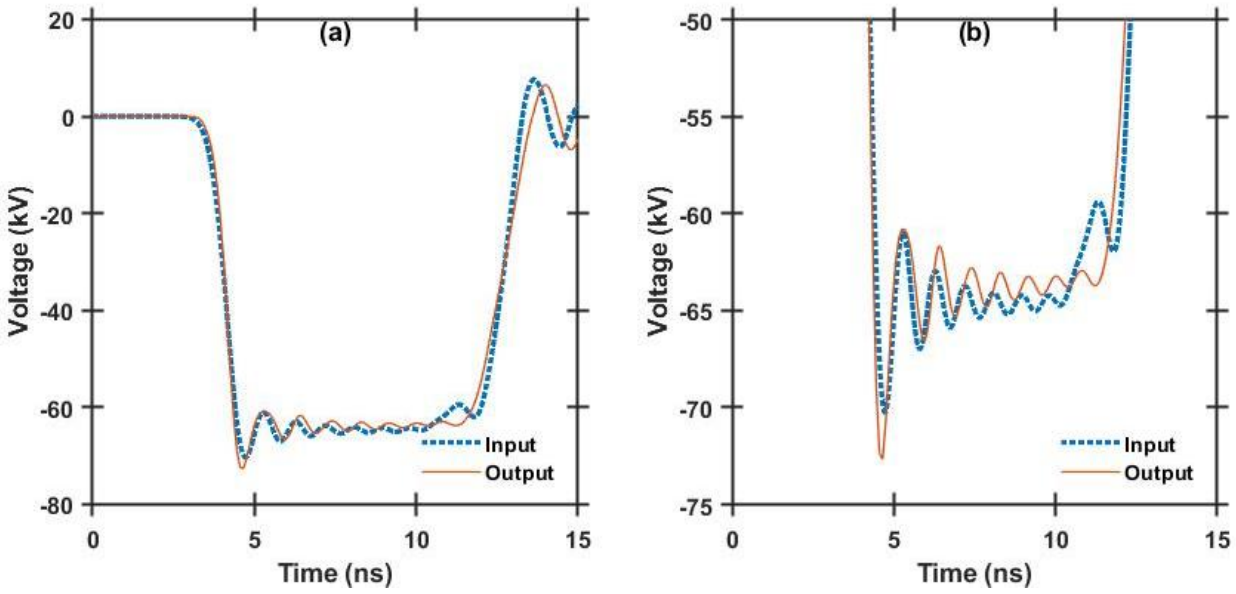

Figure 34. (a)The simulated input waveform to the NLTL produced by the Blumlein modulator and the output waveform from the NLTL and (b) zoomed in view of the flat top of the input and output waveform from the NLTL. The simulated NLTL contains a composite of 10% BST and 15% NZF volume fractions in a silicone matrix.

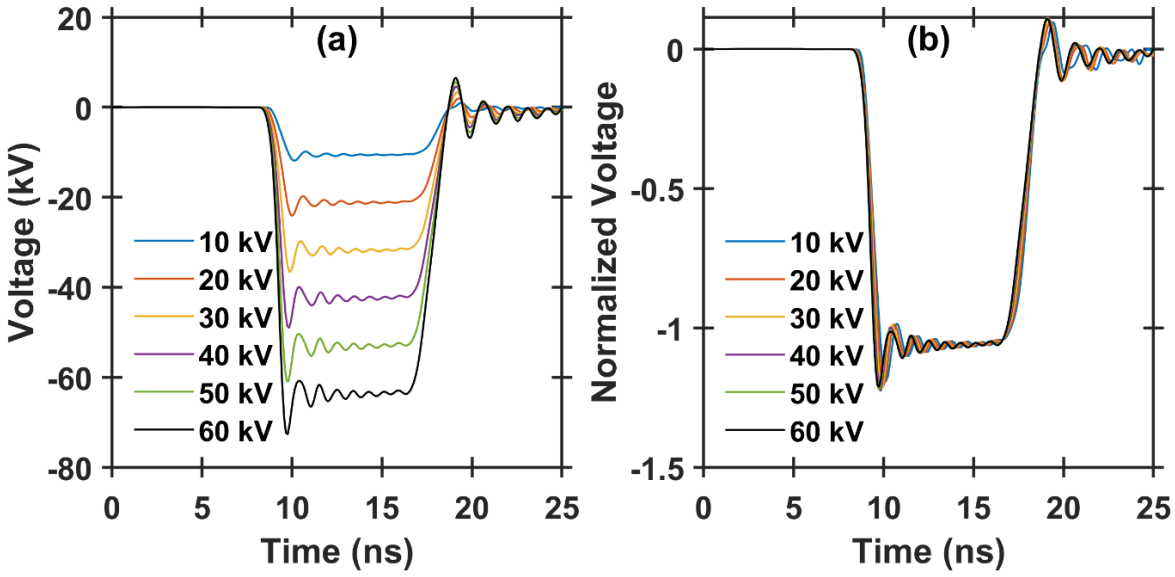

Figure 35. The simulated (a) output voltage waveforms and (b) normalized output waveforms of a 20 in NLTL with a composite comprised of 10% BST and 15% NZF in a silicone matrix driven by a Blumlein modulator.

We next performed the same simulation for the 15% BST/10% NZF composite NLTL. Figure 36 shows the input pulse to the NLTL generated by the Blumlein generator and the resulting output pulse from the NLTL. As for the other volume loadings, the NLTL output waveform did not exhibit any additional oscillations compared to the input pulse from the Blumlein modulator, although the amplitude of the initial peak was slightly higher than the initial peak on the output pulse from the Blumlein. Fig. 37 shows that the peak voltage of the output of the NLTL is constant when it is normalized to the peak voltage of the Blumlein generator output. While the initial spike increased in amplitude with increasing charging voltage, the *relative* amplitude remained the same. No applied voltages or composite combinations produced clear oscillations on the output of an NLTL driven by a Blumlein generator.

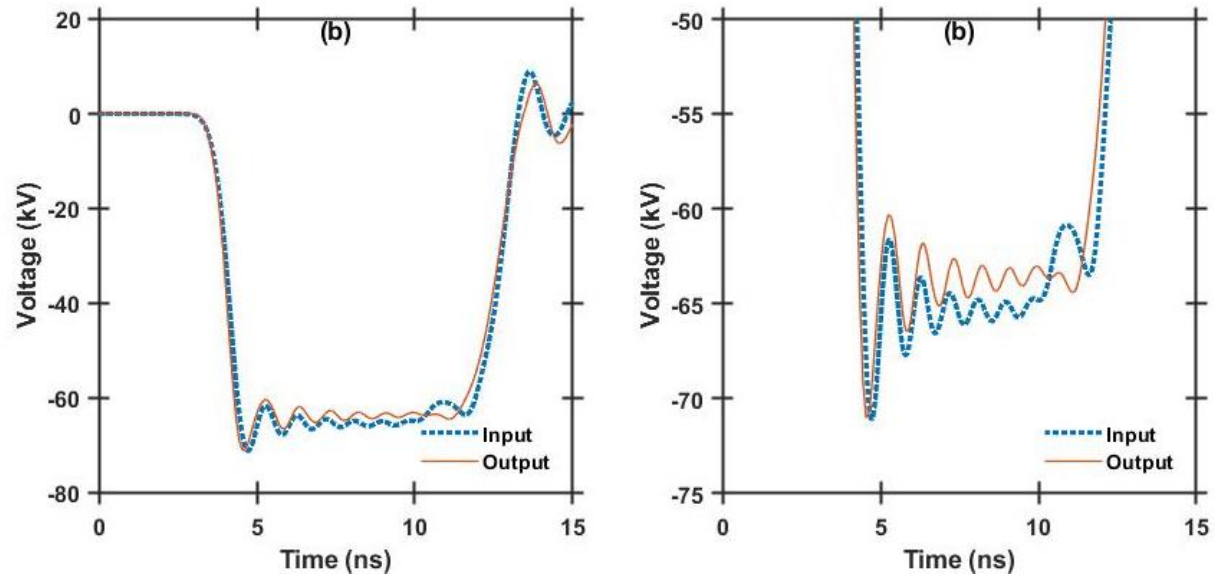

Figure 36. (a) The input waveform to the NLTL produced by the Blumlein modulator and the output waveform from the NLTL and (b) zoomed in view of the flat top of the input and output waveform from the NLTL. The NLTL simulated contains a dielectric of 15% BST and 10% NZF volume fractions in a silicone matrix.

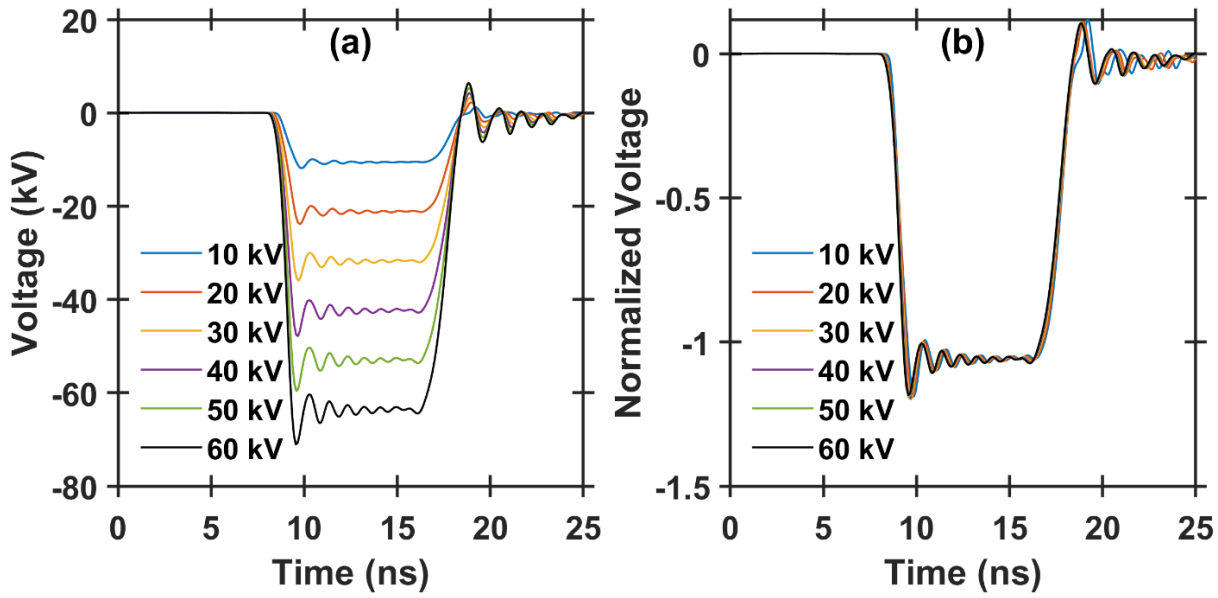

Figure 37. The simulated (a) output voltage waveforms and (b) normalized output waveforms of a NLTL with a dielectric composite comprised of 15% BST and 10% NZF in a silicone matrix driven by a Blumlein modulator.

4.3.2 Experiments Using the Blumlein Generator

We performed a power spectrum density (PSD) of the output pulses and analyzed the data to determine the frequencies not present in the initial pulse by subtracting the computed PSDs of the input pulses from the output pulses in the frequency domain. This gives the power produced at a given frequency due to pulse propagation through the NLTL. Fig. 38 shows representative pulses for the input and output of a 25% NZF composite NLTL exposed to a 30 kV pulse from the Blumlein; the input and output pulses of the other two NLTLs behaved similarly.

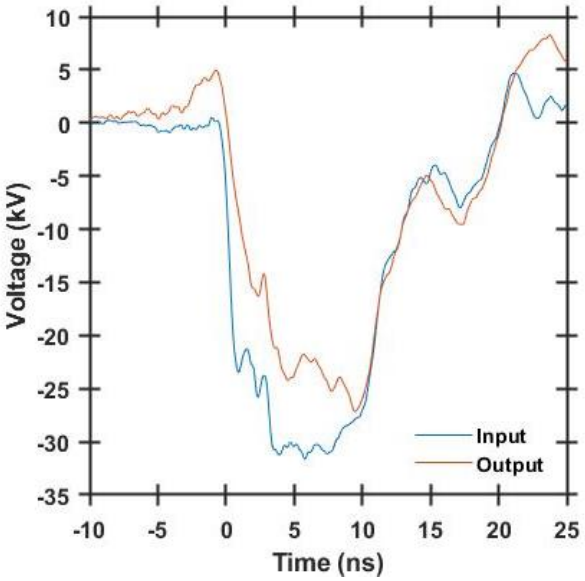

Figure 38. Representative input and output waveform for a 25% NZF composite NLT with a 30 kV input pulse.

There is a clear shift in the output waveform from the input waveform as it moves through the NLTL, with a single cycle of oscillation appearing on the rise time of the output pulse. Figure 39 shows that the output of the 25% NZF develops multiple frequencies with increasing input pulse voltage. A peak arises at 1.1 GHz and a smaller peak arises at 2.2 GHz for an input pulse of 30 kV. Figure 39(a) shows that lower input pulse amplitudes of 20 kV and 25 kV induce output frequencies on either side of the 1.1 GHz peak produced at 30 kV, although the peaks in the output spectrum have a higher trough on either side of the peaks than the 1.1 GHz peak. There is also a large peak at 750 MHz for peak applied voltages of at least 15 kV.

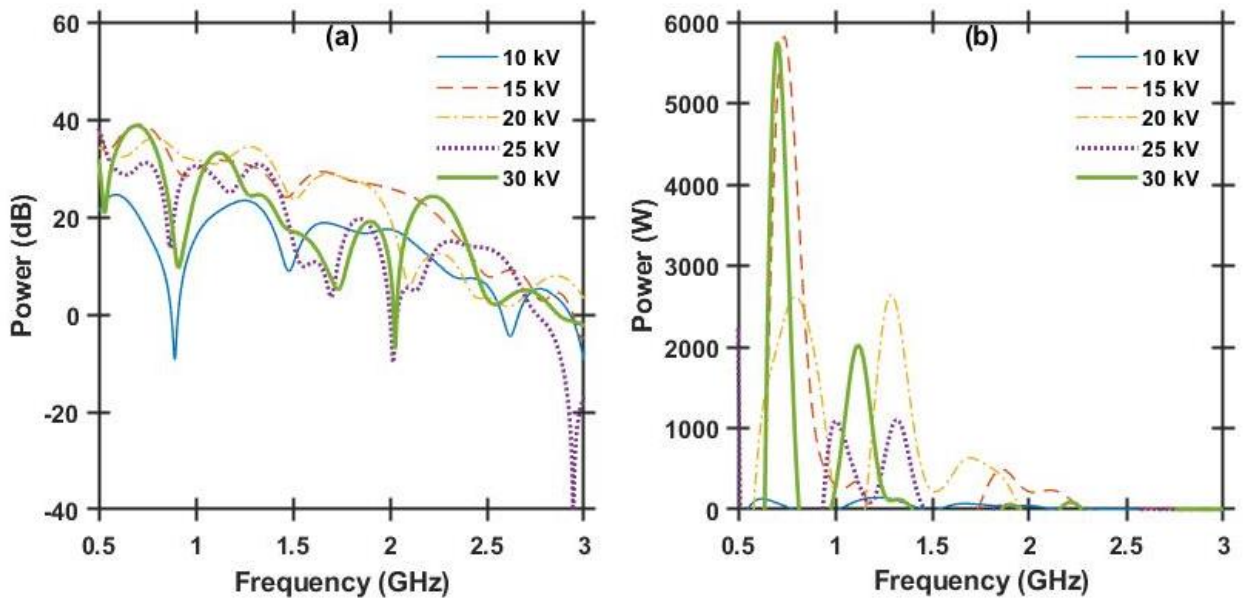

Figure 39. The (a) output spectrum of a 25% NZF composite NLTL and the (b) generated frequency content at the output of the 25% NZF composite NLTL.

We also biased the NLTL with a magnetic field using a current supply (Acopian model Y050LX2B2880-DI01) and a solenoid wrapped directly on the NLTL, but electrically isolated using electrical tape, while applying a 30 kV pulse. Figure 40 shows that the amplitude of the output pulse generally increased with increasing bias field, although this is not consistent across all frequencies. Figure 40(b) shows that a 50 kA/m bias produces the highest power output at the given frequencies; however, the peak frequency increases for applied biases of 40 kA/m and 50 kA/m. Although increasing the bias generally increases the output power, we do not observe the clear trend observed in other NLTL studies [109], as demonstrated by the lower power produced for a bias of 39.95 kA/m compared to 29.52 kA/m. This indicates that the Blumlein is not an ideal modulator to drive the NLTL.

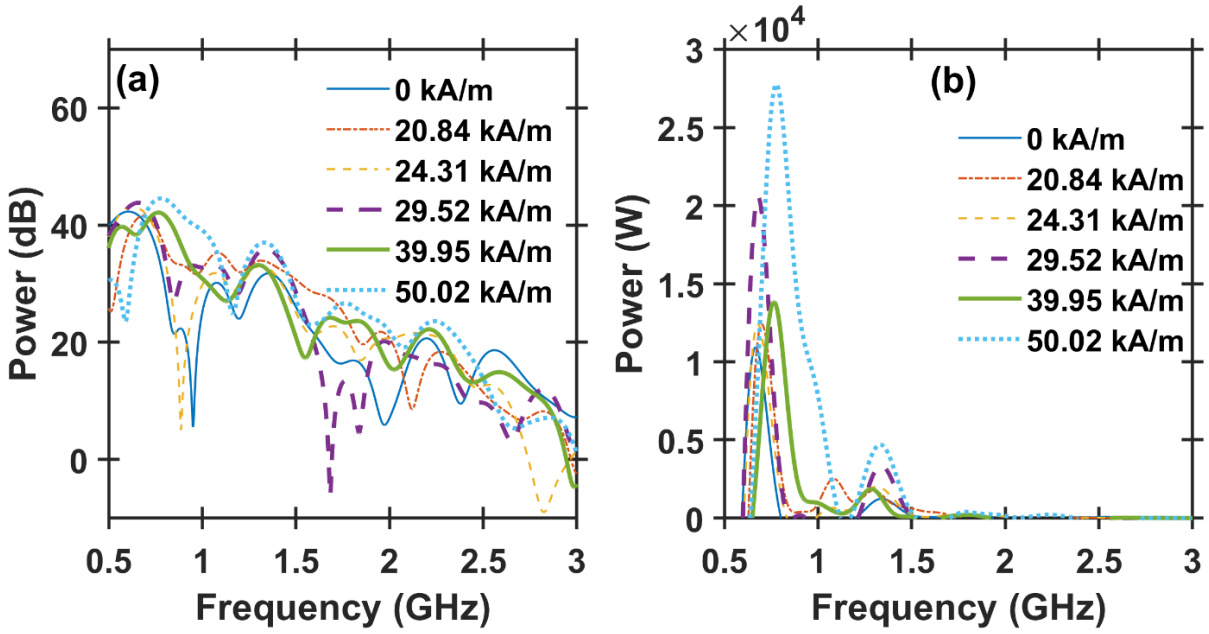

Figure 40. The (a) output spectrum of a 25% NZF composite NLTL and the (b) generated frequency content at the output of the 25% NZF composite NLTL.

Figure 41 shows that the output of a 10% BST/15% NZF composite NLTL driven by a Blumlein generator develops a peak at 1.3 GHz. Figure 41(a) shows that while the amplitude of the peak is slightly higher for a 25 kV input pulse than the 30 kV input pulse, the trough before the peak is much higher than the 30 kV peak. As the input pulse voltage increases, the output frequency peak at 1.3 GHz increases in amplitude and the trough decreases in amplitude, indicating a focusing of energy at that frequency.

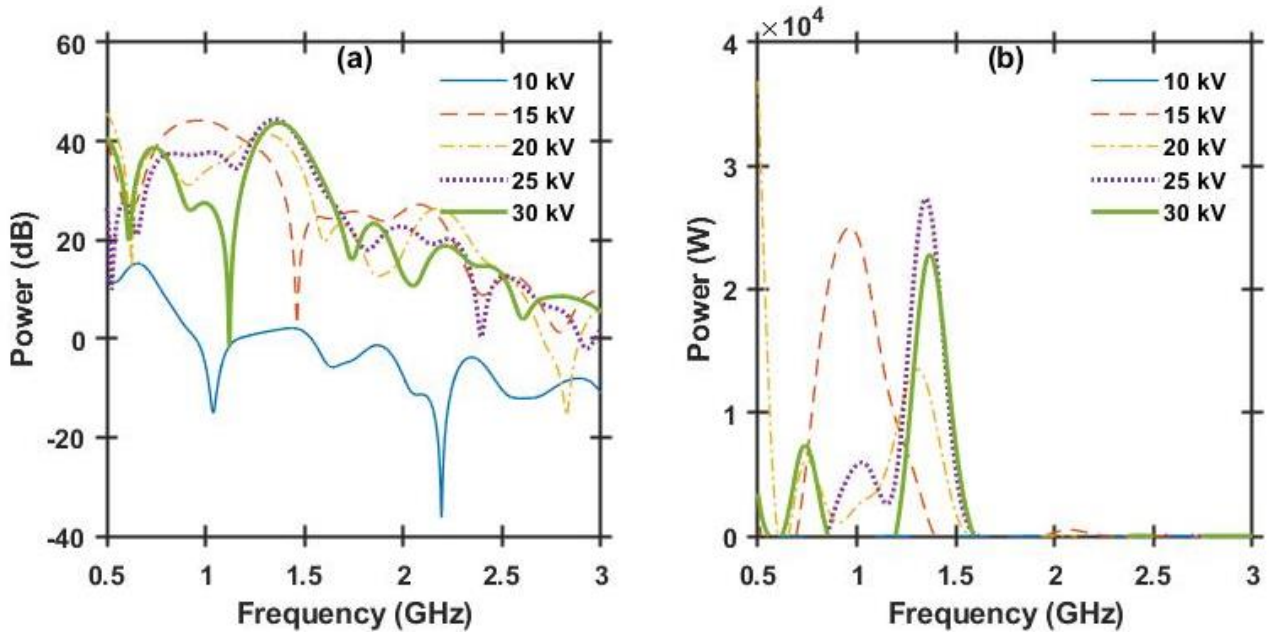

Figure 41. The (a) output spectrum of a 10% BST and 15% NZF composite NLTL and the (b) generated frequency content at the output of the 10% BST and 15% NZF composite NLTL.

Figure 42 shows the impact of magnetic field bias on output spectrum for a 10% BST/15% NZF composite NLTL driven by a 30 kV output pulse from the Blumlein modulator. The peak at 1.3 GHz observed for the unbiased line remained. We observed no general trend between the output power at the 1.3 GHz peak and the biasing field. The highest bias field of 50.32 kA/m produced a slightly higher peak than the unbiased line at a lower frequency (1 GHz). This again shows that the Blumlein modulator is not an optimal generator for driving NLTLs when seeking to achieve strong oscillations.

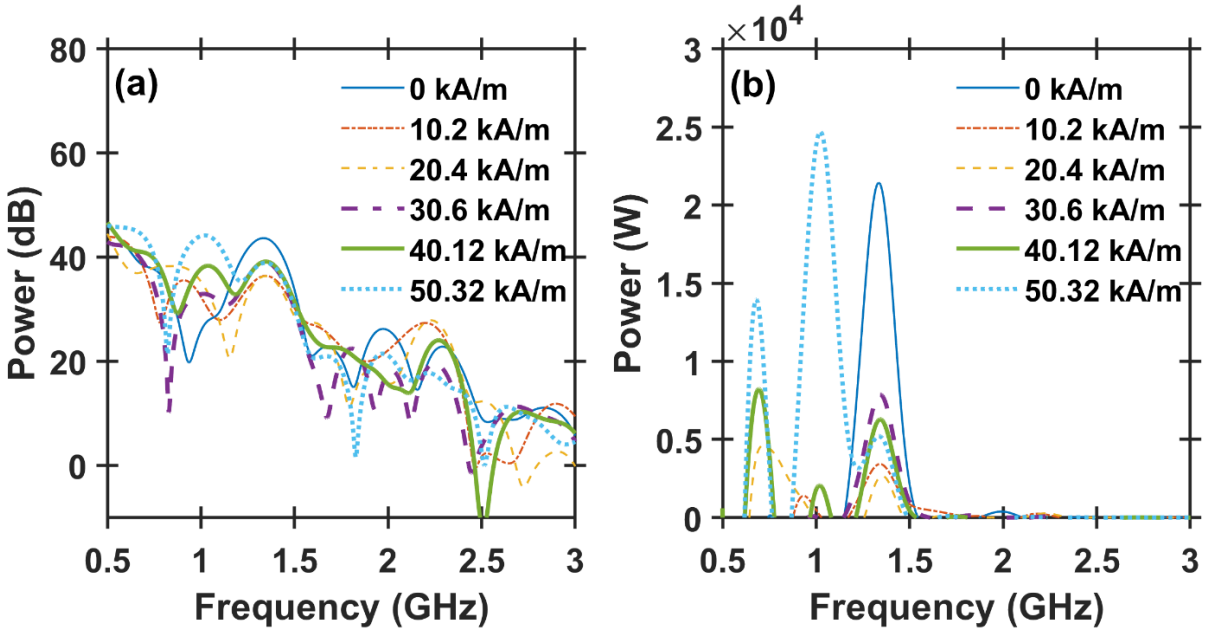

Figure 42. The (a) output spectrum of a 10% BST and 15% NZF composite NLTL and the (b) generated frequency content at the output of the 10% BST and 15% NZF composite NLTL.

Figure 43 shows that a 15% BST/10% NZF composite NLTL generates frequency at 1.3 GHz. Increasing the input pulse voltage increases the amplitude of the peak at 1.3 GHz and reduces the minimum power prior to the peak. Figure 43(a) shows that while the 15 kV input pulse produces a relatively high peak at 1.3 GHz, the output exhibits more lower frequency content than higher voltage input pulses. The amplitude of the frequencies adjacent to the peak show a higher power output than the higher voltage peaks, resulting in a less defined peak. The amplitude of the 1.3 GHz peak is slightly lower than that of the corresponding peak for the 10% BST/15% NZF composite NLTL.

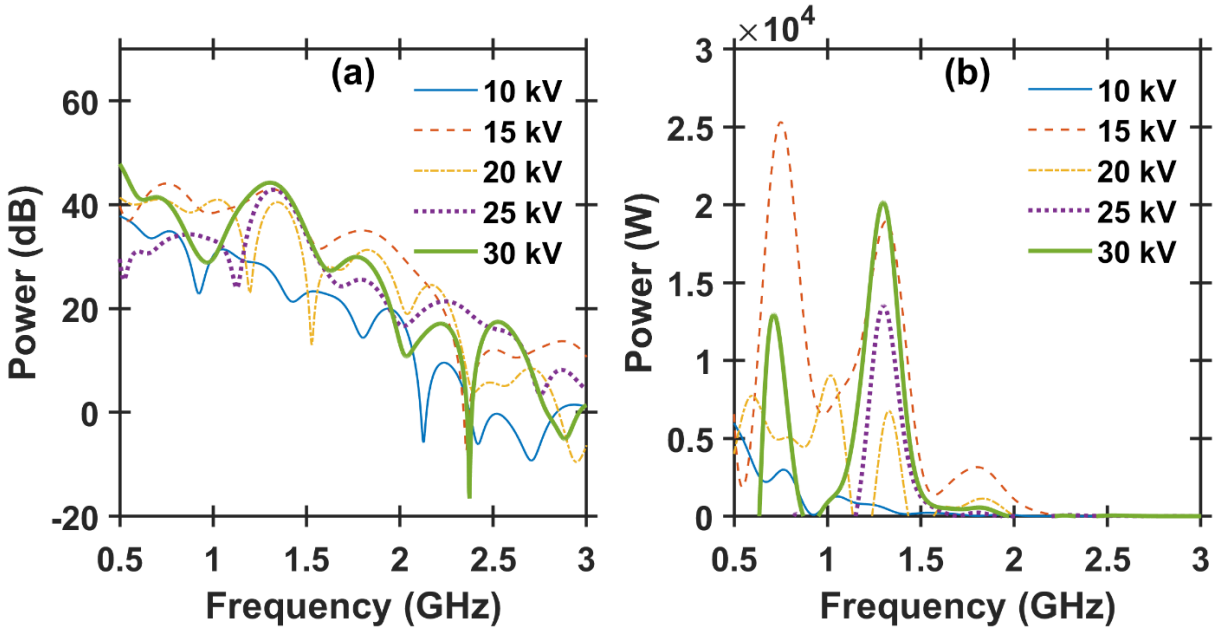

Figure 43. The (a) output spectrum of a 15% BST and 10% NZF composite NLTL and the (b) generated frequency content at the output of the 15% BST and 10% NZF composite NLTL.

The 15% BST/10% NZF composite NLTL was also biased with a magnetic field ranging from 10 kA/m to 50 kA/m, as shown in Figure 44. The output frequency at 1.3 GHz did not change from the unbiased line and, again, there is no clear trend in the power production at that frequency as a function the magnetic bias field.

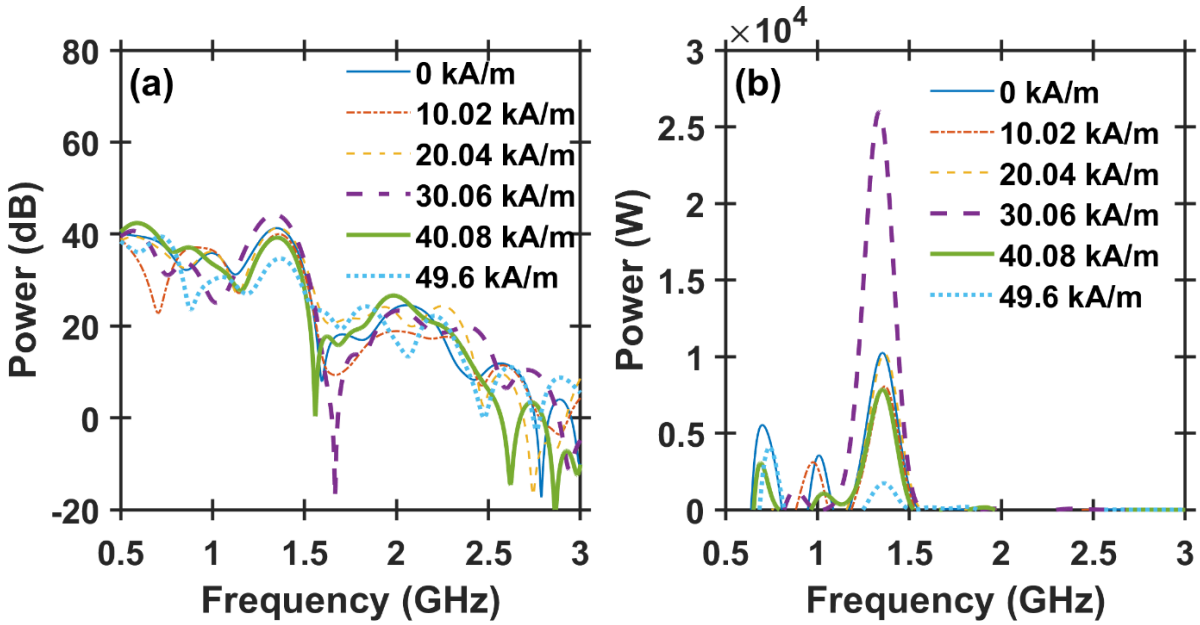

Figure 44. The (a) output spectrum of a 15% BST and 10% NZF composite NLTL and the (b) generated frequency content at the output of the 15% BST and 10% NZF composite NLTL.

4.3.3 Modeling NLTL driven by pulse forming network

To determine whether the absence of strong oscillations was due to the NLTL or the Blumlein generator, we simulated the same NLTL in LT Spice to simulate the same NLTL with a PFN in place of the Blumlein modulator. Figure 45 shows that using the PFN to drive a 25% NZF NLTL caused significant oscillations not present in the PFN output that increased in duration and amplitude with increasing PFN output voltage. The output frequency generated was 1.1 GHz independent of voltage. The longest RF burst occurred with a 60 kV input pulse and produce a 6 ns burst of oscillations. Figure 38 shows that the output frequency matched well with the measured output of the 30 kV pulse, although the strong oscillations shown in Figure 45 are not present in Figures 33, 35 or 37.

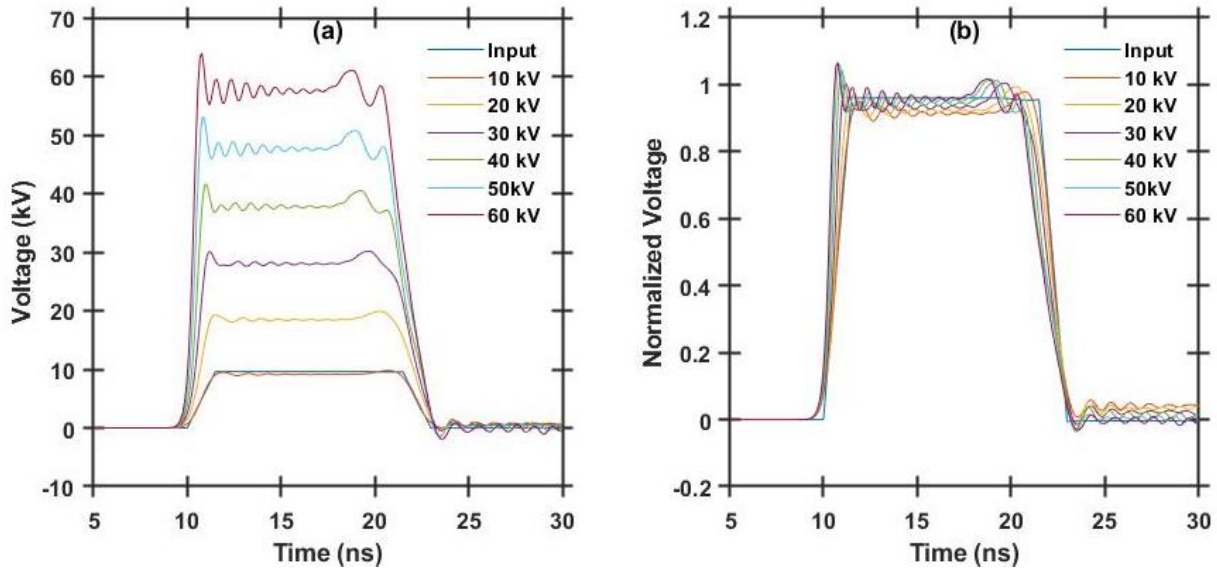

Figure 45. The (a) output of the 25% NZF 20 in NLTL and the (b) normalized output pulse of the 25% NZF 20 in NLTL driven by a PFN.

Figure 46 shows that the output of the 10% BST/15% NZF composite NLTL produced higher frequency oscillations at 1.2 GHz with oscillation amplitude and duration increasing with NLTL input pulse amplitude; however, upon reaching a maximum peak voltage of 10 kV, the NLTL no longer produced oscillations. This limitation arises due to the saturation voltage V_{SAT} in (2); the exact value of V_{SAT} is currently uncharacterized and measurements at these voltages and frequencies are difficult, although the development of custom measurement devices is ongoing. The output frequency is similar to the measured output frequency of 1.3 GHz for the 10% BST/15% NZF line driven by the Blumlein generator, as shown in Figure 41.

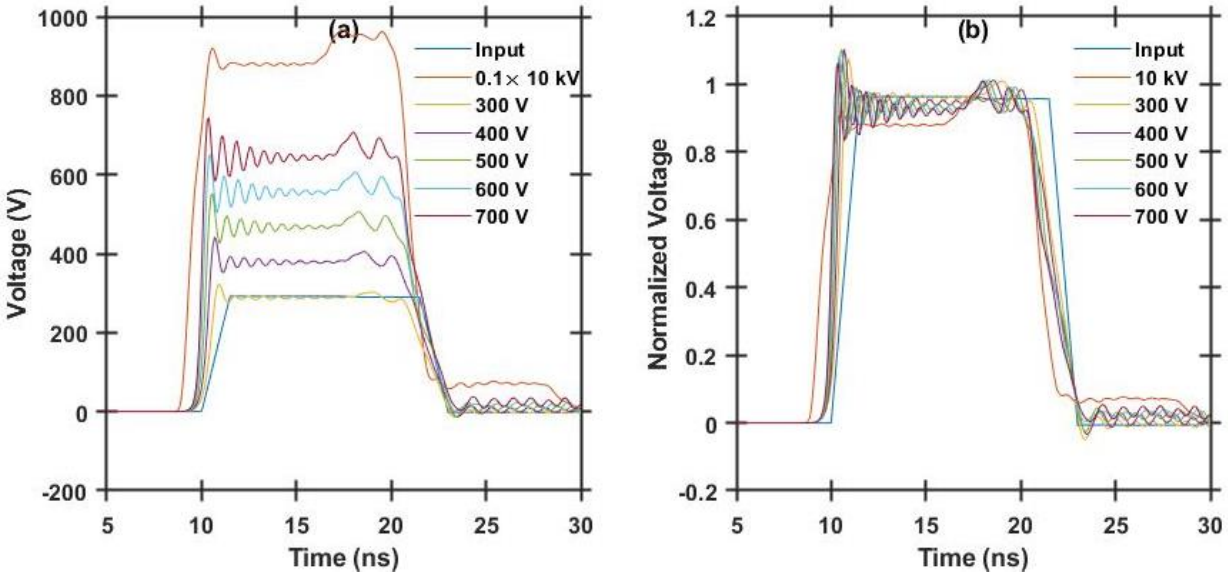

Figure 46. The (a) output of a 10% BST 15% NZF NLTL and the (b) normalized output of a 10% BST 15% NZF NLTL driven by a PFN.

The output of the 15% BST/10% NZF composite also exhibited oscillations with increasing peak-to-peak voltage and duration with increasing input voltage. The input voltage and oscillations generation were again limited by V_{SAT} in (2), as shown by the reduced oscillation magnitude for a 10 kV PFN output in Figure 47. The output frequency is 1.2 GHz, which is slightly lower than the 1.3 GHz measured for the Blumlein output in Figure 43.

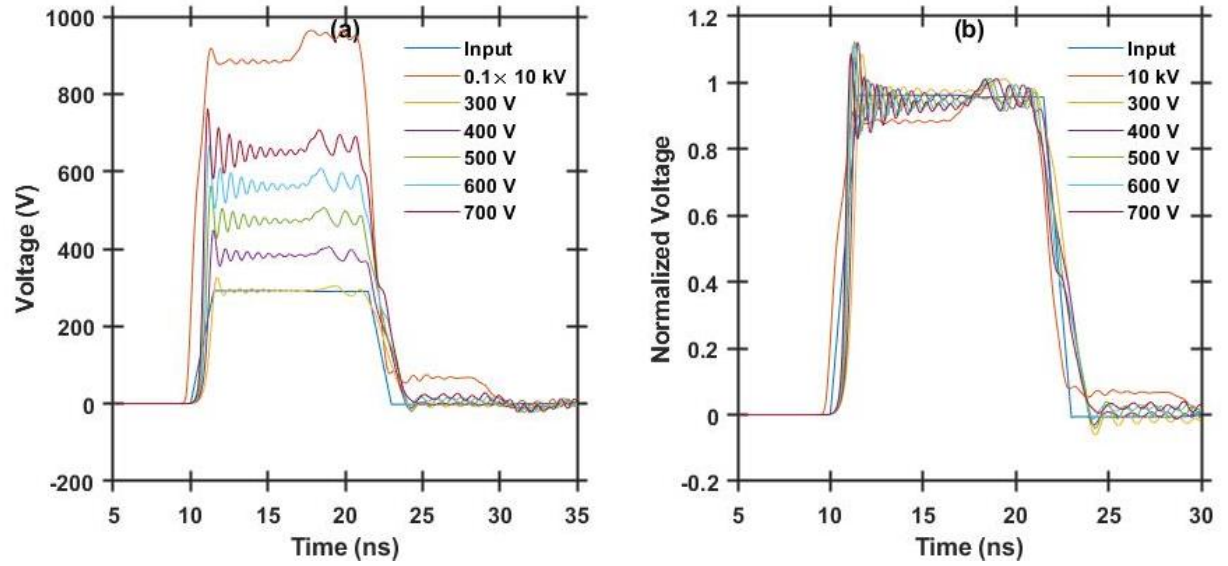

Figure 47. The (left) output of a 15% BST 10% NZF NLTL and the (right) normalized output of a 15% BST 10% NZF NLTL driven by a PFN.

4.4 Discussion

Using a Blumlein modulator to drive an NLTL generated minimal RF oscillations both in experiments and simulations. Although the Blumlein-driven NLTL produced some frequency content not present in the input waveform, it did not generate clear oscillations. The experimentally observed frequencies aligned well with those observed in LT Spice simulations where the NLTL was driven by a PFN, showing that the low power frequency generation, when driven by the Blumlein, is most likely due to the nonlinear composites. Single cycle high frequency oscillations were generated both experimentally and in simulations for NLTLs comprised of composites with different volume fractions of BST and NZF when driven by a Blumlein generator.

While the rise time of the voltage pulse produced by the Blumlein modulator is sufficient to produce oscillation [1], [2], [11], [27], [33], [35], [104], [109], [110], [112], [114], [116]-[118], [120], [123], [126], [128], [130], [181],[190]-[192], we do not observe sustained RF when applying the Blumlein to composite NLTLs either experimentally or through simulations. However, our simulations show that replacing the Blumlein generator with a standard PFN with the same pulse parameters induces output oscillations with sustained RF. The primary difference between the Blumlein generator and the PFN is the mechanism by which the pulse is generated. Blumlein modulators apply a pulse on both the inner and outer conductor of the NLTL [193], shown in Figure 48, which mitigates the electric field to which the NLTL material is exposed. On the other hand, the PFN applies a fast high voltage pulse with similar amplitude and rise- and fall-times to the center conductor with the outer conductor held at ground potential. This indicates that using a modulator that applies a signal directly to the center conductor of the NLTL produces stronger oscillations and moves the material into a nonlinear state, while generating an electric field difference by applying voltages to both conductors does not. Previous experiments using a Marx generator that applied a voltage pulse directly to the center conductor generated RF output. Moreover, our simulations and those in prior studies [109], [110], [123] have shown that using a PFN to apply a voltage pulse directly to the center conductor will induce strong oscillations in the NLTL output.

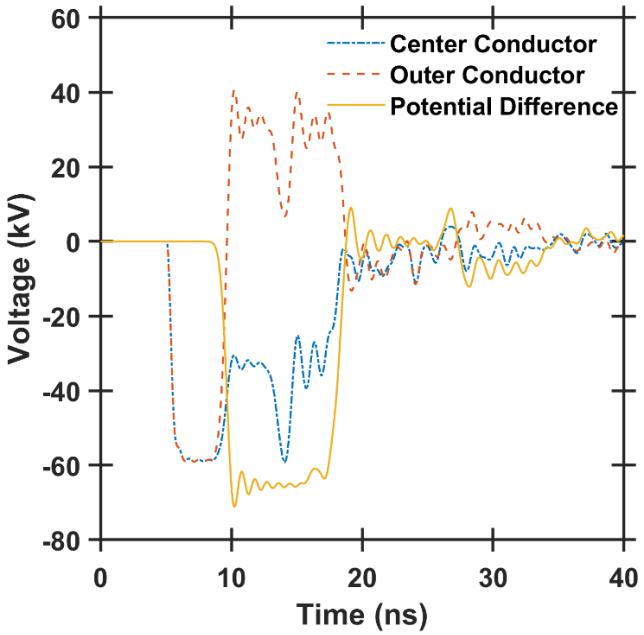

Figure 48. Simulated pulses generated by the Blumlein modulator on the inner and outer conductor of the NLTL.

Applying an external magnetic field bias also did not increase or alter the production of oscillations, even though we applied a larger magnetic field bias applied than in other gyromagnetic NLTLs [109], [110], [123] where the modulators applied comparable or lower voltage input pulses [109], [123] to produce clear oscillations. The inability to induce oscillations, even when applying a magnetic field bias, in combination with faster rise-time input pulses with equal or higher amplitude than in standard gyromagnetic NLTLs [109], [110], [123] indicates that the Blumlein is not an ideal modulator to drive NLTLs.

Future work will be to apply a high voltage pulse to NLTLs with the same composition using an inductive adder modulator [195] using a 50 Ω impedance. The inductive adder applies the pulse directly to the center conductor referenced to the outer conductor, which is ground. We will examine both biased and unbiased NLTLs to evaluate the shift in the output frequency and the pulse amplitude limit required to produce strong oscillations on the output. Future studies will further explore the impact of line length and rise-time on the effectiveness of composite NLTLs to guide future studies exploring the potential to tune output RF by adjusting inclusion material, shape, and volume fractions.

5. NONLINEAR TRANSMISSION LINE IMPLEMENTED AS PULSE FORMING LINE AND HIGH POWER MICROWAVE SOURCE

5.1 Introduction

Nonlinear transmission lines (NLTLs) are solid state high power microwave (HPM) sources that utilize nonlinear permittivity and/or permeability of materials to produce high power RF [133]. Conventional HPM sources use vacuum tubes, such as a magnetron, and require auxiliary systems, such as cryogenic cooling, electromagnets, high voltage modulator, and vacuum systems. NLTLs reduce this footprint by eliminating some of the auxiliary systems [133]. However, traditional NLTLs still require a high voltage modulator to apply a fast (< 10 ns rise time) pulse to the line [78].

High voltage modulators for HPM systems are typically Marx generators [7], [11], [111], [125], [127], pulse forming networks (PFNs) [182]-[184], or pulse forming lines (PFLs) [185]-[187]. Marx generators allow for compact voltage multiplication, but generally do not have very fast rise times (5-50 ns) [111], [196] without additional peaking sections. PFNs are compact and can provide large voltage outputs, although they are limited to the voltage threshold of the capacitors used. PFLs provide a square pulse based on the line's length and impedance and are limited by the voltage threshold of the dielectric material used. The PFN is a series of N LC ladders, made of physical capacitors C and inductors L, yielding a pulse width $\tau = N \times \sqrt{LC}$. The PFL is comprised of coaxial cables with a dielectric separating the central cable from a metal outer conductor. Coaxial cables can be modeled as a series of LC ladders, shown in Figure 49b, with the capacitance and inductance given per unit length and the pulse width a function of the length of the coaxial cable.

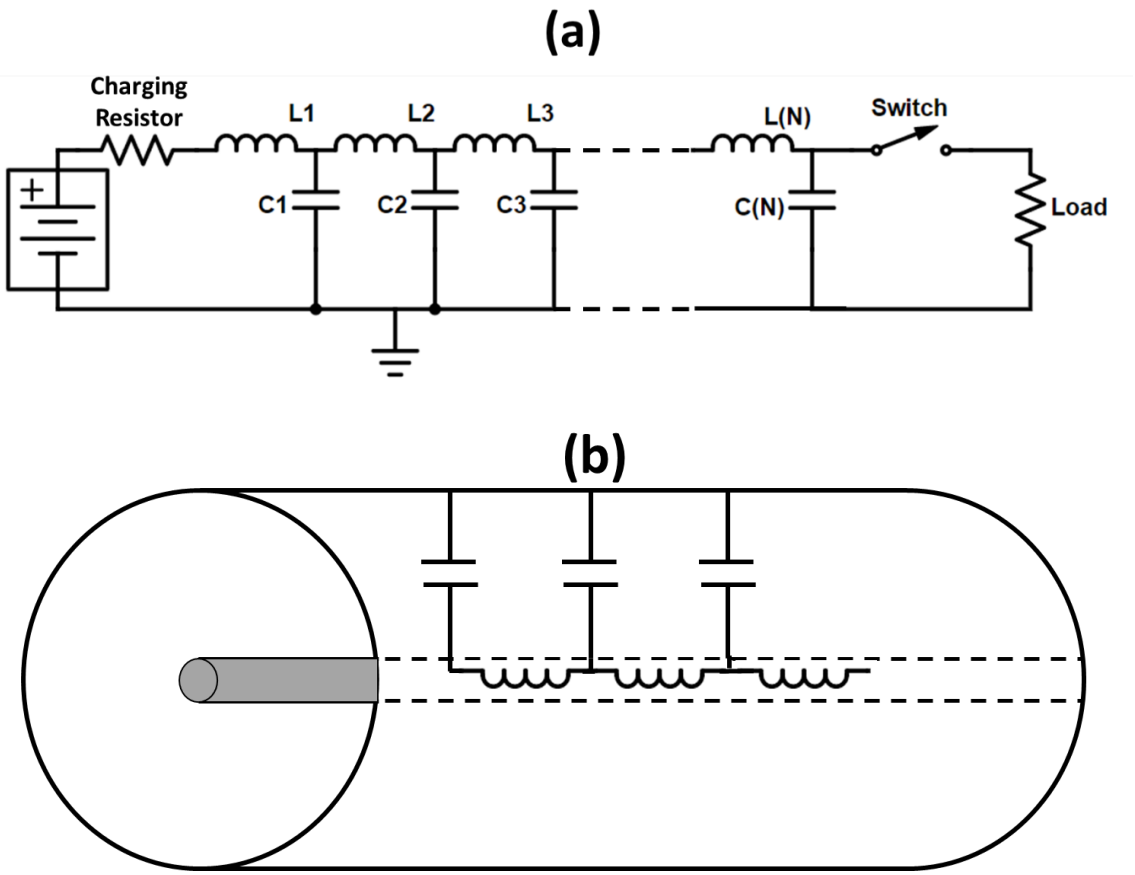

Figure 49. Representative circuits for (a) a pulse forming network (PFN) and a (b) pulse forming line (PFL).

NLTLs are traditionally comprised of ferromagnetic or ferroelectric materials [133]. Traditional gyromagnetic NLTLs utilizing ferromagnetic materials, whose permeability varies with magnetic field, rely on the precession of the magnetic moments around an effective magnetic field to produce RF [1]. The precession of the magnetic moments is described by the Landau-Lifshitz-Gilbert equation. Ferroelectric materials, whose permittivity varies with electric field, have a permanent polarization vector due to an offset atom in the crystalline lattice [78], [104]. When the material is near the Curie temperature, the offset atom can move to alternate stable positions, thus rotating the polarization vector. Common ferroelectric materials include barium titanate (BT) [35], strontium titanate (ST), and barium strontium titanate (BST) .

This Chapter further reduces the footprint required for NLTL systems by eliminating the modulator portion of the HPM system. The NLTL is designed in a coaxial geometry to create a PFL. The dielectric material consists of BST and nickel zinc ferrite (NZF) inclusions in a silicone (PDMS) matrix [179]. We selected BST because it has the lowest Curie temperature between BT,

ST, and BST (25°C), where the greatest nonlinear response occurs. The NLTL is then charged to a set voltage; a pressurized spark gap switch then discharges the voltage with a rise time of ~2 ns. The nonlinear permittivity and permeability of the BST and NZF inclusions, respectively, sharpen the waveform as it propagates down the line to the load. Once the wave has sharpened, an electromagnetic shockwave is formed in the line, creating magnetic moments in the NZF that cause the polarization vector in the BST to oscillate. The magnetic moments in the NZF precess around the magnetic field of the line to produce RF in the low GHz range. Section 5.2 describes the manufacturing, experimental, and modeling methods, section 5.3 presents the results of the experiments and simulations, and section 5.4 discusses the results.

5.2 Methods

5.2.1 NLTL Manufacturing

We construct a coaxial NLTL using a 1 in copper tube with an internal diameter of 0.75 in as the outer conductor and a 0.5 in copper rod as the center conductor to create a 10 Ω impedance NLTL. The composites were made by weighing the base (Part A PDMS Sylgard 184) and adding the required amounts of NZF (FP350 PPT Technologies) and BST (HBS-8000 TPL Inc.) to achieve the proper volume loading. The mixtures were then stirred by hand for 5 min to incorporate the powders into the PDMS base. We next placed the mixtures in a planetary centrifuge (Thinky AR100) for 5 min at 400 rpm to thoroughly mix the composites. BST composites were then placed in an ultrasonic bath for 4 h to break up any conglomerations of powder. We added a curing agent at a ratio of 1:10 mass of the PDMS base, and mixed by hand for 5 min. The mixtures were then placed in a vacuum chamber at < 20 kPa for 30 min to remove any air bubbles. The samples were then poured slowly into the outer conductor at an angle to mitigate any addition of air into the mixture. Next, we placed the outer conductor with the composite into the vacuum chamber for 5 min at < 20 kPa to remove any air that had been introduced. The center conductor was then slowly inserted into the line and was centered by an aluminum block on the bottom of the line. Again, the mixture with the center conductor inserted was place in the vacuum chamber for 5 min at < 20 kPa to remove any gas that was introduced. Finally, another aluminum block was placed on top of the line to ensure the center conductor was centered and the line was place in an oven (Thermo Scientific Heratherm OGS180) at 100 °C for 2 h to cure.

5.2.2 NLTL Testing

A Glassman high voltage supply (Model EJ40P15) was used to provide the high voltage to the NLTL center conductor. We placed a 5 MΩ resistor in series between the NLTL and the power supply to limit the current output of the supply. A pressurized spark gap was placed on the output of the NLTL with a resistive load (HVR RT series) in series with the switch. The output of the resistive load was connected to the outer conductor of the NLTL. The outer conductor was then connected to the ground terminal on the power supply.

We measured the NLTL output voltage by connecting a 10 ft RG 58 cable (whose length was selected to prevent any reflections from the measurements from interfering with the original pulse) to a 2.5 GHz oscilloscope (Lecroy WaveRunner 625 Zi). A custom resistive voltage divider, consisting of a non-inductive resistor (HVR RT series) and a 30 dB attenuator (Pasternack PE7049-30), was used to measure the voltage signals.

5.2.3 NLTL Modeling

We modeled the NLTLs using LT Spice. The current dependent inductance was modeled by defining the flux through the inductor. The equation used to model the field dependence of the NZF inclusions was derived from [101] and used the form

$$\mu(I) = (\mu_i - \mu_S) \times \tanh(H/H_s)^2 + \mu_s \tag{5-1}$$

Where μ_i is the initial permeability, μ_s is the saturation permeability and is taken to be 1, H is the applied magnetic field, and H_s is the magnetic field at which the ferrite saturates, set to 2200 G. The curve fitting tool in MATLAB was used to fit experimental data from a previous study of the composites [174], shown in Figure 28.

The voltage dependent capacitance was calculated based on the voltage dependent permittivity, given by [181]

$$\epsilon(V) = (\epsilon_i - \epsilon_{SAT})V_{SAT} \tanh^2(V/V_{SAT}) + \epsilon_{SAT}, \tag{5-2}$$

where ϵ_i is the initial permittivity, ϵ_{SAT} is the saturated permittivity and is taken to be the permittivity of the composites with the given volume fraction of NZF, measured previously [179], V_{SAT} is the voltage at which saturation begins, and V is the voltage.

Figure 50 shows the circuit diagram of the NLTL used as a PFL to produce a square pulse that generates RF. We calculated the capacitance and inductance based on the dimensions of the NLTL and the material properties for the composites [179], [188]. The capacitance and inductance are given per inch and the NLTL is comprised of 20 LC segments to model the 20 in NLTLs that we manufactured and tested. We also simulated a linear transmission line (LTL) with fixed $C = C0$ and $L = L0$.

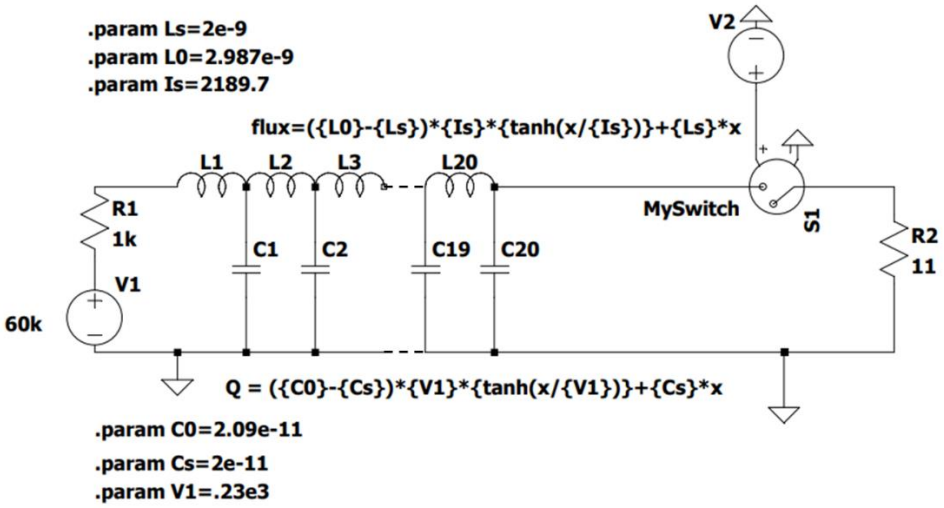

Figure 50. Circuit schematic for using a NLTL, made of composite with nonlinear dielectric and magnetic inclusions in a silicone matrix, as a PFL. Ls is the saturated inductance, L0 is the initial inductance, Is is the current at which the saturation takes place, C0 is the initial capacitance, Cs is the saturated capacitance, and V1 is the saturation voltage.

5.3 Results

5.3.1 Modeling

The simulation results show oscillations are produced on the flat top of the pulse, where conventional NLTLs produce their oscillations, and after the pulse at higher amplitudes, shown in Figure 51. The output for an NLTL with 25% NZF shows strong oscillations on the output that are much higher than the oscillations produced using a LTL. The frequency output of the 25% NZF NLTL oscillations is 800 MHz, which is slightly lower than the output of the 25% NZF line used as a NLTL and driven by the Blumlein modulator.

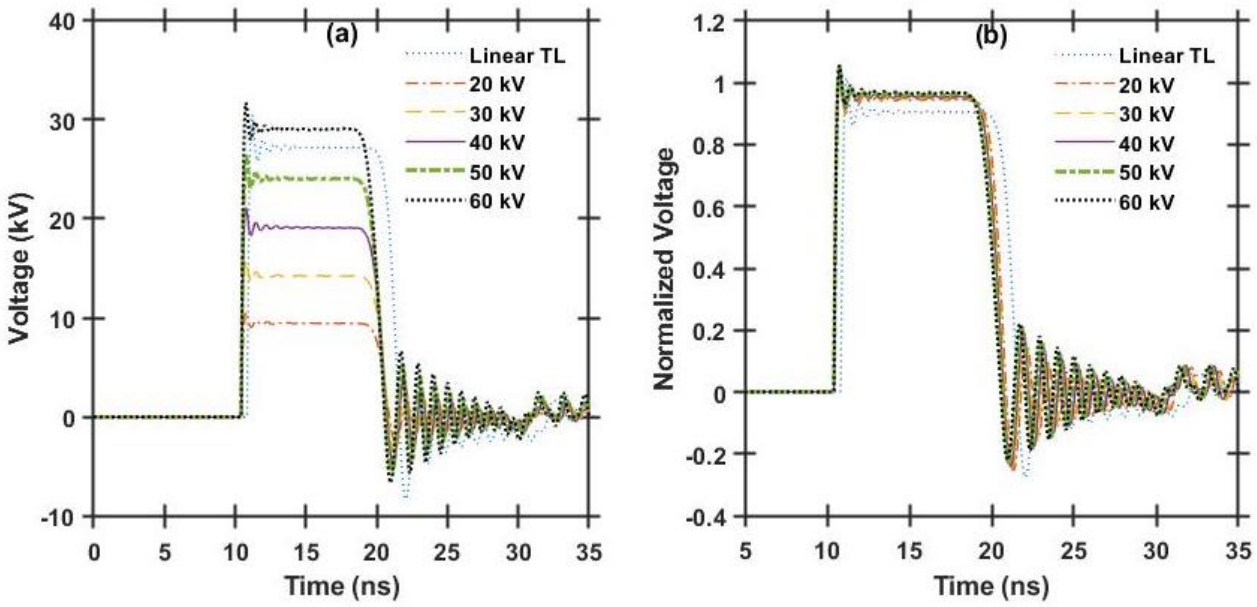

Figure 51. Simulated voltage waveforms at (a) the output and (b) the output normalized to the peak input voltage from a 25% NZF composite-based NLTL used as a PFL.

Figure 52 repeats the same analysis for a 10% BST/15% NZF composite-based NLTL. The output pulse of the NLTL is shorter in duration than the output pulse of the LTL due to the nonlinear permittivity of the composite. The high charging voltage of the line decreases the initial permittivity to the saturated state, which increases the propagation velocity and decreases the pulse width; V_{sat} determines the charging voltage for this to occur. Since we do not know V_{sat} for our composites, we kept it the same as previously [181]. The oscillations were also at a higher frequency (1 GHz) and amplitude than for the LTL.

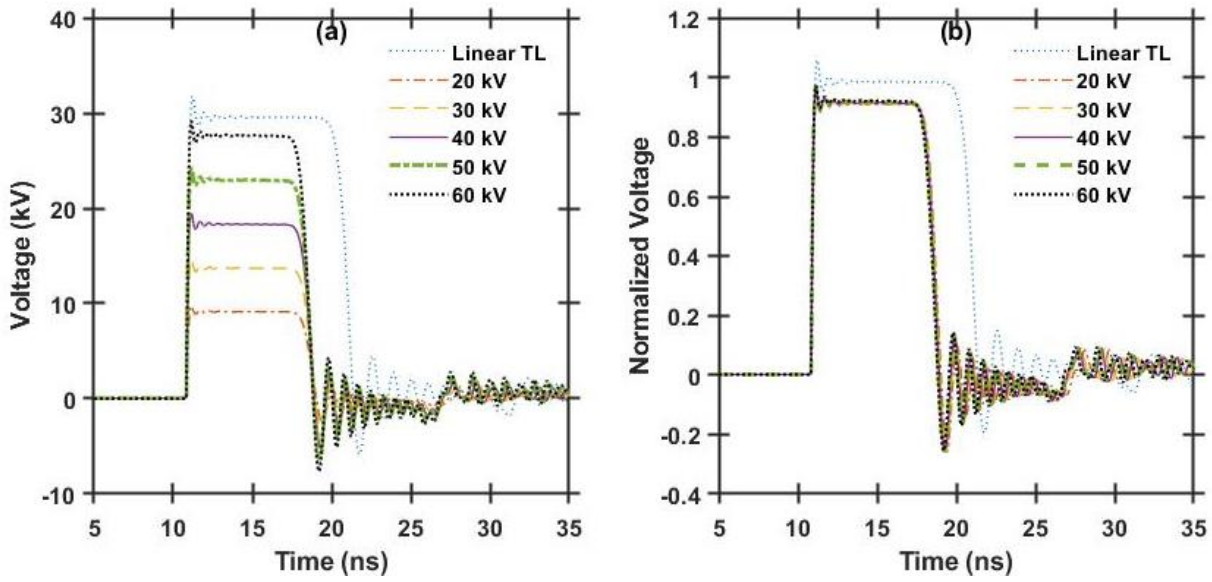

Figure 52. Simulated voltage waveforms at (a) the output and (b) the output normalized to the peak input voltage from a 10% BST/15% NZF composite-based NLTL used as a PFL.

Figure 53 shows simulations for an NLTL comprised of 15% BST and 10% NZF. Again, the output pulse is shorter in duration than that of the LTL due to the value of V_{sat}. The peak-to-peak amplitude of the first oscillation on the NLTL output exceeds that of the first oscillation for the LTL by 1 kV for the same charging voltage; subsequent oscillations increase with increasing charging voltage. The frequency of the oscillations is 1 GHz, which is slightly less than the frequency produced by the NLTL driven by the Blumlein modulator.

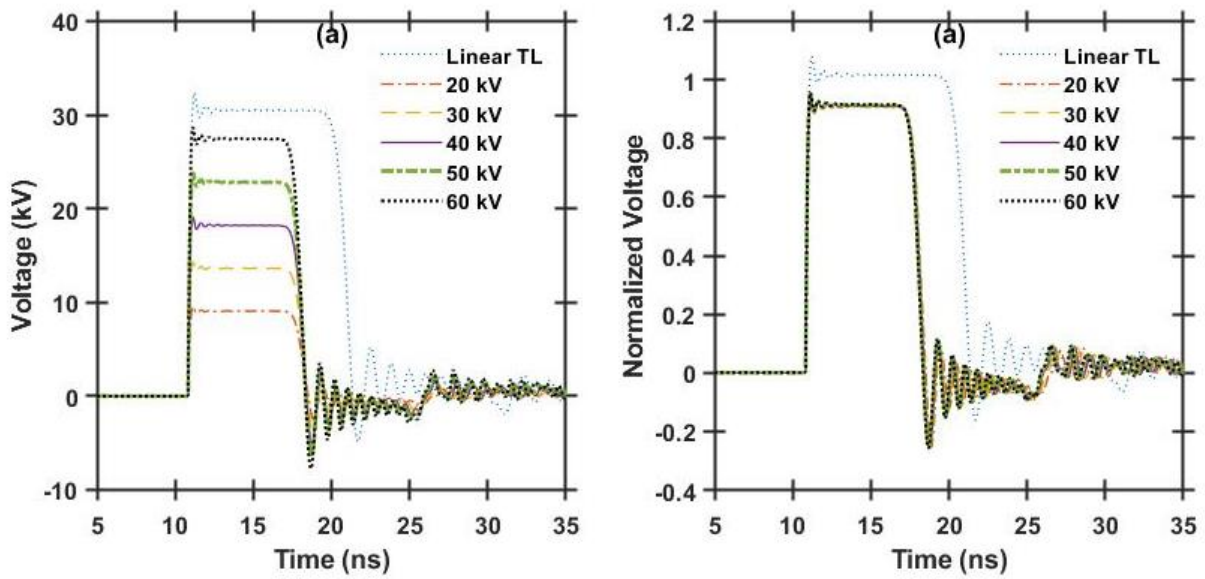

Figure 53. (a) Output waveform and (b) normalized simulation output from a 15% BST/10% NZF composite-based NLTL used as a PFL.

5.3.2 Experimental

The 25% NZF composite-based NLTL was tested at different voltages to determine the output frequency of oscillations. The output voltage was measured using a custom voltage divider, described in Appendix A, connected to the load side of the spark gap switch. Figure 54 shows that increasing the charging voltage decreased the rise time of the output pulse and caused oscillations to develop. The RF burst had a duration of 5 ns. Increasing the charging voltage produced a small current draw when only NZF inclusions were used, resulting in a voltage drop across the charging resistor that limited the maximum charging voltage of the NLTL.

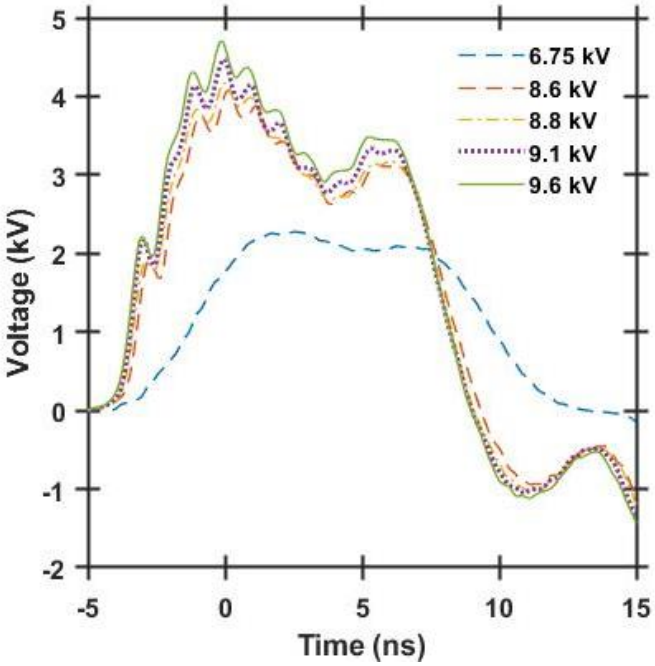

Figure 54. Measured output voltage waveforms from a 25% NZF composite-based NLTL used as a PFL.

The generated oscillations are centered around 950 MHz and occur at the peak of the output waveform, in agreement with the simulations. Figures 55 shows that the output power of the oscillations increases with increasing charging voltage. Figure 55(b) shows that while the power of the output peak is slightly higher for a charging voltage of 9.1 kV than for 9.6 kV, the output power is more concentrated in the 9.6 kV peak as the power in the frequencies just before the peak have are lower. For a charging voltage of 9.1 kV, the output power of the line exceeds 400 W at 950 MHz .

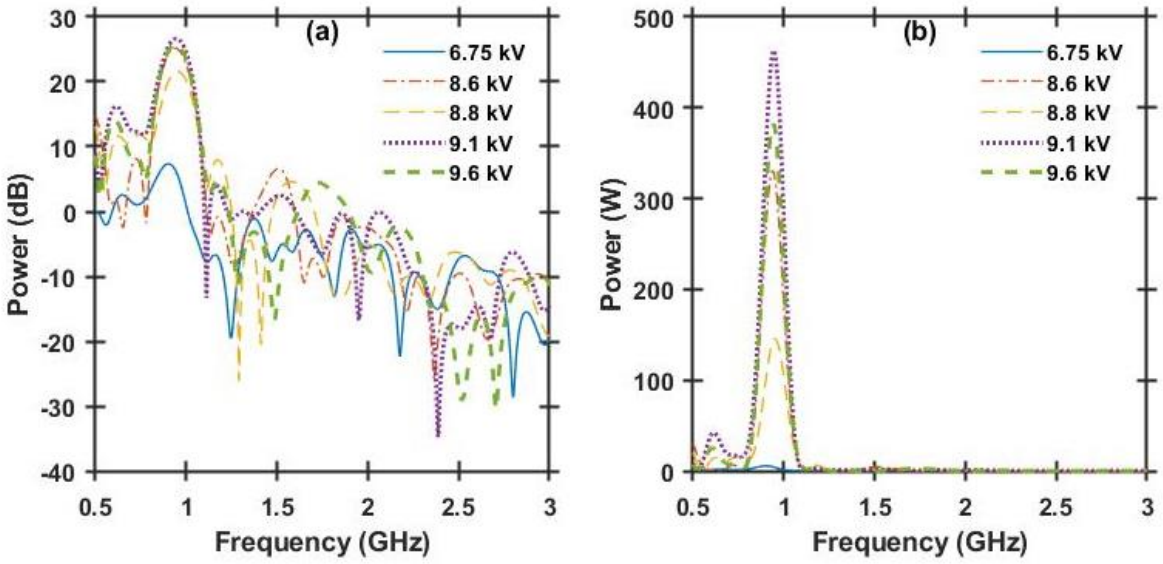

Figure 55. The output spectrum of a 25% NZF composite-based NLTL used as a PFL in (a) dB and in (b) linear power.

We repeated these measurements for a 10% BST/15% NZF composite-based NLTL. Figure 56 shows that increasing the charging voltage decreases the rise time of the output pulse and eventually induces oscillations that have a lower peak-to-peak amplitude than those in the flat top, in agreement with the simulations results from Fig. 52. Increasing the charging voltage to 14 kV creates oscillations after the pulse, which increase in amplitude with increasing charging voltage.

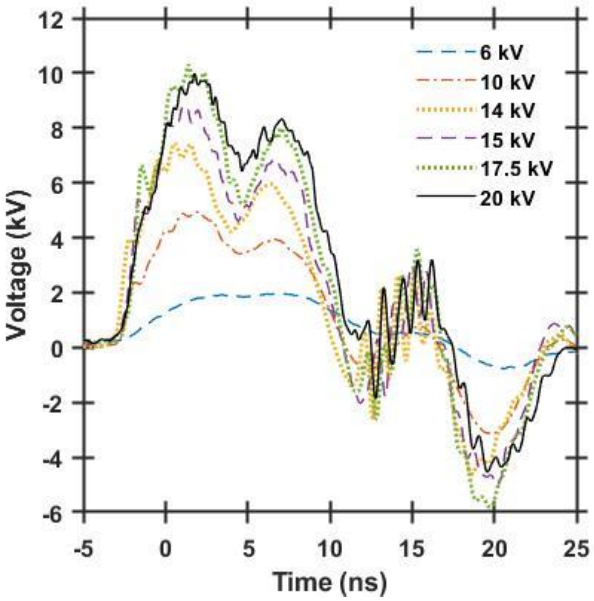

Figure 56. Measured output waveforms for a 10% BST/15% NZF composite-based NLTL used as a PFL.

Figure 57 shows that the oscillations produced on the flat top of the pulse were centered at 1 GHz, agreeing well with simulations. The output power increases with increasing charging voltage except when oscillations are formed on the output. The output power is less than the 25% NZF composite-based NLTL with comparable charging voltage. Figure 57(b) shows that increasing the charging voltage introduces a secondary frequency at 2.27 GHz and shifts the first peak to a higher frequency of 1.17 GHz. The output power at 20 kV is divided between the two main peaks at 1.17 GHz and 2.27 GHz.

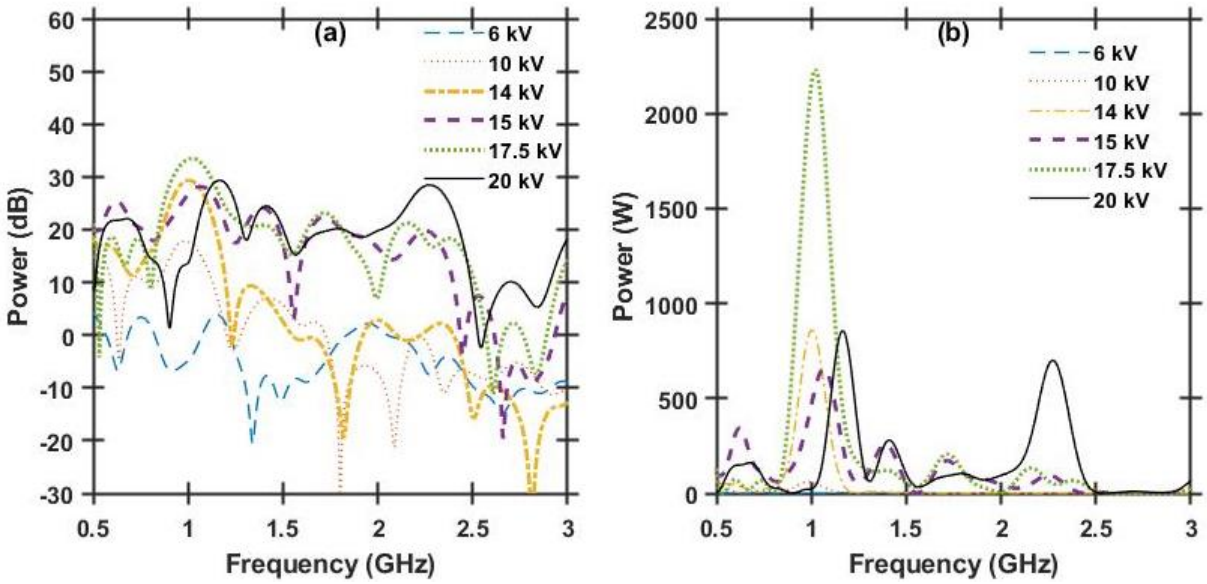

Figure 57. The output spectrum of a 10% BST/15% NZF composite-based NLTL used as a PFL in (a) dB and in (b) linear power during the pulse.

Figure 58 shows the output spectrum for the oscillations after the pulse. The oscillations after the pulse generally increased with charging voltage, exceeding those during the pulse by almost an order of magnitude. A second peak is also generated at 1.42 GHz and 1.36 GHz for a 15 kV and 20 kV charging voltage, respectively. The output power is also distributed between higher frequencies for charging voltages above 14 kV, as shown in Figure 58(a).

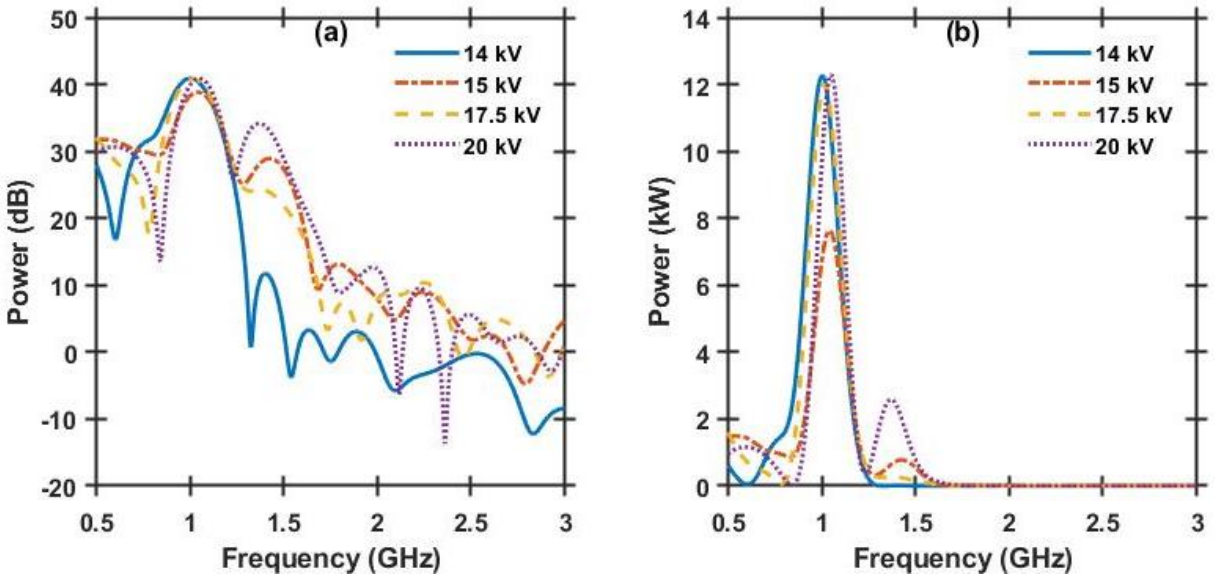

Figure 58. Output spectrum for a 10% BST/15% NZF composite-based NLTL used as a PFL after the initial pulse in (a) dB and (b) linear power, when used as a PFL.

Figure 59 shows the measured output waveforms when testing a 15% BST/10% NZF composite-based NLTL. We charged the NLTL to a higher voltage until breakdown occurred across the outside of the spark gap. Increasing the charging voltage reduced the rise time and produced oscillations. Charging the NLTL to 10 kV or above produced stronger oscillations after the pulse (4.83 kV) than on the flat top of the pulse (0.61 kV). The RF burst on the flat top of the pulse had a duration of 5 ns, while the strong oscillations after the pulse had a duration of 10 ns.

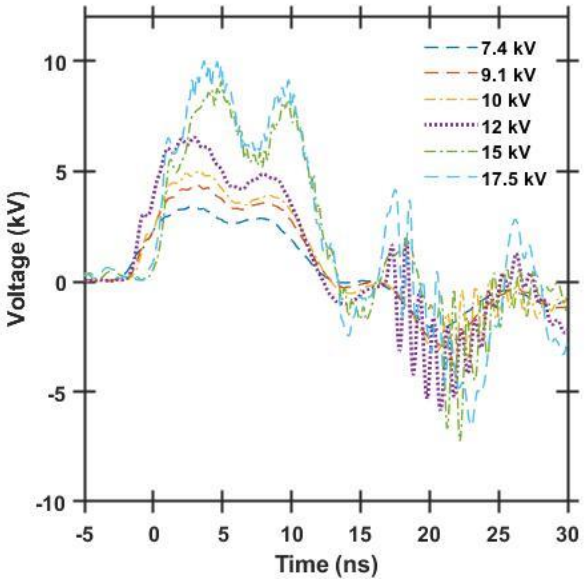

Figure 59. Measured output waveforms for a 15% BST/10% NZF composite-based NLTL used as a PFL.

Figures 60 and 61 show the output spectrum for oscillations during the pulse flat top and at the end of the pulse, respectively. The output power of the oscillations on the pulse flat top increased with increasing charging voltage, producing higher overall output power. The oscillations centered around 1 GHz, in agreement with simulation, until a 15 kV charging voltage where a large peak was produced at 2.28 GHz as seen in the 10 % BST/15% NZF composite NLTL. The amplitude of the oscillations after the pulse flat top exceed those on the flat top or any other composite NLTL tested. Figure 61 shows that the oscillations following the flat top were centered around 1 GHz at all charging voltages and increase with increasing charging voltage until reaching a peak power of ~160 kW at a 17.5 kV charging voltage..

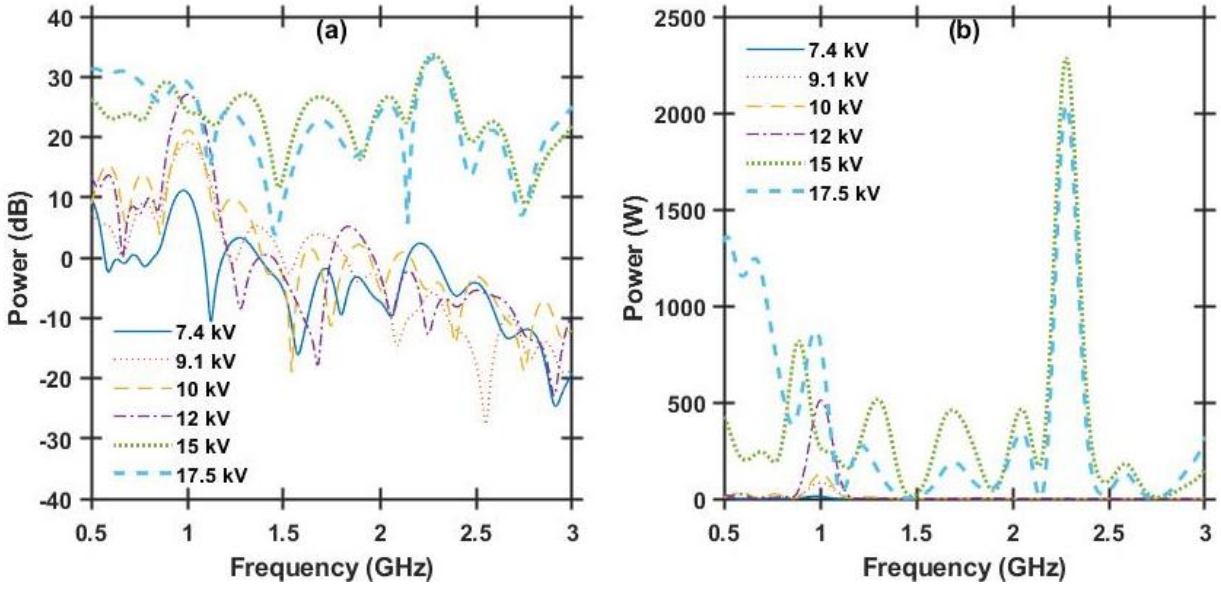

Figure 60. The output spectrum of a 15% BST/10% NZF composite-based NLTL used as a PFL during the pulse in (a) dB and in (b) linear power.

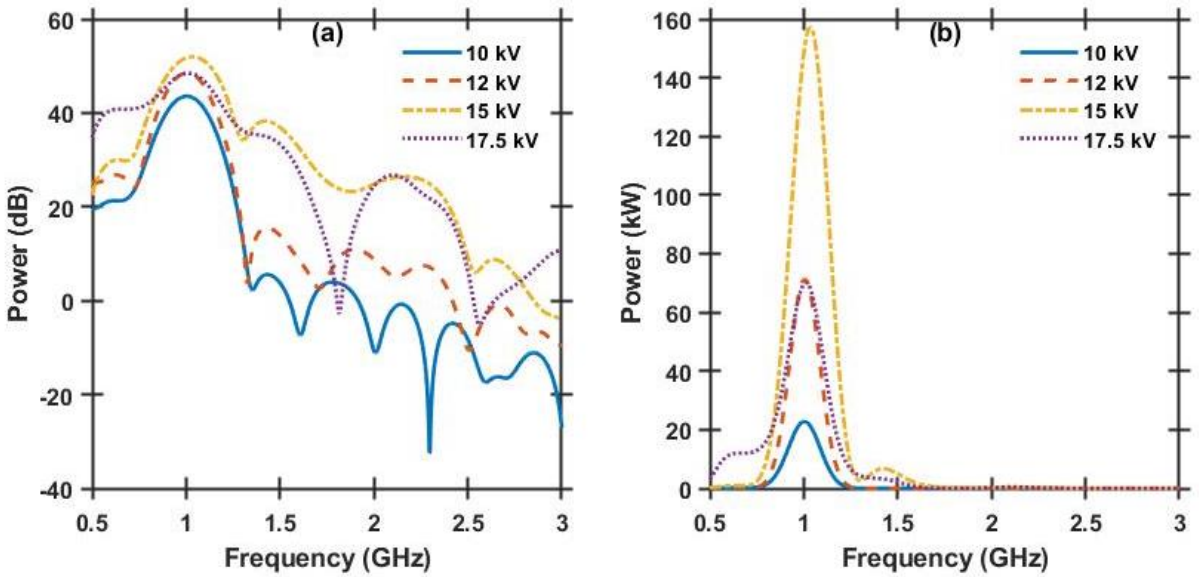

Figure 61. The output spectrum of the oscillations following the applied pulse for a 15% BST/10% NZF composite-based NLTL used as a PFL in (a) dB and in (b) linear power.

5.4 Discussion

This section evaluated the feasibility of using an NLTL consisting of composites with varying volume fractions of BST and NZF as a complete HPM system, encompassing both the modulator and HPM source. Applying a 17.5 kV charging voltage to an NLTL with 15% BST and 10% NZF produced almost 160 kW at a frequency of 1 GHz and duration of 10 ns. The output frequencies matched well with simulations performed using LT Spice. The oscillations produced after the pulse were much higher in amplitude and at the same frequency than the oscillations produced on the flat top of the pulse, except at the highest charging voltages where higher frequency peaks arise during the pulse. None of these experiments used an external magnetic field bias, further reducing the requirement of auxiliary systems required by other HPM systems, even conventional NLTL systems. While other traditional gyromagnetic lines are 1 m in length [109], [123], we show here that a 20 in line can produce HPM bursts at longer durations. The implementation of a composite hybrid NLTL provides impedance and pulse duration tunability allowing for better matching to antenna designs.

The RF burst duration of 10 ns is longer than the outputs from most traditional gyromagnetic NLTLs by 2 [123] to 7 ns [109]. The increased RF burst duration provides an increase in energy on target as well as reduces the required repetition rate needed to apply the same

energy as a conventional vacuum HPM source. While the output power is orders of magnitude lower than the MW class NLTLs, the composites can withstand electric fields up to 401.20±150.73 kV/cm [181]. The design presented here uses DC charging voltage, significantly simplifying input connector design compared to traditional NLTLs driven by a separate power modulator. Increasing charging voltage greatly increase the output power of the NLTLs, making MW output power possible.

As the charging voltage increases, the oscillations on the flat top of the pulse continue to grow and begin to generate higher frequencies. The increase in oscillations amplitude after the pulse for the 10% BST/15% NZF NLTL compared to the 15% BST/ 10% NZF NTLs could be due to the increased insulation between the NZF inclusions provided by the higher volume loading of BST. We hypothesize that magnetic losses decrease with increasing BST volume fraction due to the reduction in eddy currents in the material due to this insulation between NZF inclusions. The reduced magnetic loss would reduce the dampening of the magnetic moment precession and possibly allow large oscillations to occur that did not for higher NZF volume fractions.

One important effort for future work is to design a high voltage input connection to prevent breakdown and enable a much higher charging voltage. Additionally, using a triggered spark gap switch would provide greater control over the repetition rate and charging voltage. Constructing 50 Ω NLTLs will permit increasing the distance between the inner and outer conductors, facilitating higher charging voltages. The higher impedance lines will also produce longer duration pulses due to the increased inductance and capacitance of the line, providing the possibility of generating longer RF bursts..

6. CONCLUSION

The research has shown that a composite with nonlinear dielectric and magnetic properties is suitable for generating HPM pulses. The overall length of the NLTL device has been reduced by a factor of 2. The weight of the devices has been decreased by removing portions of the NZF material up to 75%. While the power produced thus far has not increased from conventional NLTLs, the breakdown threshold of the materials provides a hypothesis that higher powers are capable of being achieved with device sizes comparable to other NLTL devices. The critical component that would allow higher voltages is the connection to the device, which is significantly simplified by implementing the NLTL as a PFL due to the lack of size constraints resulting from high frequency pulses.

Varying the volume fractions of BST and/or NZF the permittivity of PDMS can be increased from 2.7 to 7.45 ± 0.33 with a 25% volume fraction of BST and increase the permeability of PDMS from 1 to 1.43 ± 0.04 with a 25% volume fraction of NZF at 1 GHz. The permittivity of the composites stays relatively constant over a frequency span of 1 to 4 GHz while the permeability exponentially decreases as the frequency increases. The dielectric and magnetic loss tangents also increase as the volume fractions of the inclusions are increased. However, when BST is added to composites with NZF the magnetic loss tangent decreases. The decrease in magnetic loss tangent is due to the insulation of the NZF particles that eliminates the eddy currents between the particles, which are the main source of magnetic loss in ferrites.

The breakdown voltage of composites with volume fractions of NZF exponentially decreases as the volume fraction increase where composites with BST have a relatively constant breakdown voltage. However, composites that have both BST and NZF inclusions see a much higher breakdown strength when at least 10% BST is incorporated into a composite with NZF. The breakdown strength for composites with 15% NZF increases from 49.90 ± 8.64 to 401.20 ± 150.73 kV/cm. This strong increase allows for the implementation into HPM systems.

When implementing the composite based NLTL into as a HPM source the choice of modulator is critical. The rise time of the driving pulse is also pivotal when the desired result is the production of RF. A rise time < 10 ns is generally shown to be sufficient when a line has a length of 1 m and potentially a shorter length with the application of a external magnetic field bias. Chapter 4 shows that a Blumlein modulator is insufficient to produce RF in the NLTL, even with

a rise time of 1.5 ns and a strong external magnetic field bias. While additional frequencies are produced by the composite lines that correspond to output frequencies simulated by driving the NLTL with a PFN, the power in these frequencies is very low and the clear oscillatory nature of the NLTL output pulse is not seen. Simulations indicate that this occurs because the Blumlein generator applied a pulse on both the center and outer conductor, with the potential difference being a square wave. Though the potential difference produces a square wave, the increased potential difference does not allow for a clear precession of magnetic moments in the composite. The RF production of the NLTLs results from the gyromagnetic precession of the magnetic moments in the NZF. The pulse durations, 10 ns, is too short for the motion of the polarization vector in the BST to oscillate between stable positions due to the inertia of the offset atom. However, the BST does insulate the NZF particles from one another, which prevents eddy currents and allows for a higher frequency output peak than the purely NZF composite. When selecting a modulator to drive an NLTL, a fast rise time of < 10 ns with the pulse applied directly to the center conductor and the outer conductor tied to ground is desired. When selecting a modulator to drive the composite lines, one should increase the pulse duration to utilize the oscillatory effect of the BST.

The coaxial nature of the composite NLTL allows for the implementation as both a PFN and HPM source in a single package. The NLTL can be charged to a set DC voltage and then discharged through a pressurized spark gap switch. As the charging voltage increased the rise time sharpened and produced high frequency oscillations that continued to grow in amplitude as the charging voltage increased. This greatly reduces the size of the overall HPM system by eliminating the high voltage modulator.

Future work will entail driving the composite NLTLs with other modulators, such as a PFN and inductive adder. These modulators will apply a square pulse to the center conductor of the NLTL while the outer conductor is at ground potential. The impedance of these modulators will vary between 25 and 50 Ω, which will also greatly increase the power handling capability of the lines due to increased spacing between the inner and outer conductor. Additionally, evaluation of the nonlinear magnetic properties of the composite at microwave fields indicates that the optimal bias field should be ~ 100 kV/m. The nonlinear dielectric measurements are also being designed and the test fixtures will be used to measure the permittivity of the composites while applying an

external electric field bias. Connectors will also be designed and tested to pursue the use of the NLTL as a HPM system allowing for higher voltage charging and power output.

REFERENCES

[1] J.-W. B. Bragg, J. C. Dickens, and A. A. Neuber, "Ferrimagnetic nonlinear transmission lines as high-power microwave sources," *IEEE Trans. Plasma Sci.*, vol. 41, no. 1, pp. 232–237, Jan. 2013.

[2] J. O. Rossi, L. P. Silva, J. J. Barroso, F. S. Yamasaki, and E. Schamiloglu, "Overview of RF generation using nonlinear transmission lines," in *2015 IEEE Pulsed Power Conference (PPC)*, 2015, vol. 2015-Octob, pp. 1–6.

[3] J. Gaudet, E. Schamiloglu, J. O. Rossi, C. J. Buchenauer, and C. Frost, "Nonlinear transmission lines for high power microwave applications - A survey," *Proc. 2008 IEEE Int. Power Modul. High Volt. Conf. PMHVC*, pp. 131–138, 2008.

[4] O. S. F. Zucker, P. K. L. Yu, and Y.-M. Sheu, "GaN switches in pulsed power: A comparative study," *IEEE Trans. Plasma Sci.*, vol. 42, no. 5, pp. 1295–1303, May 2014.

[5] T. J. Flack, B. N. Pushpakaran, and S. B. Bayne, "GaN technology for power electronic applications: A review," *J. Electron. Mater.*, vol. 45, no. 6, pp. 2673–2682, 2016.

[6] X. She, A. Q. Huang, O. Lucia, and B. Ozpineci, "Review of silicon carbide power devices and their applications," *IEEE Trans. Ind. Electron.*, vol. 64, no. 10, pp. 8193–8205, 2017.

[7] S. Ashby *et al.*, "High peak and average power with an L-band relativistic magnetron on CLIA," *IEEE Trans. Plasma Sci.*, vol. 20, no. 3, pp. 344–350, Jun. 1992.

[8] M. R. Ulmasculov *et al.*, "Gyromagnetic nonlinear transmission line generator of high voltage pulses modulated at 4 GHz frequency with 1000 Hz pulse repetition rate," *J. Phys. Conf. Ser.*, vol. 830, no. 1, May 2017, Art. no. 012027.

[9] N. S. Kuek, A. C. Liew, E. Schamiloglu, and J. O. Rossi, "Pulsed RF oscillations on a nonlinear capacitive transmission line," *IEEE Trans. Dielectr. Electr. Insul.*, vol. 20, no. 4, pp. 1129–1135, Aug. 2013.

[10] J. Choi and C. Seo, "Broadband VCO using electronically controlled metamaterial transmission line based on varactor-loaded split-ring resonator," *Microw. Opt. Technol. Lett.*, vol. 50, no. 4, pp. 1078–1082, Apr. 2008.

[11] I. V. Romanchenko, V. V. Rostov, V. P. Gubanov, A. S. Stepchenko, A. V. Gunin, and I. K. Kurkan, "Repetitive sub-gigawatt rf source based on gyromagnetic nonlinear transmission line," *Rev. Sci. Instrum.*, vol. 83, no. 7, Jul. 2012, Art. no. 074705.

[12] R. Hirota and K. Suzuki, "Theoretical and experimental studies of lattice solitons in nonlinear lumped networks," *Proc. IEEE,* vol. 61, no. 10, pp. 1483–1491, 1973.

[13] M. M. Turner, G. Branch, and P. W. Smith, "Methods of theoretical analysis and computer modeling of the shaping of electrical pulses by nonlinear transmission lines and lumped-element delay lines," *IEEE Trans. Electron Devices*, vol. 38, no. 4, pp. 810–816, Apr. 1991.

[14] E. Afshari and A. Hajimiri, "Nonlinear transmission lines for pulse shaping in silicon," *IEEE J. Solid-State Circuits,* vol. 40, no. 3, pp. 744–752, Mar. 2005.

[15] N. J. Zabusky and M. D. Kruskal, "Interaction of 'solitons' in a collisionless plasma and the recurrence of initial states," *Phys. Rev. Lett.*, vol. 15, no. 6, pp. 240–243, Aug. 1965.

[16] M. Tokuyama and H. Ohtagaki, "Chaos in a series circuit with a nonlinear capacitor and a nonlinear inductor," *Electr. Eng. Japan*, vol. 150, no. 2, pp. 35–42, Jan. 2005.

[17] E. Afshari, H. S. Bhat, A. Hajimiri, and J. E. Marsden, "Extremely wideband signal shaping using one- and two-dimensional nonuniform nonlinear transmission lines," *J. Appl. Phys.*, vol. 99, no. 5, Mar. 2006, Art. no. 054901.

[18] J. D. C. Darling and P. W. Smith, "High-Power pulsed RF extraction from nonlinear lumped element transmission lines," *IEEE Trans. Plasma Sci.,* vol. 36, no. 5, pp. 2598–2603, Oct. 2008.

[19] Z. Chen, D. R. Hedgepeth, and X. Tan, "Nonlinear capacitance of ionic polymer-metal composites," *Proc. SPIE,* vol. 7287, no. 517, 2009, Art. no. 728715.

[20] N. S. Kuek, A. C. Liew, E. Schamiloglu, and J. O. Rossi, "Oscillating pulse generator based on a nonlinear inductive line," *IEEE Trans. Plasma Sci.*, vol. 41, no. 10, pp. 2619–2624, Oct. 2013.

[21] N. S. Kuek, A. C. Liew, E. Schamiloglu, and J. O. Rossi, "RF pulse generator based on a nonlinear hybrid line," *IEEE Trans. Plasma Sci.*, vol. 42, no. 10, pp. 3268–3273, Oct. 2014.

[22] N. S. Kuek, A. C. Liew, E. Schamiloglu, and J. O. Rossi, "Circuit modeling of nonlinear lumped element transmission lines including hybrid lines," *IEEE Trans. Plasma Sci.,* vol. 40, no. 10, pp. 2523–2534, Oct. 2012.

[23] A. Steinbrecher and T. Stykel, "Model order reduction of nonlinear circuit equations," *Int. J. Circuit Theory Appl.,* vol. 41, no. 12, pp. 1226–1247, Dec. 2013.

[24] B. Nouri, M. S. Nakhla, and R. Achar, "Efficient simulation of nonlinear transmission lines via model-order reduction," *IEEE Trans. Microw. Theory Tech.,* wol. 65, no. 3, pp. 673-683, Mar. 2017.

[25] E. Stenglein and M. Albach, "Analytical calculation method for the non-linear characteristic of ferrite-cored inductors with stepped air gap," *Electr. Eng.,* vol. 99, no. 1, pp. 421–429, Mar. 2017.

[26] H. Fatoorehchi, H. Abolghasemi, and R. Zarghami, "Analytical approximate solutions for a general nonlinear resistor–nonlinear capacitor circuit model," *Appl. Math. Model.,* vol. 39, no. 19, pp. 6021–6031, Oct. 2015.

[27] F. S. Yamasaki, L. P. S. Neto, J. O. Rossi, and J. J. Barroso, "Soliton generation using nonlinear transmission lines," *IEEE Trans. Plasma Sci.*, vol. 42, no. 11, pp. 3471–3477, Nov. 2014.

[28] S. Y. Elnaggar and G. N. Milford, "Description and stability analysis of nonlinear transmission line type metamaterials using nonlinear dynamics theory," *J. Appl. Phys.,* vol. 121, no. 12, Mar. 2017, Art. no. 124902.

[29] M. Samizadeh Nikoo, S. M.-A. Hashemi, and F. Farzaneh, "Theory of RF pulse generation through nonlinear transmission lines," *IEEE Trans. Microw. Theory Tech.,* vol. 66, no. 7, pp. 3234–3244, Jul. 2018.

[30] A. S. Kyuregyan, "Large-amplitude shock electromagnetic wave in a nonlinear transmission line based on a distributed semiconductor diode," *Semiconductors,* vol. 53, no. 4, pp. 511–518, Apr. 2019.

[31] N. A. Akem, A. M. Dikande, and B. Z. Essimbi, "Leapfrogging of electrical solitons in coupled nonlinear transmission lines: effect of an imperfect varactor," *SN Appl. Sci.,* vol. 2, 2020, Art. no. 21.

[32] N. Seddon, C. R. Spikings, and J. E. Dolan, "RF pulse formation in nonlinear transmission lines," in *2007 16th IEEE International Pulsed Power Conference,* 2007, vol. 1, pp. 678–681.

[33] D. M. French, B. W. Hoff, S. Heidger, and D. Shiffler, "Dielectric nonlinear transmission line," in *2011 IEEE Pulsed Power Conference,* 2011, pp. 341–345.

[34] L. P. S. Neto, J. O. Rossi, J. J. Barroso, and A. R. Silva, "Characterization of ceramic dielectrics for sub-GHz applications in nonlinear transmission lines," *IEEE Trans. Plasma Sci.*, vol. 42, no. 10, pp. 3274–3282, Oct. 2014.

[35] L. P. Silva Neto, J. O. Rossi, J. J. Barroso, and E. Schamiloglu, "High-power RF generation from nonlinear transmission lines with barium titanate ceramic capacitors," *IEEE Trans. Plasma Sci.*, vol. 44, no. 12, pp. 3424–3431, Dec. 2016.

[36] P. V. Priputnev, I. V. Romanchenko, V. V. Rostov, O. B. Kovalchuk, and V. V. Barmin, "Nanosecond front dynamics and RF oscillation generation in a transmission line with nonlinear capacitors," in *2018 20th International Symposium on High-Current Electronics (ISHCE)*, 2018, pp. 85–88.

[37] L. R. Raimundi, J. O. Rossi, E. G. L. Rangel, L. C. Silva, E. Schamiloglu, and L. P. S. Neto, "RF generation at 200 MHz using a SiC Schottky diode lumped NLTL," in *2018 IEEE International Power Modulator and High Voltage Conference (IPMHVC)*, 2018, pp. 473–476.

[38] L. R. Raimundi, J. O. Rossi, E. G. L. Rangel, L. C. Silva, and E. Schamiloglu, "High-voltage capacitive nonlinear transmission lines for RF generation based on silicon carbide Schottky diodes," *IEEE Trans. Plasma Sci.* vol. 47, no. 1, pp. 566-573, Jan. 2019.

[39] L. C. Silva, J. O. Rossi, E. G. L. Rangel, L. R. Raimundi, and E. Schamiloglu, "Study of pulsed RF signal extraction and irradiation from a capacitive nonlinear transmission line," *Int. J. Adv. Res. Sci. Eng. Technol.*, vol. 5, no. 10, pp 121-133, Oct. 2018.

[40] L.P. S. Neto, H. M. Moraes, J. O. Rossi, J. J. Barroso, and E. G. L. Rangel, "Increasing the voltage modulation depth of the RF produced by NLTL," *IEEE Trans Plasma Sci.* 2020.

[41] E. G. L. Rangel, J. J. Barroso, J. O. Rossi, F. S. Yamasaki, L. P. S. Neto, and E. Schamiloglu, "Influence of input pulse shape on RF generation in nonlinear transmission lines," *IEEE Trans. Plasma Sci.*, Vol. 44, no. 10, pp. 2258-2267, 2016.

[42] Y. Wang, L. Lang, C. H. Lee, B. Zhang, and Y. D. Chong, "Topologically enhanced harmonic generation in a nonlinear transmission line metamaterial," *Nat. Commun*, vol. 10, 2019, Art. no. 1102.

[43] M. Adnan, and E. Afshari, "Efficient microwave and millimeter-wave frequency multipliers using nonlinear transmission lines in CMOS technology," *IEEE Trans. Microw. Theory Tech.*, vol. 63, no. 9, pp. 2889-2896, Sep. 2015.

[44] J. B. Pendry, A. J. Holden, D. J. Robbins, and W. J. Stewart, “Magnetism from conductors and enhanced nonlinear phenomena,” *IEEE Trans. Microw. Theory Tech.*, vol. 47, no. 11, pp. 2075–2084, 1999.

[45] J. B. Pendry, “Controlling electromagnetic fields,” *Science*, vol. 312, no. 5781, pp. 1780–1782, Jun. 2006.

[46] R. Marques, F. Mesa, J. Martel, and F. Medina, “Comparative analysis of edge- and broadside-coupled split ring resonators for metamaterial design - theory and experiments,” *IEEE Trans. Antennas Propag.*, vol. 51, no. 10, pp. 2572–2581, Oct. 2003.

[47] H. Nornikman, B. H. Ahmad, M. Z. A. Abdul Aziz, M. F. bin A. Malek, H. Imran, and A. R. Othman, “Study and simulation of an edge couple split ring resonator (EC-SRR) on truncated pyramidal microwave absorber,” *Prog. Electromagn. Res.*, vol. 127, no. March, pp. 319–334, 2012.

[48] F. Martín, J. Bonache, F. Falcone, M. Sorolla, and R. Marqués, “Split ring resonator-based left-handed coplanar waveguide,” *Appl. Phys. Lett.*, vol. 83, no. 22, pp. 4652–4654, Dec. 2003.

[49] V. G. Veselago, “The electrodynamics of substances with simultaneously negative values of ε and μ,” *Sov. Phys. Uspekhi*, vol. 10, no. 4, pp. 509–514, Apr. 1968.

[50] W. Tang, G. Goussetis, N. J. G. Fonseca, H. Legay, E. Saenz, and P. de Maagt, “Coupled split-ring resonator circular polarization selective surface,” *IEEE Trans. Antennas Propag.*, vol. 65, no. 9, pp. 4664–4675, Sep. 2017.

[51] A. Rigi-Tamandani, J. Ahmadi-Shokouh, and S. Tavakoli, “Wideband planar split ring resonator based metamaterials,” *Prog. Electromagn. Res. M*, vol. 28 , pp. 115–128, Jan. 2013.

[52] T. J. Cui, D. Smith, and R. Liu, *Metamaterials Theory, Design, and Applications*. Boston, MA: Springer US, 2010.

[53] M. Shamonin, E. Shamonina, V. Kalinin, and L. Solymar, “Resonant frequencies of a split-ring resonator: Analytical solutions and numerical simulations,” *Microw. Opt. Technol. Lett.*, vol. 44, no. 2, pp. 133–136, Jan. 2005.

[54] B. Sauviac, C. R. Simovski, and S. A. Tretyakov, “Double split-ring resonators: analytical modeling and numerical simulations,” *Electromagnetics*, vol. 24, no. 5, pp. 317–338, Jan. 2004.

[55] O. Sydoruk, E. Tatartschuk, E. Shamonina, and L. Solymar, "Analytical formulation for the resonant frequency of split rings," *J. Appl. Phys.*, vol. 105, no. 1, Jan. 2009, Art. no. 014903.

[56] J. D. Baena *et al.*, "Equivalent-circuit models for split-ring resonators and complementary split-ring resonators coupled to planar transmission lines," *IEEE Trans. Microw. Theory Tech.*, vol. 53, no. 4, pp. 1451–1461, Apr. 2005.

[57] F. Qureshi, M. A. Antoniades, and G. V. Eleftheriades, "A compact and low-profile metamaterial ring antenna with vertical polarization," *IEEE Antennas Wirel. Propag. Lett.*, vol. 4, no. 1, pp. 333–336, 2005.

[58] M. A. Rahman, M. R. I. Faruque, and M. T. Islam, "Circularly split-ring-resonator-based frequency-reconfigurable antenna," *Appl. Phys. A*, vol. 123, no. 1, Jan. 2017, Art. no. 110.

[59] S. I. Maslovski, P. M. T. Ikonen, I. Kolmakov, S. A. Tretyakov, and M. Kaunisto, "Artificial magnetic materials based on the new magnetic particle: metasolenoid," *Prog. Electromagn. Res.*, vol. 54, pp. 61–81, 2005.

[60] R. Liu, T. J. Cui, D. Huang, B. Zhao, and D. R. Smith, "Description and explanation of electromagnetic behaviors in artificial metamaterials based on effective medium theory," *Phys. Rev. E*, vol. 76, no. 2, p. 026606, Aug. 2007.

[61] F. Bilotti, A. Toscano, L. Vegni, K. Aydin, K. B. Alici, and E. Ozbay, "Equivalent-circuit models for the design of metamaterials based on artificial magnetic inclusions," *IEEE Trans. Microw. Theory Tech.*, vol. 55, no. 12, pp. 2865–2873, Dec. 2007.

[62] A. Kabiri, L. Yousefi, and O. M. Ramahi, "On the fundamental limitations of artificial magnetic materials," *IEEE Trans. Antennas Propag.*, vol. 58, no. 7, pp. 2345–2353, Jul. 2010.

[63] E. Poutrina, D. Huang, and D. R. Smith, "Analysis of nonlinear electromagnetic metamaterials," *New J. Phys.*, vol. 12, no. 9, Sep. 2010, Art. no. 093010.

[64] K. Payandehjoo and R. Abhari, "Suppression of unwanted harmonics using integrated complementary split-ring resonators in nonlinear transmission line frequency multipliers," *IEEE Trans. Microw. Theory Tech.*, vol. 56, no. 4, pp. 931–941, Apr. 2008.

[65] Z. Duan, J. S. Hummelt, M. A. Shapiro, and R. J. Temkin, "Sub-wavelength waveguide loaded by a complementary electric metamaterial for vacuum electron devices," *Phys. Plasmas*, vol. 21, no. 10, Oct. 2014, Art. no. 103301.

[66] D. M. French, D. Shiffler, and K. Cartwright, “Electron beam coupling to a metamaterial structure,” *Phys. Plasmas*, vol. 20, no. 8, Aug. 2013, Art. no. 083116.

[67] D. Shiffler, R. Seviour, E. Luchinskaya, E. Stranford, W. Tang, and D. French, “Study of split-ring resonators as a metamaterial for high-power microwave power transmission and the role of defects,” *IEEE Trans. Plasma Sci.*, vol. 41, no. 6, pp. 1679–1685, Jun. 2013.

[68] J. A. Bossard *et al.*, “Mitigating field enhancement in metasurfaces and metamaterials for high-power microwave applications,” *IEEE Trans. Antennas Propag.*, vol. 64, no. 12, pp. 5309–5319, Dec. 2016.

[69] D. R. Smith, W. J. Padilla, D. C. Vier, S. C. Nemat-Nasser, and S. Schultz, “Composite medium with simultaneously negative permeability and permittivity,” *Phys. Rev. Lett.*, vol. 84, no. 18, pp. 4184–4187, May 2000.

[70] D. R. Smith, S. Schultz, P. Markoš, and C. M. Soukoulis, “Determination of effective permittivity and permeability of metamaterials from reflection and transmission coefficients,” *Phys. Rev. B*, vol. 65, no. 19, Apr. 2002, Art. no. 195104.

[71] A. Rigi-Tamandani, J. Ahmadi-Shokouh, and S. Tavakoli, “Wideband planar split ring resonator based metamaterials,” *Prog. Electromagn. Res. M*, vol. 28, pp. 115–128, Dec. 2013.

[72] D. Bensafieddine, F. Djerfaf, F. Chouireb, and D. Vincent, “Design of tunable microwave transmission lines using metamaterial cells,” *Appl. Phys. A*, vol. 123, no. 4, Apr. 2017, Art. no. 248.

[73] K. Aydin and E. Ozbay, “Capacitor-loaded split ring resonators as tunable metamaterial components,” *J. Appl. Phys.*, vol. 101, no. 2, 2007.

[74] K. Aydin *et al.*, “Split-ring-resonator-coupled enhanced transmission through a single subwavelength aperture,” *Phys. Rev. Lett.*, vol. 102, no. 1, Jan. 2009, Art. no. 013904.

[75] T. Okamoto, T. Otsuka, S. Sato, T. Fukuta, and M. Haraguchi, “Dependence of LC resonance wavelength on size of silver split-ring resonator fabricated by nanosphere lithography,” *Opt. Express*, vol. 20, no. 21, Oct. 2012, Art. no. 24059.

[76] L.-C. Tsai and W.-J. Chen, “A UWB antenna with bandnotched filters using slot-type split ring resonators,” *Microw. Opt. Technol. Lett.*, vol. 58, no. 11, pp. 2595–2598, 2016.

[77] R. Seviour, Y. S. Tan, and A. Hopper, “Effects of high power on microwave metamaterials,” in *2014 8th International Congress on Advanced Electromagnetic Materials in Microwaves and Optics*, 2014, no. August, pp. 142–144.

[78] E. G. L. Rangel, J. O. Rossi, J. J. Barroso, F. S. Yamasaki, and E. Schamiloglu, “Practical constraints on nonlinear transmission lines for RF generation,” *IEEE Trans. Plasma Sci.*, vol. 47, no. 1, pp. 1000 – 1016, Jan. 2019.

[79] E. M. Gyorgy, “Rotational model of flux reversal in square loop ferrites,” *J. Appl. Phys.*, vol. 28, no. 9, pp. 1011–1015, Sep. 1957.

[80] H. C. Hsieh, “Coupled mode theory in a lossy, nonlinear transmission line system,” *J. Appl. Phys.*, vol. 62, no. 5, pp. 2095–2102, Sep. 1987.

[81] E. Sawado, M. Taki, and S. Kiliu, “Nonlinear magnetic lattice and the modified Korteweg-de Vries equation,” *Phys. Rev. B*, vol. 38, no. 16, pp. 11911–11914, Dec. 1988.

[82] H. Ikezi, S. S. Wojtowicz, R. E. Waltz, J. S. DeGrassie, and D. R. Baker, “High-power soliton generation at microwave frequencies,” *J. Appl. Phys.*, vol. 64, no. 6, pp. 3277–3281, Sep. 1988.

[83] R. Luebbers, K. Kumagai, S. Adachi, and T. Uno, “FDTD calculation of transient pulse propagation through a nonlinear magnetic sheet,” *IEEE Trans. Electromagn. Compat.*, vol. 35, no. 1, pp. 90–94, 1993.

[84] M. Oriel, C. U. Brown, “High voltage soliton production in nonlinear transmission lines and other pulsed power applications,” Oxford University, 1997.

[85] F. Crowne, “Modeling and simulation of nonlinear dynamics,” Adelphi, MD, 2010.

[86] E. Gluskin, “A nonlinear resistor and nonlinear inductor using a nonlinear capacitor,” *J. Franklin Inst.*, vol. 336, no. 7, pp. 1035–1047, Sep. 1999.

[87] L. Gao, X. Yang, J. Hu, and J. He, “ZnO microvaristors doped polymer composites with electrical field dependent nonlinear conductive and dielectric characteristics,” *Mater. Lett.*, vol. 171, pp. 1–4, May 2016.

[88] V. G. Harris, “Modern microwave ferrites,” *IEEE Trans. Magn.*, vol. 48, no. 3, pp. 1075–1104, Mar. 2012.

[89] F. Qin and H.-X. Peng, “Ferromagnetic microwires enabled multifunctional composite materials,” *Prog. Mater. Sci.*, vol. 58, no. 2, pp. 183–259, Mar. 2013.

[90] G. Zhao, R. P. Joshi, S. Rogers, E. Schamiloglu, and H. P. Hjalmarson, "Simulation studies for nonlinear-transmission-line based ultrafast rise times and waveform shaping for pulsed-power applications," *IEEE Trans. Plasma Sci.*, vol. 36, no. 5, pp. 2618–2625, Oct. 2008.

[91] H. A. Ávila, M. M. Reboredo, R. Parra, and M. S. Castro, "Dielectric permittivity calculation of composites based on electrospun barium titanate fibers," *Mater. Res. Express*, vol. 2, no. 4, Apr. 2015, Art. no. 045302.

[92] K. A. O'Connor and R. D. Curry, "Three-dimensional electromagnetic modeling of composite dielectric materials," in *2011 IEEE Pulsed Power Conference*, 2011, pp. 274–279.

[93] A. L. Garner, G. J. Parker, and D. L. Simone, "A semi-empirical approach for predicting the performance of multiphase composites at microwave frequencies," *IEEE Trans. Dielectr. Electr. Insul.*, vol. 23, pp. 1126–1134, 2015.

[94] A. L. Garner, G. J. Parker, and D. L. Simone, "Accounting for conducting inclusion permeability in the microwave regime in a modified generalized effective medium theory," *IEEE Trans. Dielectr. Electr. Insul.*, vol. 22, no. 1, pp. 2064–2072, 2015.

[95] M. Lapine, I. V. Shadrivov, and Y. S. Kivshar, "Colloquium: nonlinear metamaterials," *Rev. Mod. Phys.*, vol. 86, no. 3, pp. 1093–1123, Sep. 2014.

[96] M. Y. Koledintseva, R. E. DuBroff, R. W. Schwartz, and J. L. Drewniak, "Double statistical distribution of conductivity and aspect ratio of inclusions in dielectric mixtures at microwave frequencies," *Prog. Electromagn. Res.*, vol. 77, pp. 193–214, 2007.

[97] B. A. Slovick, Z. G. Yu, and S. Krishnamurthy, "Generalized effective-medium theory for metamaterials," *Phys. Rev. B*, vol. 89, no. 15, Apr. 2014, Art. no. 155118.

[98] Z. Szabo and J. Fuzi, "Equivalence of magnetic metamaterials and composites in the view of effective medium theories," *IEEE Trans. Magn.*, vol. 50, no. 4, pp. 1–4, Apr. 2014.

[99] E. Kengne and W. M. Liu, "Exact solutions of the derivative nonlinear Schrödinger equation for a nonlinear transmission line," *Phys. Rev. E*, vol. 73, no. 2, Feb. 2006, Art. no. 026603.

[100] I. V. Romanchenko and V. V. Rostov, "Energy levels of oscillations in a nonlinear transmission line filled with saturated ferrite," *Tech. Phys.*, vol. 55, no. 7, pp. 1024–1027, Jul. 2010.

[101] F. S. Yamasaki, E. Schamiloglu, J. O. Rossi, and J. J. Barroso, "Simulation studies of distributed nonlinear gyromagnetic lines based on LC lumped model," *IEEE Trans. Plasma Sci.*, vol. 44, no. 10, pp. 2232–2239, Oct. 2016.

[102] S. Y. Karelin, V. B. Krasovitsky, I. I. Magda, V. S. Mukhin, and V. G. Sinitsin, "Radio frequency oscillations in gyrotropic nonlinear transmission lines," *Plasma*, vol. 2, no. 2, pp. 258–271, Jun. 2019.

[103] I. G. Kataev, *Electromagnetic Shock Waves*. London: Iliffe Books Ltd, 1966.

[104] G. Branch and P. W. Smith, "Shock waves in transmission lines with nonlinear dielectrics," in *IEE Colloquium on Pulsed Power*, 1993, pp. 7/1-7/3.

[105] S. N. Rukin, "Pulsed power technology based on semiconductor opening switches: A review," *Rev. Sci. Instrum.*, vol. 91, no. 1, Jan. 2020, Art. no. 011501.

[106] A. I. Gusev, M. S. Pedos, A. V. Ponomarev, S. N. Rukin, S. P. Timoshenkov, and S. N. Tsyranov, "A 30 GW subnanosecond solid-state pulsed power system based on generator with semiconductor opening switch and gyromagnetic nonlinear transmission lines," *Rev. Sci. Instrum.*, vol. 89, no. 9, Sep. 2018, Art. no. 094703.

[107] W. Tie *et al.*, "Optimized analysis of sharpening characteristics of a compact RF pulse source based on a gyro-magnetic nonlinear transmission line for ultrawideband electromagnetic pulse application," *Plasma Sci. Technol.*, vol. 21, no. 9, Sep. 2019, Art. no. 095503.

[108] M. R. Ulmaskulov, S. A. Shunailov, K. A. Sharypov, and M. I. Yalandin, "Multistage converter of high-voltage subnanosecond pulses based on nonlinear transmission lines," *J. Appl. Phys.*, vol. 126, no. 8, Aug. 2019, Art. no. 084504.

[109] J.-W. B. Bragg, W. W. Sullivan, D. Mauch, A. A. Neuber, and J. C. Dickens, "All solid-state high power microwave source with high repetition frequency," *Rev. Sci. Instrum.*, vol. 84, no. 5, May 2013, Art. no. 054703.

[110] J.-W. B. Bragg, J. C. Dickens, and A. A. Neuber, "Material selection considerations for coaxial, ferrimagnetic-based nonlinear transmission lines," *J. Appl. Phys.*, vol. 113, no. 6, Feb. 2013, Art. no. 064904.

[111] D. M. French and B. W. Hoff, "Spatially dispersive ferrite nonlinear transmission line with axial bias," *IEEE Trans. Plasma Sci.*, vol. 42, no. 10, pp. 3387–3390, Oct. 2014.

[112] D. V. Reale *et al.*, "Bias-field controlled phasing and power combination of gyromagnetic nonlinear transmission lines," *Rev. Sci. Instrum.*, vol. 85, no. 5, May 2014, Art. no. 054706.

[113] J. M. Johnson *et al.*, "Material selection of a ferrimagnetic loaded coaxial delay line for phasing gyromagnetic nonlinear transmission lines," *Rev. Sci. Instrum.*, vol. 86, no. 8, Aug. 2015, Art. no. 084702.

[114] I. V. Romanchenko, V. V. Rostov, A. V. Gunin, and V. Y. Konev, "High power microwave beam steering based on gyromagnetic nonlinear transmission lines," *J. Appl. Phys.*, vol. 117, no. 21, Jun. 2015, Art. no. 214907.

[115] J. M. Johnson *et al.*, "Characteristics of a four element gyromagnetic nonlinear transmission line array high power microwave source," *Rev. Sci. Instrum.*, vol. 87, no. 5, May 2016, Art. no. 054704.

[116] M. R. Ul'maskulov *et al.*, "Coherent summation of radiation from four-channel shock-excited RF source operating at 4 GHz and a repetition rate of 1000 Hz," *IEEE Trans. Plasma Sci.*, vol. 45, no. 10, pp. 2623–2628, Oct. 2017.

[117] M. R. Ulmaskulov *et al.*, "Four-channel generator of 8-GHz radiation based on gyromagnetic non-linear transmitting lines," *Rev. Sci. Instrum.*, vol. 90, no. 6, Jun. 2019, Art. no. 064703.

[118] I. V. Romanchenko *et al.*, "Four channel high power rf source with beam steering based on gyromagnetic nonlinear transmission lines," *Rev. Sci. Instrum.*, vol. 88, no. 5, May 2017, Art. no. 054703.

[119] K. M. Noel, A. M. Pearson, R. D. Curry, and K. A. O'Connor, "High frequency properties of high voltage barium titanate-ferrite multiferroic metamaterial composites," *IEEE Trans. Dielectr. Electr. Insul.*, vol. 23, no. 5, pp. 2965–2969, Oct. 2016.

[120] D. V. Reale, J. M. Parson, A. A. Neuber, J. C. Dickens, and J. J. Mankowski, "Investigation of a stripline transmission line structure for gyromagnetic nonlinear transmission line high power microwave sources," *Rev. Sci. Instrum.*, vol. 87, no. 3, Mar. 2016, Art. no. 034706.

[121] Q. J. Li, Z. P. Zhang, W. Ni, X. H. Sun, and C. C. Wang, "Large and switchable dielectric tunability in $Na_{1/2}Bi_{1/2}Cu_3Ti_4O_{12}$ ceramics," *J. Alloys Compd.*, vol. 695, pp. 1561–1565, Feb. 2017.

[122] R. Gholipur and A. Bahari, "Effect of electric field on the dielectric and magnetic properties of random nanocomposites," *Mater. Des.*, vol. 94, pp. 139–147, Mar. 2016.

[123] I. V. Romanchenko, V. V. Rostov, A. V. Gunin, and V. Y. Konev, “Gyromagnetic RF source for interdisciplinary research,” *Rev. Sci. Instrum.*, vol. 88, no. 2, Feb. 2017, Art. no. 024703.

[124] A. I. Gusev, M. S. Pedos, S. N. Rukin, and S. P. Timoshenkov, “Solid-state repetitive generator with a gyromagnetic nonlinear transmission line operating as a peak power amplifier,” *Rev. Sci. Instrum.*, vol. 88, no. 7, Jul. 2017, Art. no. 074703.

[125] B. W. Hoff, D. M. French, D. S. Simon, P. D. Lepell, T. Montoya, and S. L. Heidger, “High current nonlinear transmission line based electron beam driver,” *Phys. Rev. Accel. Beams*, vol. 20, no. 10, Oct. 2017, Art. no. 100401.

[126] B. W. Hoff and D. M. French, “Simulations of a disk-on-rod TWT driven by an NLTL-modulated electron beam,” *IEEE Trans. Plasma Sci.*, vol. 44, no. 8, pp. 1265–1269, Aug. 2016.

[127] J. A. Schrock *et al.*, “Spatially dispersive nonlinear transmission line experimental performance analysis,” *IEEE Trans. Dielectr. Electr. Insul.*, vol. 26, no. 2, pp. 412–415, Apr. 2019.

[128] J. O. Rossi and P. N. Rizzo, “Study of hybrid nonlinear transmission lines for high power RF generation,” in *2009 IEEE Pulsed Power Conference*, 2009, pp. 46–50.

[129] L. P. S. Neto, J. O. Rossi, J. J. Barroso, and E. Schamiloglu, “Hybrid nonlinear transmission lines used for RF soliton generation,” *IEEE Trans. Plasma Sci.*, vol. 46, no. 10, pp. 3648–3652, 2018.

[130] J. O. Rossi, P. N. Rizzo, and F. S. Yamasaki, “Prospects for applications of hybrid lines in RF generation,” in *2010 IEEE International Power Modulator and High Voltage Conference*, 2010, pp. 632–635.

[131] P. V. Priputnev, I. V. Romanchenko, P. V. Vykhodtsev, S. N. Maltsev, and V. Y. Konev, “RF pulse generation in combined nonlinear gyromagnetic transmission line,” in *2019 International Multi-Conference on Engineering, Computer and Information Sciences (SIBIRCON)*, 2019, pp. 0261–0264.

[132] M. S. Nikoo, S. M.-A. Hashemi, and F. Farzaneh, “Theoretical analysis of RF pulse termination in nonlinear transmission lines,” *IEEE Trans. Microw. Theory Tech.*, vol. 66, no. 11, pp. 1–8, 2018.

[133] A. J. Fairbanks, A. M. Darr, and A. L. Garner, “A review of nonlinear transmission line system design,” *IEEE Access*, vol. 8, pp. 148606–148621, 2020,

[134] A. L. Garner, G. J. Parker, and D. L. Simone, “Predicting effective permittivity of composites containing conductive inclusions at microwave frequencies,” *AIP Adv.*, vol. 2, no. 3, , Sep. 2012, Art. no. 032109.

[135] Z. Wang *et al.*, “Effect of high aspect ratio filler on dielectric properties of polymer composites: a study on barium titanate fibers and graphene platelets,” *IEEE Trans. Dielectr. Electr. Insul.*, vol. 19, no. 3, pp. 960–967, 2012.

[136] Z. Wang, J. Keith Nelson, H. Hillborg, S. Zhao, and L. S. Schadler, “Dielectric constant and breakdown strength of polymer composites with high aspect ratio fillers studied by finite element models,” *Compos. Sci. Technol.*, vol. 76, pp. 29–36, Mar. 2013.

[137] K. M. Noel, A. M. Pearson, R. D. Curry, and K. A. O. Connor, “High Frequency Properties of High Voltage Barium Titanate-Ferrite Multiferroic Metamaterial Composites,” *IEEE Trans. Dielectr. Electr. Insul.*, vol. 23, no. 5, pp. 2965–2969, 2016.

[138] R. P. Mahajan, K. K. Patankar, M. B. Kothale, and S. A. Patil, “Conductivity, dielectric behaviour and magnetoelectric effect in copper ferrite-barium titanate composites,” *Bull. Mater. Sci.*, vol. 23, no. 4, pp. 273–279, 2000.

[139] S. Liang, S. R. Chong, and E. P. Giannelis, “Barium titanate/epoxy composite dielectric materials for integrated thin film capacitors,” *Proc. - Electron. Components Technol. Conf., vol. Part F1334*, pp. 171–175, 1998.

[140] K. C. Cheng, C. M. Lin, S. F. Wang, S. T. Lin, and C. F. Yang, “Dielectric properties of epoxy resin-barium titanate composites at high frequency,” *Mater. Lett.*, vol. 61, no. 3, pp. 757–760, 2007.

[141] R. Grigalaitis *et al.*, “Dielectric and magnetic properties of BaTiO3 -NiFe 2O4 multiferroic composites,” *Ceram. Int.*, vol. 40, no. 4, pp. 6165–6170, 2014.

[142] L. Ramajo, M. Reboredo, and M. Castro, “Dielectric response and relaxation phenomena in composites of epoxy resin with BaTiO3 particles,” *Compos. Part A Appl. Sci. Manuf.*, vol. 36, no. 9, pp. 1267–1274, 2005.

[143] G. Wang, X. Chen, Y. Duan, and S. Liu, “Electromagnetic properties of carbon black and barium titanate composite materials,” *J. Alloys Compd.*, vol. 454, no. 1–2, pp. 340–346, 2008.

[144] R. P. Mahajan, K. K. Patankar, M. B. Kothale, S. C. Chaudhari, V. L. Mathe, and S. A. Patil, "Magnetoelectric effect in cobalt ferrite-barium titanate composites and their electrical properties," *Pramana - J. Phys.*, vol. 58, no. 5–6, pp. 1115–1124, 2002.

[145] P. Sambyal, A. P. Singh, M. Verma, M. Farukh, B. P. Singh, and S. K. Dhawan, "Tailored polyaniline/barium strontium titanate/expanded graphite multiphase composite for efficient radar absorption," *RSC Adv.*, vol. 4, no. 24, 2014, Art. no. 12624.

[146] K. Verma and S. Sharma, "Impedance spectroscopy and dielectric behavior in barium strontium titanate-nickel zinc ferrite composites," *Phys. Status Solidi Basic Res.*, vol. 249, no. 1, pp. 209–216, 2012.

[147] T. Hu, J. Juuti, and H. Jantunen, "RF properties of BST-PPS composites," *J. Eur. Ceram. Soc.*, vol. 27, no. 8-9 SPEC. ISS., pp. 2923–2926, 2007.

[148] R. J. Pandya, U. S. Joshi, and O. F. Caltun, "Microstructural and Electrical Properties of Barium Strontium Titanate and Nickel Zinc Ferrite Composites," *Procedia Mater. Sci.*, vol. 10, no. September, pp. 168–175, 2015.

[149] G. Gallone, F. Carpi, D. De Rossi, G. Levita, and A. Marchetti, "Dielectric constant enhancement in a silicone elastomer filled with lead magnesium niobate-lead titanate," *Mater. Sci. Eng. C*, vol. 27, no. 1, pp. 110–116, 2007.

[150] J. Ryu, A. V. Carazo, K. Uchino, and H. E. Kim, "Piezoelectric and magnetoelectric properties of lead zirconate titanate/Ni-ferrite particulate composites," *J. Electroceramics*, vol. 7, no. 1, pp. 17–24, 2001.

[151] A. M. Pearson, R. D. Curry, and K. M. Noel, "Characterization of Ni-Zn ferrite double-positive metamaterials for pulsed power systems," *IEEE Trans. Plasma Sci.*, vol. 44, no. 10, pp. 1978–1983, 2016.

[152] K. A. O'Connor and R. D. Curry, "High dielectric constant composites for high power antennas," in *Dig. Tech. Pap. Int. Pulsed Power Conf.*, pp. 212–217, 2011.

[153] S. Sindhu, M. R. Anantharaman, B. P. Thampi, K. A. Malini, and P. Kurian, "Evaluation of a.c. conductivity of rubber ferrite composites from dielectric measurements," *Bull. Mater. Sci.*, vol. 25, no. 7, pp. 599–607, 2002.

[154] K. A. O'Connor and R. D. Curry, "High voltage characterization of high dielectric constant composites," *Proc. 2010 IEEE Int. Power Modul. High Volt. Conf. IPMHVC 2010*, pp. 159–162, 2010.

[155] J. Krupka, T. Zychowicz, V. Bovtun, and S. Veljko, “Complex permittivity measurements of ferroelectrics employing composite dielectric resonator technique,” *IEEE Trans. Ultrason. Ferroelectr. Freq. Control*, vol. 53, no. 10, pp. 1883–1888, 2006.

[156] J. Krupka, J. Breeze, N. M. N. Alford, A. E. Centeno, L. Jensen, and T. Claussen, “Measurements of permittivity and dielectric loss tangent of high resistivity float zone silicon at microwave frequencies,” *16th Int. Conf. Microwaves, Radar Wirel. Commun. MIKON 2006*, vol. 54, no. 11, pp. 1097–1100, 2006.

[157] J. Xu, K. S. Moon, C. Tison, and C. P. Wong, “A novel aluminum-filled composite dielectric for embedded passive applications,” *IEEE Trans. Adv. Packag.*, vol. 29, no. 2, pp. 295–306, 2006.

[158] K. A. O’Connor and R. D. Curry, “Dielectric studies in the development of high energy density pulsed power capacitors,” Dig. Tech. Pap. Int. Pulsed Power Conf., pp. 1–6, 2013

[159] P. Pötschke, S. M. Dudkin, and I. Alig, “Dielectric spectroscopy on melt processed polycarbonate - Multiwalled carbon nanotube composites,” *Polymer (Guildf).*, vol. 44, no. 17, pp. 5023–5030, 2003.

[160] P. G. Bartley and S. B. Begley, “A new technique for the determination of the complex permittivity and permeability of materials,” *2010 IEEE Instrumentation & Measurement Technology Conference Proceedings*, 2010, pp. 54–57.

[161] G. H. Gardenier, F. Gui, and J. N. Demas, “Error propagation made easy - Or at least easier,” *J. Chem. Educ.*, vol. 88, no. 7, pp. 916–920, 2011.

[162] G. F. Knoll, Radiation Detection Measurements, 3rd ed. New York: John Wiley & Sons Inc., 2000.

[163] Y. Rao, J. Qu, T. Marinis, and C. P. Wong, “Precise numerical prediction of effective dielectric constant for polymer-ceramic composite based on effective-medium theory,” *IEEE Trans. Components Packag. Technol.*, vol. 23, no. 4, pp. 680–683, 2000.

[164] S. Giordano, “Effective medium theory for dispersions of dielectric ellipsoids,” *J. Electrostat.*, vol. 58, no. 1–2, pp. 59–76, 2003.

[165] D. K. Das-Gupta and K. Doughty, “Polymer-ceramic composite materials with high dielectric constants,” *Thin Solid Films*, vol. 158, no. 1, pp. 93–105, 1988.

[166] D. A. Powell, I. V. Shadrivov, Y. S. Kivshar, and M. V. Gorkunov, “Self-tuning mechanisms of nonlinear split-ring resonators,” *Appl. Phys. Lett.*, vol. 91, no. 14, Oct. 2007, Art. no. 144107.

[167] L. R. Raimundi, J. O. Rossi, E. G. . Rangel, L. C. Silva, E. Schamiloglu, and L. P. S. Neto, “RF generation at 200 MHz using a SiC Schottky diode lumped NLTL,” *2018 IEEE International Power Modulator and High Voltage Conference (IPMHVC)*, Jun. 2018, pp. 473–476.

[168] M. Dwyer, H. Kim, L. Mawst, and D. van der Weide, “Double-uniform Schottky diode nonlinear transmission line generating sub-picosecond transients,” *2018 IEEE Radio and Wireless Symposium (RWS)*, Jan. 2018, pp. 287–289.

[169] M. Ninic, B. Jokanovic, and P. Meyer, “Reconfigurable multi-state composite split-ring resonators,” *IEEE Microw. Wirel. Components Lett.*, vol. 26, no. 4, pp. 267–269, Apr. 2016.

[170] J. Guo, X. Wang, Z. Jia, J. Wang, and C. Chen, “Nonlinear electrical properties and field dependency of BST and nano-ZnO-doped silicone rubber composites,” *Molecules*, vol. 23, no. 12, 2018, Art. no. 3153.

[171] A. Sihvola, S. Saastamoinen, and K. Heiska, “Mixing rules and percolation,” *Remote Sens. Rev.*, vol. 9, no. 1–2, pp. 39–50, Mar. 1994.

[172] V. Myroshnychenko and C. Brosseau, “Effective complex permittivity of two-phase random composite media: A test of the two exponent phenomenological percolation equation,” *J. Appl. Phys.*, vol. 103, no. 8, Apr. 2008, Art. no. 084112.

[173] K. Bober, R. H. Giles, and J. Waldman, “Tailoring the microwave permittivity and permeability of composite materials,” *Int. J. Infrared Millimeter Waves*, vol. 18, no. 1, pp. 101–123, 1997.

[174] T. D. Crawford, A. J. Fairbanks, J. A. Hernandez, T. N. Tallman, and A. L. Garner, “Nonlinear permeability measurements for nickel zinc ferrite and nickel zinc ferrite/barium strontium titanate composites from 1-4 GHz,” *IEEE Trans. Magn.*, accepted, doi: 10.1109/TMAG.2021.3068820.

[175] C. W. Beier, J. M. Sanders, and R. L. Brutchey, “Improved breakdown strength and energy density in thin-film polyimide nanocomposites with small barium strontium titanate nanocrystal fillers,” *J. Phys. Chem. C*, vol. 117, no. 14, pp. 6958–6965, 2013.

[176] Y. Wang, J. Cui, Q. Yuan, Y. Niu, Y. Bai, and H. Wang, "Significantly enhanced breakdown strength and energy density in sandwich-structured barium titanate/poly(vinylidene fluoride) nanocomposites," *Adv. Mater.*, vol. 27, no. 42, pp. 6658–6663, 2015.

[177] S. Siddabattuni, T. P. Schuman, and F. Dogan, "Improved polymer nanocomposite dielectric breakdown performance through barium titanate to epoxy interface control," *Mater. Sci. Eng. B Solid-State Mater. Adv. Technol.*, vol. 176, no. 18, pp. 1422–1429, 2011.

[178] J. Benford, J.A. Swegle, E. Schamiloglu, High Power Microwaves, 3rd ed., CRC Press, Boca Raton, 2015.

[179] A.J. Fairbanks, T.D. Crawford, J.A. Hernandez, J.D. Mateja, X. Zhu, T.N. Tallman, A.L. Garner, Electromagnetic measurements of composites containing barium strontium titanate or nickel zinc ferrite inclusions from 1-4 GHz, *Compos. Sci. Technol*. accepted, doi: 10.1016/j.compscitech.2021.108798.

[180] J.F. Kolb, S. Kono, K.H. Schoenbach, "Nanosecond pulsed electric field generators for the study of subcellular effects," *Bioelectromagnetics*. Vol. 27, p. 172–187, 2006.

[181] F.S. Yamasaki, J.O. Rossi, J.J. Barroso, "RF generation using nonlinear transmission lines for aerospace applications," *2013 SBMO/IEEE MTT-S Int. Microw. Optoelectron. Conf., IEEE*, 2013: pp. 1–5.

[182] D. M. French and D. Shiffler, "High power microwave source with a three dimensional printed metamaterial slow-wave structure," *Rev. Sci. Instrum.*, vol. 87, no. 5, May 2016, Art. no. 053308.

[183] M. Samizadeh Nikoo, "Nonuniform line generator for high-power RF applications," *IEEE Trans. Plasma Sci.*, vol. 46, no. 1, pp. 64–71, Jan. 2018.

[184] S. E. Calico, M. C. Scott, and P. Pelletier, "The Phillips Laboratory's rep-rate pulser for high-power microwave source development," Proc. Ninth International Pulsed Power Conference, Albuquerque, NM, 21-23 June 1993 pp. 869-873.

[185] S. Kumar Sharma, P. Deb, R. Shukla, T. Prabaharan, and A. Shyam, "Compact pulse forming line using barium titanate ceramic material," *Rev. Sci. Instrum.*, vol. 82, no. 11, pp. 1–4, 2011.

[186] Y. S. Jin *et al.*, "High voltage ultrawide band pulse generator using Blumlein pulse forming line," *Rev. Sci. Instrum.*, vol. 83, no. 4, 2012.

[187] Z. Liu and J. Zhang, “Investigation of helical pulse forming line,” *Plasma Sci. Technol.*, vol. 8, no. 5, pp. 596–599, 2006.

[188] A. J. Fairbanks *et al.*, “Electromagnetic measurements of composites containing barium strontium titanate and nickel zinc ferrite inclusions from 1-4 GHz,” *Compos. Sci. Technol.*, vol. accepted.

[189] D. V. Berkov and J. Miltat, “Spin-torque driven magnetization dynamics: Micromagnetic modeling,” *J. J. Magn. Magn. Mater.*, vol. 320, no. 7, pp. 1238-1259, 2008.

[190] D. M. French, B. W. Hoff, W. Tang, S. Heidger, J. Allen-Flowers, and D. Shiffler, “Nonlinear transmission line based electron beam driver,” *Rev. Sci. Instrum.*, vol. 83, no. 12, Dec. 2012, Art. no. 123302.

[191] Y. Cui, J. Meng, L. Huang, Y. Yuan, H. Wang, and D. Zhu, “Operation analysis of the wideband high-power microwave sources based on the gyromagnetic nonlinear transmission lines,” *Rev. Sci. Instrum.*, vol. 92, no. 3, Mar. 2021, Art. no. 034702.

[192] I. V. Romanchenko, V. Y. Konev, V. V. Barmin, P. V. Priputnev, and S. N. Maltsev, “A nonlinear transmission line based on periodically placed silicon high voltage switches,” *AIP Adv.*, vol. 10, no. 12, Dec. 2020, Art. no. 125020.

[193] J. Lehr and P. Ron, *Foundations of Pulsed Power Technology*. John Wiley & Sons, 2017.

[194] L. Collier, M. B. Walls, J. Dickens, J. Mankowski, and A. Neuber, “Solid state linear transformer driver (LTD) development for HPM sources,” in 2015 *IEEE Pulsed Power Conference (PPC)*, May 2015, vol. 2015-Octob, pp. 1–4.

[195] K. E. Miller, J. R. Prager, T. M. Ziemba, J. G. Carscadden, C. Bowman, and I. Slobodov, “High voltage inductive adder,” US 10282567, 2019.

[196] Y. J. Chen, A. A. Neuber, J. Mankowski, J. C. Dickens, M. Kristiansen, and R. Gale, “Design and optimization of a compact, repetitive, high-power microwave system,” *Rev. Sci. Instrum.*, vol. 76, no. 10, Oct. 2005, Art. no. 104703.

APPENDIX A

The voltage divider was made using a 10 kΩ resistor connected to the high voltage output of one side of the Blumlein. The resistors chosen were the HVR RT series and Caddock MG730 series due to their purely resistive nature. The leads on both sides of the resistors were made as short as possible to minimize inductance but provide a solderable size for connections. This second side of the resistor was then connected to the center pin of a bulk head SMA connector.

Figure A- 1. High voltage resistors used in voltage divider (top) HVR RT series and (bottom) Caddock MG730 series. Both resistors have a 10 kΩ resistance.

The output of the SMA bulk head connector was then sent to the oscilloscope through a 10 ft RG 58 coaxial cable and 30 dB attenuator (Pasternack PE7049). The oscilloscope can be used in both 50 Ω and 1 MΩ coupling. Figure A-2 shows the circuit divider for modeling the voltage divider.

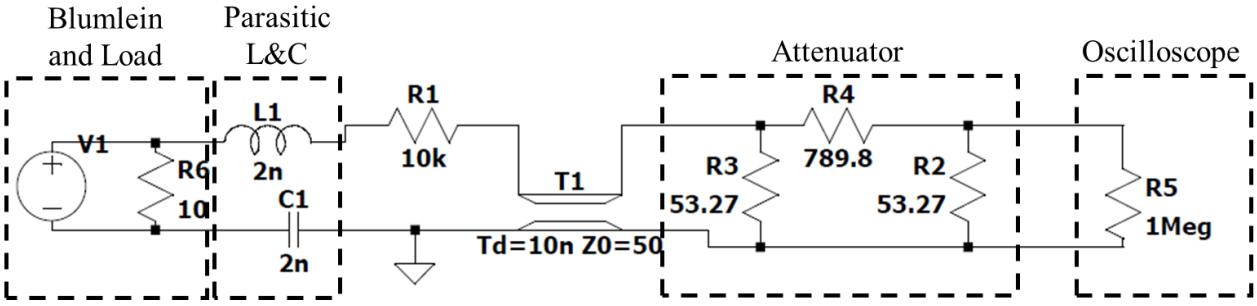

Figure A- 2. Circuit schematic of resistive voltage divider used to measure output of Blumlein and NLTL. The inductor, L1, and capacitor, C1, are the estimated parasitic capacitance and inductance of the divider.

VITA

Andrew J. Fairbanks

Objective:

Secure a position supporting National Defense Initiatives focused in the field of directed energy through the use of novel High Power Microwave devices and Pulsed Power technology.

Education:

Purdue University	West Lafayette, IN 47907
PhD Nuclear Engineering	Anticipated 05/2021
MS Nuclear Engineering	12/17
BS Nuclear Engineering	05/15

Professional Experience:

Naval Surface Warfare Center Dahlgren Division, Dahlgren, VA 05/16-
Pathways / SSEP / Engineer-5 Summers (16 Months) of post Bachelor Degree Engineering
(Supervisor: Jacob Walker)

- Wrote and submitted proposal for funding of novel high voltage modulator to drive multiple solid state high power microwave sources in a phased configuration for tactical defense purposes.
- Collaborated with Branch management and NSWCDD technical liaison to build collaboration between NSWCDD and academic institutions
    - Collaborated with NSWCDD outreach to determine avenues for collaboration with academia and summarized various opportunities in report to branch management
    - Proposed funding call for technological development to aid in the advancement of various high voltage modulator systems to increase effectiveness and stability of current high power microwave systems
- Compiled civilian and military standards for collateral effects of electronic systems in a report that aided in mission planning and modeling of tactical deployment of HPM systems
- Compiled civilian and military standards for biological effects and limits for RF exposure to personnel and evaluated thresholds to high power RF exposure
- Compiled and evaluated various solid state switching technologies for the feasibility of implementation into high voltage modulators in order to increase power handling capabilities and source effectiveness of current and future high power microwave sources
- Part of a team that designed and developed a novel direct injection high voltage source for base defense while performing the following responsibilities:
    - Tested and evaluated output of novel direct inject pulsed power system

while designing and implementing electromagnetic interference mitigation
    - Supported design, build, and assembly of system
    - Collaborated as part of a team to install and demonstrate system
    - Provided hands on and classroom training to over 400 security forces personnel on the proper function and safe implementation of system
- Worked as part of a team evaluating High Power Microwave sources and their effects on various targets while performing the following responsibilities:
    - Tested and evaluated multiple high power microwave systems′ effects
    - Operated data acquisition system for the evaluation and testing of high power microwave systems
    - Performed diagnostics on systems to determine malfunction cause and evaluate corrections and mitigations to high power microwave system
- Participated in the development of novel high voltage pulsed modulator for driving multiple high power microwave sources while performing the following responsibilities:
    - Provided technical expertise for annual review
    - Tested and evaluated novel pulse power system for feasibility in driving relativistic high power microwave magnetrons
    - Designed laboratory layout of high power modulator system to allow for optimal use of space and safe operation of 1 T electromagnet
    - Calculated effective dose rate and required shielding for safe operation of relativistic high power microwave magnetron
- Tested and evaluated existing technology with novel implementation with the following responsibilities
    - Evaluated novel application of existing technology by testing various waveforms, power output, and orientation of intended targets
    - Designed and constructed test fixture for target positions and waveform measurements, allowing for offsite testing
    - Evaluated, repaired, and tested target diagnostic system to provide testing capabilities that would have otherwise have been canceled
- Part of a team evaluating current, past, and future high power microwave technologies and supporting technologies while performing the following duties:
    - Designed and simulated test circuitry for the evaluation of novel solid state technologies
    - Collaborated with industry, academia, and government personnel on the design and testing HPM systems
    - Designed and reconstructed high voltage modulator for the use in driving solid state high power microwave systems
    - Evaluated proposals for the simulation of RF effects on various target sets and RF coupling on targets of interest
    - Evaluated and summarized various relativistic, vacuum, solid state, and conventional high power microwave sources and their potential implementation and presented written report of the summarization
- Designed and developed novel circuit representation for evaluation of RF effects on representative electronic circuits of interest using Graph Theory
    - Generated computer code to represent circuits of interest and simulate RF propagation and coupling of signals through the use of Graph Theory
    - Investigate previous implementations of Graph Theory for signal propagation

- Evaluated feasibility of using Graph theory for easier simulation of RF coupling on representative circuits
- Designed pulse power source to provide a 10 ns high voltage pulse, up to 50 kV, with fast rise time for application to high power microwave system

Naval Research Laboratory, Washington, DC 06/15-8/15
Directed Energy Professional Society Intern/ Engineer- 3 Months of post Bachelor Degree

Engineering Experience

(Supervisor: Mike Helle)

- Interrogated laser induced plasma filaments with low power RF source to evaluate plasma properties
- Conducted experiments varying laser, target gas, and RF field parameters to examine plasma change
- Determined sensitivity of plasma filament position in microwave waveguide through simulations and experimental measurements
- Analyzed data using mathematical software

University Experience

Purdue University, West Lafayette, Indiana (Supervisor: Prof. Robert Bean) 06/14-08/14

- Engineered and implemented safety systems for PUR-1 research nuclear reactor
- Examined and refined procedures for laboratory classes
- Evaluated nuclear diagnostic and measurement equipment

Leibniz Institute for Plasma Science and Technology, Greifswald, Germany 07/13-08/13
Summer Research Intern (Supervisor: Prof. Juergen Kolb)

- Built various Blumlein pulse forming networks
- Experimented with switching, grounding, inductance, and capacitance
- Examined effects on pulse shape and reflection

Research Experience:

BioElectrics and ElectroPhysics Laboratory (BEEP) 02/13 -
Research Assistant under Dr. Allen Garner

- Designed, constructed, and tested nonlinear transmission lines using novel composites and various line impedances
- Tested nonlinear transmission lines using various pulsed power topologies and impedances
- Designed and simulated pulse power systems for HPM technologies
- Designed and built novel composites for use in nonlinear transmission lines
- Designed impedance matched transmission lines for high power applications
- Measured high frequency material properties of dielectric and magnetic composites
- Designed and tested pulse generators for treatment of waste water through plasma discharges
- Mentored undergraduate students and Master's students both in-person and remotely
- Examined change in cellular conductivity of cancer cells due to nanosecond pulsed electric fields in real time
- Designed and Built Blumlein pulse generator for air flow modification in jet engines

- Applied pulsed electric fields to adhesion cells to develop a standard operating procedure
- Investigated change in cellular conductivity of chloroplasts due to nanosecond pulsed electric fields in real time
- Measured the conductivity and permittivity of cellular components and their change after the application of nanosecond pulsed electric fields

Radiation Sterilization of Various Food 01/12-05/12

Undergraduate Research Assistant under Dr. Rusi Taleyarkhan

- Measured the growth of mold and change in composition of food after various radiation doses
- Collected and analyzed data to determine if a trend was present

Teaching Experience:

Teaching Assistant Fall 2015,2016

Graduate Teaching Assistant for NUCL 305 (Nuclear Instrumentation Laboratory II)

- Taught NUCL 305 lab course two to three times a week and organized course materials and lab space. Held office hours every week to teach undergraduate students

Graduate Teaching Assistant for NUCL 205 (Nuclear Instrumentation Laboratory I) Spring 2016

- Taught NUCL 205 lab course two to three times a week and organized course materials and lab space. Held Office hours every week to assist undergraduate students

Relevant Skills:

- PSpice and LT Spice
- ImageJ
- MATLAB
- High voltage, high frequency measurements
- High power microwave design
- Construction and operation of Blumlein pulse forming network
- Use Mathematica to analyze and present data
- COMSOL AC/DC circuit module
- Operation of high voltage equipment
- Experience with wiring, machining, and construction
- Developed and instituted operating procedures and safety measures
- Created and implemented experiments to investigate different phenomena
- Trained in cell culturing and preparation

Refereed Journal Articles

1. R. S. Brayfield II, A. Jassem, M. V. Lauria, **A. J. Fairbanks**, Kevin M. Keener, and A. L. Garner, "Characterization of High Voltage Cold Atmospheric Plasma Generation in Sealed Packages as a Function of Container Material and Fill Gas," *Plasma Chem. Plasma Process.* **38**, 379-395 (2018).
2. R. S. Brayfield, II, **A. J. Fairbanks**, A. M. Loveless, S. Gao, A. Dhanabal, W. Li, C. Darr, W. Wu, and A. L. Garner, "The Impact of Cathode Surface Roughness and Multiple Breakdown Events on Microscale Gas Breakdown at Atmospheric Pressure," *Journal of Applied Physics* **125**, 203302 (2019).
3. **A. J. Fairbanks**, A. M. Darr, and A. L. Garner, "A Review of Nonlinear Transmission Line System

Design," *IEEE Access* **8**, 148606 – 148621 (2020).

4. T. D. Crawford, **A. J. Fairbanks**, J. A. Hernandez, T. N. Tallman, and A. L. Garner, "Nonlinear permeability measurements for nickel zinc ferrite and nickel zinc ferrite/barium strontium titanate composites from 1-4 GHz," *IEEE Trans. Magn*. In press https://doi.org/10.1109/TMAG.2021.3068820
5. **A.J. Fairbanks**, T.D. Crawford, J.A. Hernandez, J.D. Mateja, X. Zhu, T.N. Tallman, and A.L. Garner, Electromagnetic measurements of composites containing barium strontium titanate or nickel zinc ferrite inclusions from 1-4 GHz, *Compos. Sci. Technol*. In press https://doi.org/10.1016/j.compscitech.2021.108798
6. **A.J. Fairbanks**, T.D. Crawford, J.A. Hernandez, J.D. Mateja, X. Zhu, T.N. Tallman, and A.L. Garner, "Electromagnetic measurements of composites containing barium strontium titanate and nickel zinc ferrite inclusions from 1-4 GHz," *Compos. Sci. Technol*., Accepted 20 April 2021.
7. **[INVITED] A. J. Fairbanks**, T. D. Crawford, M. E. Vaughn, and A. L. Garner, "Simulated and Measured Output from a Composite Nonlinear Transmission Line Driven by a Blumlein Pulse Generator," Submitted, *IEEE Trans. Plasma Sci*.

Conference Papers

1. L. Mittal, V. Raman, I. G. Camarillo, A. L. Garner, **A. J. Fairbanks**, G. A. Dunn, and R. Sundararajan, "Synergy of Micro and Nanosecond Electrical Pulses with Chemotherapeutics on Human Cancer Cell Viability," 2017 Annual Report Conference on Electrical Insulation and Dielectric Phenomena, pp. 596-599 (2017).
2. **A. J. Fairbanks**, A. Vadlamani, T. Whitmer, and A. L. Garner, "Nanosecond Electric Pulse Induced Changes in Cell Suspension Conductivity," in 2015 Annual Report Conference on Electrical Insulation and Dielectric Phenomena, pp. 628-631 (2015).
3. **A. J. Fairbanks**, A. Vadlamani, T. Whitmer, and A. L. Garner, "Real Time Measurements of Cell Suspension Conductivity Changes Due to Pulsed Electric Fields," in Proc. 2014 IEEE International Power Modulator and High Voltage Conference (IPMHVC), pp. 399-401 (2014).

Presentations:

1. **A. J. Fairbanks**, X. Zhu, J. A. Hernandez, T. N. Tallman, A. L. Garner, "Composite Material Development for Nonlinear Transmission Lines," 21st Annual Directed Energy Science & Technology Symposium, Open and Limited Poster Session, 09 April 2019, Destin, FL, USA.
2. R. Brayfield, **A. Fairbanks**, A. Loveless, W. Li, C. Darr, and A. Garner, "Submicroscale Gas Breakdown as a Function of Cathode Protrusion," 1P21, 24 June 2019, Orlando, FL USA.
3. R. Brayfield II, **A. Fairbanks**, A. Loveless, S. Gao, R. Bean, Y. Xuan, W. Wu, and A. Garner, "The Impact of Electrode Surface Roughness on Field Emission Driven Breakdown for Microscale Gaps," 04 June 2018, Jackson Lake Lodge, WY, USA, Poster 1P02 (2018).
4. L. Mittal, V. Raman, I. Camarillo, A. Garner, **A. Fairbanks**, G. Dunn, and R. Sundararajan, "Nanosecond Electric Pulses for Anti-Cancer Treatment," 06 June 2018, Jackson Lake Lodge, WY, USA, Poster 3P18 (2018).
5. L. Mittal, V. Raman, I. G. Camarillo, A. L. Garner, A. J. Fairbanks, G. A. Dunn, and R. Sundararajan, "Synergy of Micro and Nanosecond Electrical Pulses with Chemotherapeutics on Human Cancer Cell Viability," 2017 Annual Report Conference on Electrical Insulation and Dielectric Phenomena, pp. 596-599 (2017).
6. A. L. Garner, R. S. Brayfield II, **A. J. Fairbanks**, K. P. Newman, S. M. Sanders, R. Jagannath, B. Singh, B.-S. Chen, and S. P. M. Bane, "Electric Pulse Parameter and Electrode Geometry Impact on Plasma Formation," 2016 IEEE International Power Modulator and High Voltage Conference, 07 July 2016, San Francisco, CA, p. 259 (2016).

7. M. Mulligan, S. Das, **A. Fairbanks**, L. A. Sherman, A. Garner, A. Shay, and J. Myers, "Electric Pulse Parameter Exploration for Lipid Extraction from Microalgae," 2016 IEEE International Power Modulator and High Voltage Conference, 07 July 2016, San Francisco, CA, p. 173 (2016).
8. **A. Fairbanks**, A. Darr, A. Vadlamani, and A. Garner, "Electric Pulse Modification of Mammalian Cell Suspension Conductivity," 2016 IEEE International Power Modulator and High Voltage Conference, 07 July 2016, San Francisco, CA, p. 162 (2016).
9. **A. J. Fairbanks**, A. Vadlamani, T. Whitmer, and A. L. Garner, "Nanosecond Electric Pulse Induced Changes in Cell Suspension Conductivity," in 2015 Annual Report Conference on Electrical Insulation and Dielectric Phenomena, October 2015, Ann Arbor, MI, pp. 628-631 (2015).
10. **A. Fairbanks**, A. Vadlamani, T. Whitmer, R. Sundararajan, and A. Garner, "Cell suspension electrical measurements in real time," BioEM 2015, 16 June 2015, Asilomar Conference Center, Pacific Grove, CA, 16 June 2015, p.64 (2015).
11. **A. J. Fairbanks**, A. Vadlamani, T. Whitmer, and A. L. Garner, "Electrical conductivity changes in cell suspensions during electric pulses," 2015 IEEE International Pulsed Power Conference, 01 June 2015, Austin, TX (2015).
12. A. L. Garner, S. P. M. Bane, **A. J. Fairbanks**, B. –S. Chen, R. S. Brayfield II, "Using electrode geometry and electric pulse parameters to control atmospheric pressure plasma formation," 2015 IEEE International Pulsed Power Conference, 01 June 2015, Austin, TX (2015).
13. S. Sommakia[+], A. Baijnath, K. Raun, **A. J. Fairbanks**, K. Otto, and A. L. Garner, "Pulsed electric field interactions with primary mixed cortical cultures," 11th International Bioelectrics Symposium, October 2014, Columbia, MO, p. 31 (2014).
14. **A. J. Fairbanks**, A. Vadlamani, T. Whitmer, and A. L. Garner, "Cell suspension conductivity variation during electric pulses," 11th International Bioelectrics Symposium, October 2014, Columbia, MO, p. 28 (2014).
15. A. Vadlamani, J. Zhuang, **A. J. Fairbanks**, G. Dunn, J. F. Kolb, and A. L. Garner, "Temperature dependence of the electrical properties of biological cells," 11th International Bioelectrics Symposium, October 2014, Columbia, MO, p. 27 (2014).
16. **A. J. Fairbanks**, A. Vadlamani, T. Whitmer, and A. L. Garner, "Real time Measurements of Cell Suspension Conductivity Changes Due to Pulsed Electric Fields," 2014 IEEE International Power Modulator and High Voltage Conference, June 2014, Santa Fe, NM, p. 111 (2014).
17. A. Vadlamani, **A. J. Fairbanks**, S. P. M. Bane, and A. L. Garner, "Variable High Voltage, High Frequency Nanosecond Pulser for Plasma Combustion," 2014 IEEE International Plasma Sciences/BEAMS Conference, May 2014, Washington, DC.

Conference Oral Presentations [*italics*=presenter]

1. ***A. J. Fairbanks***, T. D. Crawford, J. A. Hernandez, T. N. Tallman, A. L. Garner, "Testing Nonlinear Transmission Lines Made of Novel Composites," 47th IEEE International Conference on Plasma Science, 10 December 2020, virtual.
2. *T. D. Crawford*, **A. J. Fairbanks**, J. A. Hernandez, T. N. Tallman, A. L. Garner, "Nonlinear Permeability Measurements of Single and Dual Inclusion Composites for NLTL Systems from 1-4 GHz," 47th IEEE International Conference on Plasma Science, 10 December 2020, virtual.
3. ***A. J. Fairbanks***, X. Zhu, J. A. Hernandez, T. D. Crawford, J. D. Mateja, T. N. Tallman, A. L. Garner, "Experimental and Simulation Evaluation of Composite Materials for NLTL System Design," 22nd Annual Directed Energy Science & Technology Symposium, Student Workshop, 11 March 2020, West Point, NY, USA.
4. R. S. Brayfield II, A. M. Darr, W. Li, **A. J. Fairbanks**, H. Wang, *A. M. Loveless*, and A. L. Garner, "Nano/Micro-Meter electrode topology Effects on Electron Emission," 22nd Annual Directed Energy Science & Technology Symposium, Student Workshop, 11 March 2020, West Point, NY, USA.

5. *R. Brayfield*, **A. Fairbanks**, A. Loveless, S. Gao, C. Darr, J. Malayter, W. Wu, and A. Garner, "Microscale Gas Breakdown Voltage Dependence on Electrode Surface," IEEE Pulsed Power and Plasma Science Conference, 3F3, 25 June 2019.
6. ***A. Fairbanks***, X. Zhu, J. Hernandez, S. Gao, W. Wu, T. Tallman, and A. Garner, "Development and Diagnostics on Composites for Nonlinear Transmission Lines," IEEE Pulsed Power and Plasma Science Conference, 2C3, 24 June 2019.
7. *X. Zhu*, **A. J. Fairbanks**, and A. L. Garner, "Assessing Effective Medium Theories for Designing Composites for Nonlinear Transmission Lines," IEEE Pulsed Power and Plasma Science Conference, 2C2, 24 June 2019.
8. *R. S. Brayfield, II*, **A. J. Fairbanks**, A. M. Loveless, S. Gao, W. Li, C. Darr, J. R. Malayter, W. Wu, and A. L. Garner, "Experimental assessment of electrode effects on gas breakdown for microscale gaps," 21st Annual Directed Energy Science & Technology Symposium, Student Workshop II, 10 April 2019, Destin, FL, USA.
9. **[INVITED]** *A. L. Garner*, A. M. Loveless, R. S. Brayfield II , **A. J. Fairbanks** , S. D. Dyanko , S. Gao , W. Wu, R. S. Bean, and G. Meng, "Gas Breakdown at Microscale and Smaller Gaps: Theoretical Unification of Mechanisms and Experimental Assessment of Surface Roughness," iPlasmaNanoIX, New Buffalo, MI, 27 August 2018.
10. ***A. Fairbanks***, A. Darr, A. Vadlamani, R. Brayfield II, and A. Garner, "Real-time Conductivity Measurements of Mammalian Cell Suspension during Nanosecond Electric Pulse Trains," 2018 IEEE International Power Modulator and High Voltage Conference, 04 June 2018, Jackson Lake Lodge, WY, USA, Oral 2O-1 (2018).
11. *A. L. Garner*, R. S. Brayfield II, **A. J. Fairbanks**, A. M. Loveless, S. Gao, R. S. Bean, Y. Xuan, and W. Wu, "Microscale Gas Breakdown and Implications to Electron Emission," 20th Annual Directed Energy Science & Technology Symposium, High Power Microwave (HPM) Technologies, 01 March 2018, Oxnard, CA, USA.
12. **A. J. Fairbanks**, A. M. Darr, A. Vadlamani, and *A. L. Garner*, "Measurement of Electric Pulse Modification of Cell Suspension Conductivity during Treatment," 2017 IEEE International Conference on Plasma Sciences, Oral TU 1.5-4, 25 May 2017, Atlantic City, NJ USA.
13. R. S. Brayfield II, **A. J. Fairbanks**, and *A. L. Garner*, "Plasma Species Variation as a Function of Voltage for High Voltage Cold Atmospheric Pressure Plasmas in Sealed Bags," 2017 IEEE International Conference on Plasma Sciences, Oral TU 2.5-2, 23 May 2017, Atlantic City, NJ USA.
14. R. S. Brayfield II, A. Jassem, M. Lauria, **A. J. Fairbanks**, *A. L. Garner*, and K. M. Keener, "Optical Emission Spectroscopy of High Voltage, Cold Atmospheric Pressure Plasmas," 2016 IEEE International Conference on Plasma Sciences, Oral 3E-2, 21 June 2016, Banff, Alberta, Canada.
15. **[INVITED]** *A. L. Garner*, V. B. Neculaes, M. Deminsky, A. S. Torres, V. Robinson, A. Vadlamani, J. J. Maciejewski, T. Whitmer, **A. J. Fairbanks**, S. K. Wyatt, A. L. Brewster, R. Sundararajan, and B. Potapkin, "Electric Pulse Manipulation of Biological Cells: From Theory to Applications," 60th Annual Health Physics Society Conference, 14 July 2015, Indianapolis, IN, TAM-G – Special Session: Non-Ionizing Radiation, TAM-G.3.

Professional Organizations:

- **IEEE Member** 2014-
- **IEEE Nuclear and Plasma Science Society:** 2014-
- **IEEE Young Professionals** 2014-
- **IEEE Microwave Theory and Techniques Society** 2015-

Awards:

Directed Energy Professional Society Directed Energy Graduate Scholar	2020
Exceptional Dedication to the Mission	27 March 2019
Krauss Scholarship	2018
IEEE International Power Modulator and High Voltage Conference Travel Award	2018
Graduate Teaching Excellence Award	2017
Alpha Nu Sigma Nuclear Engineering Honor Society	2017
Krauss Scholarship	2017
IEEE Conference on Electrical Insulation and Dielectric Physics (CEIDP) Student Travel Award	2015